Measurement of Direct Photons in Ultra-Relativistic Au+Au Collisions

A Dissertation Presented

by

Haijiang Gong

to

The Graduate School

in Partial Fulfillment of the Requirements

for the Degree of

Doctor of Philosophy

in

Physics

Stony Brook University

April 2014

Stony Brook University

The Graduate School

Haijiang Gong

We, the dissertation committee for the above candidate for the Doctor of Philosophy degree, hereby recommend acceptance of this dissertation.

Axel Drees
Professor, Department of Physics and Astronomy

Robert McCarthy
Professor, Department of Physics and Astronomy

Thomas Kuo
Professor, Department of Physics and Astronomy

Gabor David
Physicist, Brookhaven National Laboratory

This dissertation is accepted by the Graduate School.

Graduate School

Abstract of the Dissertation

Measurement of Direct Photons in Ultra-Relativistic Au+Au Collisions

by

Haijiang Gong

Doctor of Philosophy

in

Physics

Stony Brook University

2014

Direct photons provide a tool to study the different stages of a heavy ion collision, especially the formation of a quark-gluon plasma (QGP), without being influenced by the strong interaction and hadronization processes. The yield of direct photons can be determined based on the inclusive photon yield and the photon yield from hadronic decays.

At the high p_T range, direct photons are produced in initial parton-parton scatterings, quark-gluon Compton scattering $g + q \rightarrow \gamma + q$ and quark-antiquark annihilation $q + \overline{q} \rightarrow \gamma + g$ which are well described by perturbative Quantum Chromodynamics (pQCD). PHENIX published measurement of direct photons from RUN2 dataset in $\sqrt{s_{NN}} = 200GeV$ Au+Au collisions [1] indicates that there is a significant direct photon signal for $p_T \geq 4GeV/c$ and it is consistent with the binary scaled pQCD model calculation from p+p collisions [2]. Apparently, the direct photon production is in direct contrast to high p_T hadrons suppression observed in

Au+Au collisions [3] and serve as an important test of binary scaling from p+p collisions which provides strong confirmation that the observed large suppression of high p_T hadron production in central Au+Au collisions is dominantly a final-state effect due to parton energy loss in the dense produced medium, rather than an initial-state effect.

At low p_T range where a significant fraction of direct photons is expected to come from the thermalized medium of deconfined quarks and gluons, the measurement is very challenging. These so-called thermal photons carry information about the initial temperature of the medium.

We present a new analysis technique that was developed to improve and understand the direct photon production measurement in the low and medium p_T range. The technique was applied to PHENIX Run4 Au+Au $\sqrt{s_{NN}} = 200 GeV/c$ collisions dataset. It uses strict particle identification(PID) in the Electromagnetic Calorimeter(EMCal) and a charged particle veto to extract a clean photon signal. These photons are then tagged with EMCal photon candidates with loose PID cuts, which can be reconstructed with high efficiency, to determine the fraction of photons originating from π^0 decays. Most systematic uncertainties and detector effects cancel in this method. The results are compared with recent PHENIX direct photon measurement through external conversion method and various theoretical calculation predicting thermal photon production.

Contents

List of Figures

List of Tables

Acknowledgements

I would like to express my sincere gratitude to my PhD advisor, Prof. Axel Drees, for his great patience and guidance. I can not imagine myself finishing this challenging research without his support. He has been an excellent advisor and a good friend.

I would like to extend my thanks to Relativistic Heavy Ion research group in Stony Brook University, especially to Prof. Barbara Jacak, Tom Hemmick and Ralf Averbeck for their help on my research and to Alberica Toia and Torsten Dahms for endless days and nights together debugging code and discussing physics. It has been a wonderful experience to work within the PHENIX collaboration.

Last but not least, I would like to thank my parents, Xiaoxin Gong and Mimi Shui, for their nurturing and unconditional support towards my love to science ever since I was a child. I also want to express my graciousness to my wife Peggy for her encouragement and love to accomplish this work.

Chapter 1

Theoretical Background

Relativistic heavy ion collisions is an excellent tool to study nuclear matter under extreme conditions, i.e. the Quark Gluon Plasma (QGP), and to explore the phase diagram of strongly interacting matter for new states. However, the detection of such dense matter under extreme condition is very challenging due to the fact that it has only a fleeting existence which is followed by return to a phase of hot hadronic matter. A number of observables have been proposed which should show a behavior distinctly different from usual nuclear matter [23].

For the interpretation of results from heavy ion collisions viewed as a superposition of two nucleons, a basic understanding of more elementary nucleon-nucleon reactions such as p+p collision is crucial. Above a center of mass energy of $\sqrt{s} \sim 10GeV$ the total cross section for p+p collisions is roughly constant $\theta_{tot} \sim 40mb$ [24].The cross section at these energies is dominated by inelastic reactions where the colliding particles lose energy with the deposited energy resulting in the production of new particles. The mean number of produced particles, mostly pions, increases only slowly with the center of mass energy and is dominated by particles with small transverse momenta.

So called soft processes account for the majority of particle production which dominates at low transverse momenta $p_T \leq 1GeV/c$. The momentum spectrum of these particles is well described by an exponential function $e^{-\alpha p_T}$ with constant $\alpha \sim 6/(GeV/c)$. However, it was found that the cross section for these soft particles cannot be extrapolated to high p_T and the distribution in this kinematical region is better described by a power law which is governed by hard processes with large Q^2. These hard processes can be treated in QCD perturbatively (pQCD) where the cross section for a hadron can be written as Eq. 1.1 [25]. Soft processes are characterized by a small momentum transfer Q^2 which is of the order of QCD scale and can not be treated in pQCD as quarks inside hadrons can not be considered as asymptotically free.

$$E\frac{d^3\theta_h}{dp^3} = \sum_{a,b,c} f_a(x,Q^2) \otimes f_b(x,Q^2) \otimes \frac{d\sigma_{ab\to c}}{d^3p} \otimes D_{c/h}(z,Q^2) \qquad (1.1)$$

The first two terms in Eq. 1.1, $f_{q,g}(x,Q^2)$, are the non-perturbative distribution functions of partons in the colliding nucleons, which depend only on the momentum transfer and the parton fractional momentum x. They can be determined e.g. in deep-inelastic electron-nucleus reactions. The third term is the perturbatively computable cross section describing parton-parton scattering in the form of $ab \to c$. The last term $D_{c/h}(z,Q^2)$ is the universal but non-perturbative fragmentation function of the scattered parton c into the hadron h carrying a fraction $z = p^h/p^c$ of the parton momentum. It can be also determined experimentally. If the outgoing particle in the hard scattering process is a photon, the fragmentation function reduces to a $\delta(1-z)$ function.

It should be noted that calculation of total cross sections via Eq. 1.1 suffers from uncertainties due to the arbitrary choice of factorization, renormalization and fragmentation scales. The different scales are usually chosen identical and on the order of transverse momentum.

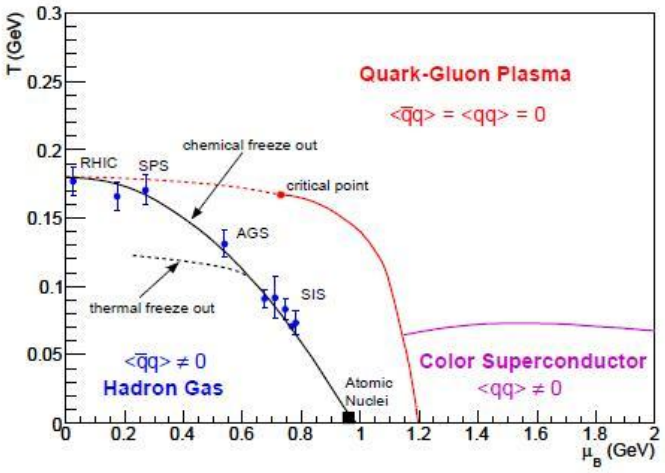

Figure 1.1: Phase diagram of hadronic matter as function of temperature T and baryonic chemical potential μ_B which illustrates the merging picture of transition from hadronic to quark matter. The measured chemical freeze out points from SIS, AGS, SPS and RHIC energies are shown as points [4]. The dashed line denotes the thermal freeze out.

The phase diagram of strongly interacting matter, shown schematically in

Fig. 1.1, depicts possible phases of nuclear matter depending on its temperature T and the baryo-chemical potential μ_B. At low temperatures and low baryo-chemical potentials, nuclear matter exists in its ordinary form, e.g. as in atomic nuclei. On the other hand, the phase transitions in two extremes are interesting for cosmology and astrophysics. In the Big Bang scenario for the origin of universe, the elementary particles were produced in the freeze-out from a phase with high temperature and low baryon density on the order of 1 μ_s after the Big Bang. For the phase transition with high baryon density to even more exotic states of matter at zero temperature, it may today still be reached in the center of neutron stars.

1.1 Quark Gluon Plasma

The Quark-Gluon-Plasma (QGP) is a state where quarks and gluons are deconfined. Under normal circumstances, because of non-perturbative character of QCD at large distances and small momentum transfer, it is very difficult to derive quantities for bound quark-gluon states, hadrons and the atomic nuclei based on first principles. A useful phenomenological description of quarks in hadrons is provided by bag models in which the quarks are treated as massless inside a bag of finite temperature and as infinitely massive outside the bag [26] [27]. In this model confinement results from balance between the bag pressure, directed inward and the stress arising from the kinetic energy of quarks. If this balance is distorted and the pressure of quarks is larger than the bag pressure, a new phase of matter containing deconfined quark and gluons is formed the QGP.

In order to reach this new phase, two extreme scenarios can be considered: a quark-gluon system in thermal equilibrium with a large temperature $T > T_c$, where the kinetic energy of the quarks and the gluons with corresponding pressure P exceeds the bag pressure, or a system at T = 0 with high baryon density n_B or baryo-chemical potential μ_B, where the Pauli principle forces the quarks into states with increasing momenta as they get closer, leading to a degenerative pressure that may exceed the bag pressure. The corresponding limits of energy density ϵ_{SB} ("Stefan-Boltzmann" limit) is defined below

$$\epsilon_{SB} = (\frac{7}{8} d_{quark} + d_{gluon}) \frac{\pi^2}{30} T^4 \tag{1.2}$$

where d_{quark} and d_{gluon} stand for the degree of freedom of quarks and gluons, respectively. Typical values for the critical temperature and critical baryon number density in these two extreme scenarios derived from the bag model in [27] is $T_c \sim 144 MeV$.

Another way of calculating the critical temperature is lattice QCD [28] where the gauge theory of QCD is formulated on a discrete lattice of space-time. This approach has the advantage that it retains the fundamental characteristics of QCD and makes it accessible to computational methods in order to calculate the properties of quarks and gluons. Nowadays, lattice QCD calculation starts taking into account more realistic quark masses which was not possible before due to the lack of computing power. Furthermore, it can calculate observables like baryon masses with increasing accuracy [29, 30]. Such lattice calculation has shown a rapid increase of energy and entropy density at temperatures $T_c \sim 190MeV$ [31], an indication of deconfinement.

Fig. 1.2 illustrates the sudden rise of the energy density ϵ/T^4 at a critical temperature $T_c \sim 170MeV$ for different numbers of quark flavors. This is interpreted as the phase transition into deconfied QGP phase [32]. The expectation for an ideal gas with quark and gluon degrees of freedom, the Stefan-Boltzmann limit of the energy density, is also shown in Fig. 1.2. It is not reached even for temperatures four times larger than the critical temperature, indicating that the often used description of QGP as a free gas of weakly interacting quarks and gluons may not be applicable at these temperatures [32].

1.2 Evolution of Ultra-Relativistic Heavy Ion Collisions

Relativistic heavy ion collisions have various phases from initial collisions to the final hadronic state. One simple view of this process is that the Lorentz-contracted nuclei interact only in the region of geometrical overlap, determined by the impact parameter b as shown in Fig. 1.3. The corresponding nucleons are called participants, while the nucleons outside the geometrical overlap, the spectators, are basically unaffected by the collision. The participants interact with each other in the reaction zone, leading to the formation of a hot and dense region, the fireball. There are two basic scenarios for the formation of the fireball depending on the nuclear stopping in the reaction. For large stopping, described in the Landau model [33], the complete kinetic energy of the nucleons is converted into thermal energy and a baryon-rich fireball is formed. The characteristic rapidity distribution of produced particles in such a reaction has a maximum at mid-rapidity. In the Bjorken scenario [34] the stopping is limited and the nucleons penetrate each other, they exhibit transparency. This leads to a fireball with low baryo-chemical potential as the baryon number remains concentrated near the beam rapidity. The rapidity

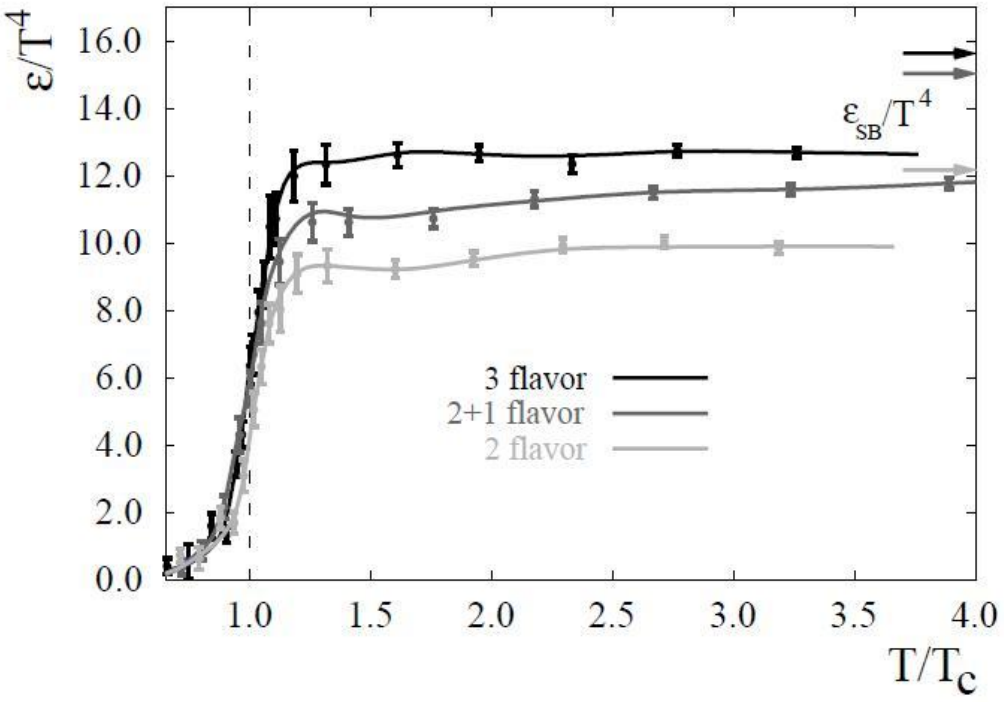

Figure 1.2: Lattic QCD results [5] for the energy density (ϵ) divided by T^4, which is degree of freedom as known from Eq. 1.2, as a function of the temperature scaled by critical temperature T_C. The arrows on the right side indicate the values for Stefan-Boltzmann limit.

distribution in this case should be essentially flat in the rapidity region between the two beams.

Fig 1.4 shows the space-time picture of evolution of the matter created in ultra-relativistic heavy ion collisions at RHIC with the longitudinal coordinate z and the time coordinate[35].

At t=0, free partons, mainly gluons are produced by a collision between two nuclei. The system is initially not in thermal equilibrium and the dynamics can be described by a cascade of colliding partons. The subsequent multiple parton scattering brings the matter to local equilibrium. If the deposited energy is large enough and exceeds the critical energy density, QGP is formed at the proper time $t = \tau_0$. The system will evolve like a fluid as it expands and cools down. At $t = \tau_C$, the system will reach the critical temperature between QGP and ordinary hadrons, and after mixed phase, the system consists of the ordinary hadrons interacting with each other at $t = \tau_H$. At $t = \tau_F$, each

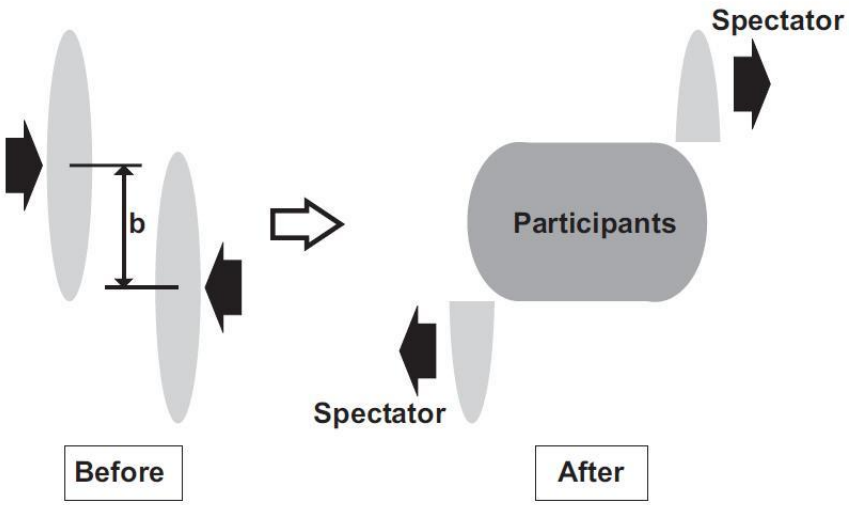

Figure 1.3: Schematic view of two colliding nuclei in the geometrical participant-spectator model.

hadron does not interact and produced particles are moving away. The final step of the reaction is the complete decoupling (freeze-out) of the hadrons after further expansion of the system.

1.2.1 Signature of QGP

The experimental search for QGP is complicated by the fact that it only has a fleeting existence and that any signal from QGP has to compete with background from hadron gas following by hadronization of plasma. There is no single signature that alone provides evidence for the creation of QGP and a variety of signatures together have to be taken into account when studying heavy-ion collisions in the light of QGP search. Those signatures have been already proposed before the startup of RHIC [36]. RHIC experiments have published four white papers [37–40] to review their results for possible signatures and a short summary of such signatures is given below.

Thermodynamical properties such as temperature, pressure, energy density and entropy of a system as well as their mutual dependence are directly influenced by a phase transition. The average transverse momentum of particle p_T in QGP phase is in principle related to the temperature of system. However, hadrons do interact after the chemical freeze-out from QGP in the hadron gas so that direct connection to the temperature is distorted. A better probe maybe provided by thermally produced dileptons and photons as they

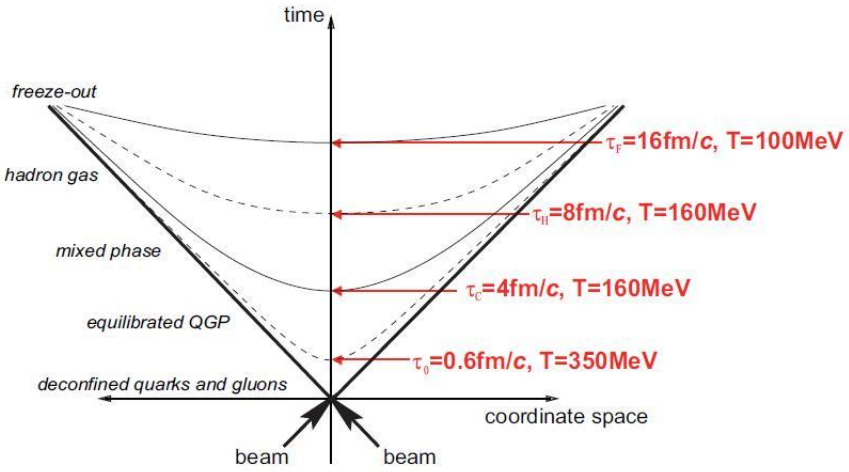

Figure 1.4: Space-time picture of a nucleus-nucleus collision. The times and temperatures for different phases are taken from [6].

do not suffer from strong final state interactions. They are created throughout all stages of the reaction from initial hard scattering to thermal production in QGP and hadron gas so they can provide direct information on the evolution of the fireball. Photons produced in hard scattering processes serve as an important test of binary scaling from $p+p$ collisions while thermal photons can be emitted from hot medium like QGP, both of which will be further explained in Section 1.4. Dileptons are produced in QGP phase by quark-antiquark annihilation which is governed by thermal distribution of quarks and antiquarks in plasma. This production channel has to be disentangled from the Drell-Yan production and the production in a hadron gas via process of $\pi^+\pi^- \rightarrow l^+l^-$[27]. By combining analysis of dileptons continuum mass spectrum and measurement of the ρ, ω and Φ mesons via their lepton decay branch, it provides an interesting probe for QGP phase as these mesons' mass might be influenced by chiral symmetry restoration. RHIC result showed an enhancement of e^+e^- paris below the ρ meson mass peak in 200GeV Au+Au collisions[41].

The entropy and energy density of the system is usually related to the measured particle multiplicity dN/dy and the transverse energy dE_T/dy at mid-rapidity. The hydrodynamical properties and the equation of state of the system can be studied through collective flow effects arising from pressure gradients in the asymmetric reaction zone, while the system size and lifetime of the reaction zone can be inferred from interferometry of identical particles, known as Hanbury-Brown-Twiss or HBT interferometry. Such HBT corre-

lations have been measured at RHIC[42, 43]. The resulting radius is of the order of $\sim 5fm$ which can be explained by improved theoretical models[44], including factors such as pre-equilibrium flow, a stiffer equation of state and adding viscosity.

The hydrodynamic properties of a medium can be investigated by its hydrodynamic flow, which can be addressed by the measurement of azimuthal anisotropy of particles at different momenta with respect to a so-called reaction plane. The reaction plane is the plane spanned by the impact parameter b and the direction of the colliding beams z. The anisotropy is generally described in terms of the parameter v_2 which is the second harmonic of the Fourier transformation of the angular distribution at a given p_T. The relatively large v_2 measured at RHIC[45, 46] suggests that the expanding fireball reaches the equilibrium rapidly. Initially the p_T dependency of v_2 is explained by hydrodynamic models assuming the existence of a perfect fluid with little or no viscosity[47, 48]. Recent theoretical studies indicate that the hexadecapole flow harmonic v_4 is a more sensitive constraint on the freeze-out dynamics[49] and the ratio $v_4/(v_2)^2$ indicate whether full local equilibrium is achieved in the QGP[50]. The precise measurements of charged hadron v_2 and v_4 at PHENIX [51] are consistent with the effects of finite viscosity and eccentricity fluctuations.

Other promising signatures for deconfined QGP phase include both enhanced production of strange quark because relatively low energy $\sim 300MeV/c^2$ is only needed for creation of a $s\bar{s}$ pair and J/Ψ suppression. As a bound $c\bar{c}$ state, J/Ψ is primarily produced in hard parton-parton scatterings due to its large mass of $3097MeV/c^2$. In QGP the attractive potential between a $c\bar{c}$ is screened by large density of free color chargs in the medium. At hadronization time the disassociated charm quarks couple with a larger probability to abundant lighter quarks than recombining to a J/Ψ.

1.3 Jet Quenching

At large transverse momenta, particles are usually produced in hard parton-parton scattering processes. In the QCD vacuum, the scattered partons subsequently fragment into jets. In collisions of heavy nuclei, the particles from initial hard scattering processes have to travel through the subsequently created hot and dense medium before fragmentation, therefore the jets can be used to probe the matter produced in such collisions[52]. A large energy loss in a colored medium was predicted in [53, 54]. It should distort the back-to-back correlation of particle jets and lead to a suppression of particle production called jet quenching at high p_T compared to p+p reaction.

1.3.1 Medium Effects

The amount of nuclear medium effect can be quantified using a nuclear modification factor R_{AA} which is the ratio between the measured yield and the expected yield from p+p result. It is defined as the following

$$R_{AA} = \frac{d^2N_{AA}/dp_T d\eta}{T_{AA}(b)d^2\sigma_{NN}/dp_T d\eta} \tag{1.3}$$

where denominator is the cross-section in p+p collisions scaled with thickness function $T_{AA}(b)$ in A+A nucleus-nucleus collision. R_{AA} is expected to be unity above certain p_T where hard scattering is the dominant source of particle production in the absence of any medium effects. $T_{AA}(b)$ is Glauber scaling factor defined as

$$T_{AA}(b) = \int d^2r T_A(r)T_A(r-b)T_A(r) = \int dz \rho_A(r,z) \tag{1.4}$$

The average number of binary nucleon-nucleon collisions $< N_{coll} >$ at an impact parameter b shown in Fig. 1.3 is given by $T_{AA}(b) =< N_{coll}(b) > /\sigma_{NN}$, where θ_{NN} is the total inelastic cross section. $T_{AA}(b)$ is analogous to an integrated "nucleon luminosity" for two overlapping nuclei. Since each centrality selection by the experiment samples a different distribution of impact parameters, the cross-section for a high-p_T particle produced in an A+A collision with certain centrality is linearly connected to p+p cross-section via the the average nuclear thickness.

In order to understand the nuclear modification factor in heavy-ion collisions and to quantify effects of hot nuclear matter, it is very important to know all other medium effects on particle production that are not due to presence of a hot and dense medium. Those effects include energy loss already for the passage through cold nuclear matter, enhanced particle production by multiple soft scattering and a modification of parton distribution function in initial state.

Cronin effect was observed by J.W. Cronin et al [55] in 1974 as one of known initial state effects that the cross-section does not simply scale with the number of target nucleons. Instead it scales like:

$$E\frac{d^3\sigma}{dp^3}(p_T, A) = E\frac{d^3\sigma}{dp^3}(p_T, 1) \otimes A^{\alpha(p_T)} \tag{1.5}$$

With $\alpha > 1$ for transverse momenta larger than approximately $2GeV/c$ hence there is an enhancement of particle production comparing to the expectation from $p + p$ collision, which can be explained as multiple soft scattering of incoming partons while passing through the nucleus and leading to a broad-

ening of the transverse momentum distribution.

Another known initial state effect, nuclear shadowing was discovered by the EMC group in 1982 that the structure function $F_2(x, Q^2)$ per nucleon in iron differs significantly from a free nucleon [56]. A highly energetic hadron has contributions to its wavefunction from gluons, quarks and antiquarks each of which has can carry some fraction of momentum with a probability. A convenient variable to describe the contribution of a parton to total hadron momentum is the fractional momentum x. A collection of data from different nuclei is shown in Fig. 1.5 where the nuclear effects are clearly seen. For $x < 0.2$ a reduction of $R^A_{F_2} = F^A_2/F^d_2$ called nuclear shadowing is observed. A small enhancement is seen between $0.1 < x < 0.2$ which sometimes is referred as anti-shadowing. The dip for $0.2 < x < 0.8$ was also first reported by the EMC group [56] and is usually called the EMC effect. The rise for larger x can be associated with Fermi motion of the nucleons inside nucleus [57].

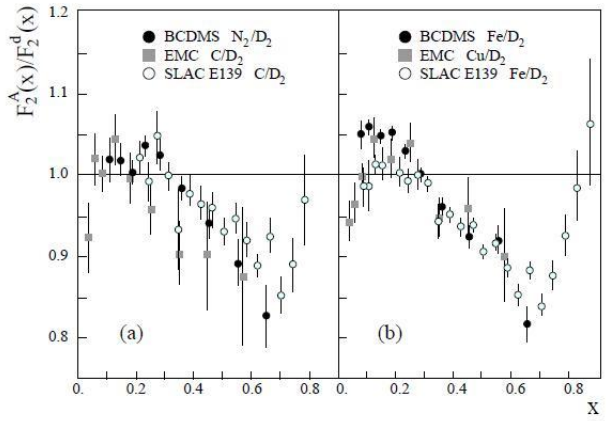

Figure 1.5: Ratio of structure function $F^A_2(x)/F^d_2(x)$ for nuclear targets A comparing to deuterium d measured in deep-inelastic electron (SLAC-139) and muon (BCDMS, EMC) scattering: (a) medium-weight targets, (b) heavier-weight targets.

The relevant x-region of scattered parton can be estimated by transverse momentum of leading hadron, which is the hadron carrying the largest momentum fraction of original scatter parton

$$x \sim \frac{2p_T}{\sqrt{s_{NN}}} \tag{1.6}$$

So that for RHIC energies and for transverse momenta up to 10GeV/c the shadowing region $x < 0.1$ is most relevant. Early predictions for jet quench-

ing at RHIC energies already considered this effect which can reduce nuclear modification factor by approximately 30% although a large uncertainty due to poorly known gluon contribution[58].

1.4 Direct Photon Production

Direct photons are all photons not originating from hadronic decays, e.g. $\pi^0, \eta \rightarrow \gamma\gamma$. They are usually further classified into prompt photons produced in early hard scattering and thermal photons emitted from thermally equilibrated phase. The examination of direct photons provides a tool to study different stages of heavy ion collision, especially the formation of quark-gluon plasma (QGP) since they are not influenced by strong interaction and hadronization processes.

In heavy ion collisions, high-p_T direct photons result mostly from hard scattering processes, which are insensitive to QGP evolution since they are not modified by the medium. The measurement in this p_T region provides valuable information about the initial yield from hard scattering. The comparison of photon yields in heavy ion to p+p collisions at high-p_T is also used to test the binary scaling behavior obtained from Glauber Model. Additional photons could be emitted from produced hot and dense thermal medium. The thermal radiation dominates at the low-p_T region of the spectrum.

1.4.1 Thermal Photons from QGP

Every thermal source emits thermal photon radiation so does QGP. The mean free path of photons in the QGP phase is large so they are not likely to interact ($\alpha_{EM} \ll \alpha_s$). In leading order (LO) perturbation theory real photons are produced via quark-antiquark annihilation ($q\bar{q} \rightarrow g\gamma$) and by quark-gluon Compton scattering ($qg \rightarrow q\gamma$). The corresponding Feynman graphs are shown in Fig. 1.6 together with an example of a higher order Bremsstrahlung process in which a quark radiates a photon.

In thermal field theory the technique to calculate the emission of direct photons from QGP has been developed since 1950s [59]. By assuming that the net baryon density is zero in QGP so that the quark distribution $f_q(E)$ and the antiquark distribution $f_{\bar{q}}(E)$ are the same, the thermal emission rate of photons with momentum p can be derived by following Eq. 1.7 both perturbatively [60, 61] and nonperturbatively [62].

$$E_\gamma \frac{dR}{d^3 p_\gamma} = \frac{-2}{(2\pi)^3} Im\Pi_\mu^{R,\mu} \frac{1}{e^{E/T} - 1} \tag{1.7}$$

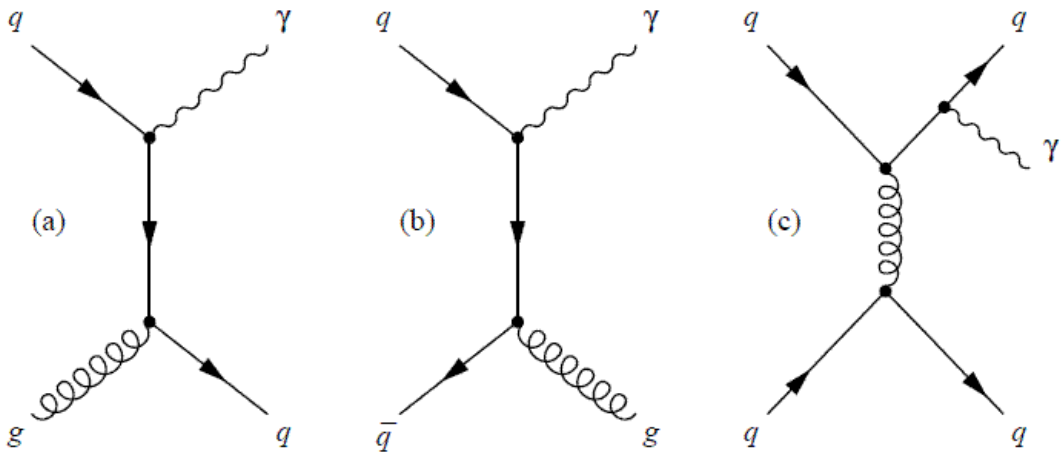

Figure 1.6: Feynman diagrams of the main production processes for direct photons in initial hard scatterings and thermalized quark-gluon plasma phase. (a) quark-gluon compton scattering of order $\alpha_s\alpha$, (b) quark-antiquark annihilation of order $\alpha_s\alpha$, (c) Bremsstrahlung of order $\alpha_s^2\alpha$.

where $\Pi_\mu^{R,\mu}$ is the retarded photon self-energy at finite T.

1.4.2 Thermal Photons from Hadron Gas

The calculation of thermal photon spectrum from fireball produced in heavy ion collisions involves also the contribution from hot hadron gas phase (HHG) following QGP. It is also needed as reference for a scenario without a phase transition, to see if the thermal photon spectrum can be used as a signature for QGP.

The emission rate of thermal photons from HHG can be treated very similar to QGP case discussed above. The rate is proportional to the imaginary part of photon self-energy with the difference that pions, η and ρ mesons constitute the loop corrections instead of quarks and gluons [63]. The coupling between the different vertices of the loop is determined by experimental observations such as decay rate for $\rho \to \pi\pi$. This effective coupling already considers higher-order effects e.g. vertex corrections. The cuts through the loop diagrams in Fig. 1.7 can be identified with the following relevant hadronic processes.

- $\pi^\pm\rho^0 \to \pi^\pm\gamma$

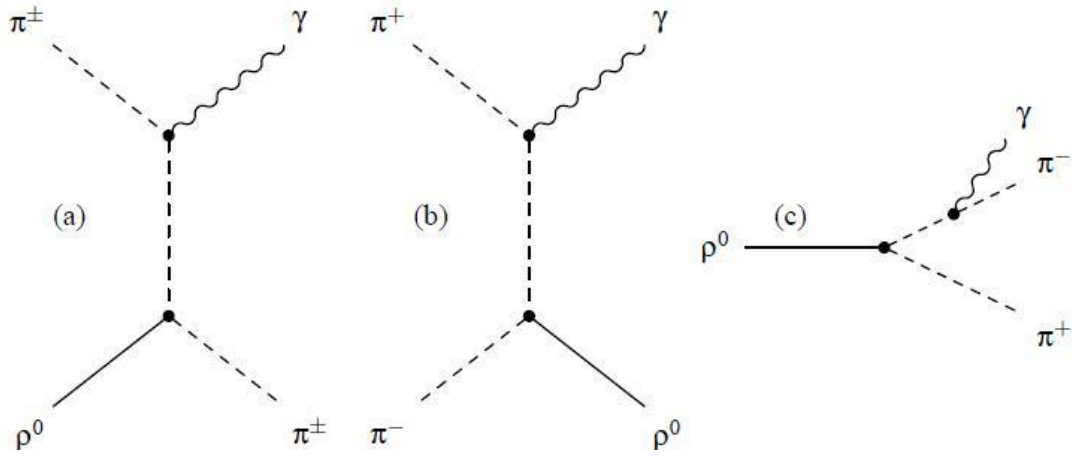

Figure 1.7: Examples of processes for the production of photons in a hadron gas: (a) $\pi\rho$ Compton scattering, (b)$\pi^+\pi^-$ annihilation, (c) ρ decay.

- $\pi^+\pi^- \rightarrow \rho^0\gamma$
- $\rho^0 \rightarrow \pi^+\pi^-\gamma$
- $\omega \rightarrow \pi^0\gamma$

Fig. 1.8 shows a recent result of theoretical calculation of photon emission spectra from central Au+Au collisions at RHIC energy [7]. The calculation assumes a temperature of 370 MeV and a formation time of 1/3 fm which includes all processes listed above and uses a massive Yang-Mills model of hadron interactions. The thermal photon spectra from hadron gas is similar to that emitted by QGP at the same temperature which is dominant at $1 < p_T < 3GeV/c$.

1.4.3 Prompt Photons

The main source of non-thermal direct photons are the prompt photons, which are produced in early hard scattering, similar to hadrons with large transverse momenta and are calculable via perturbative QCD invoking the factorization theorem equation. The basic underlying processes are the same as in the QGP shown as Fig. 1.6, with the main difference that the initial parton distribution is not given by the thermal distributions in the QGP but by the parton distributions in the incoming nuclei. The photon production in hard scattering is in principle not influenced by the uncertainty in the fragmentation

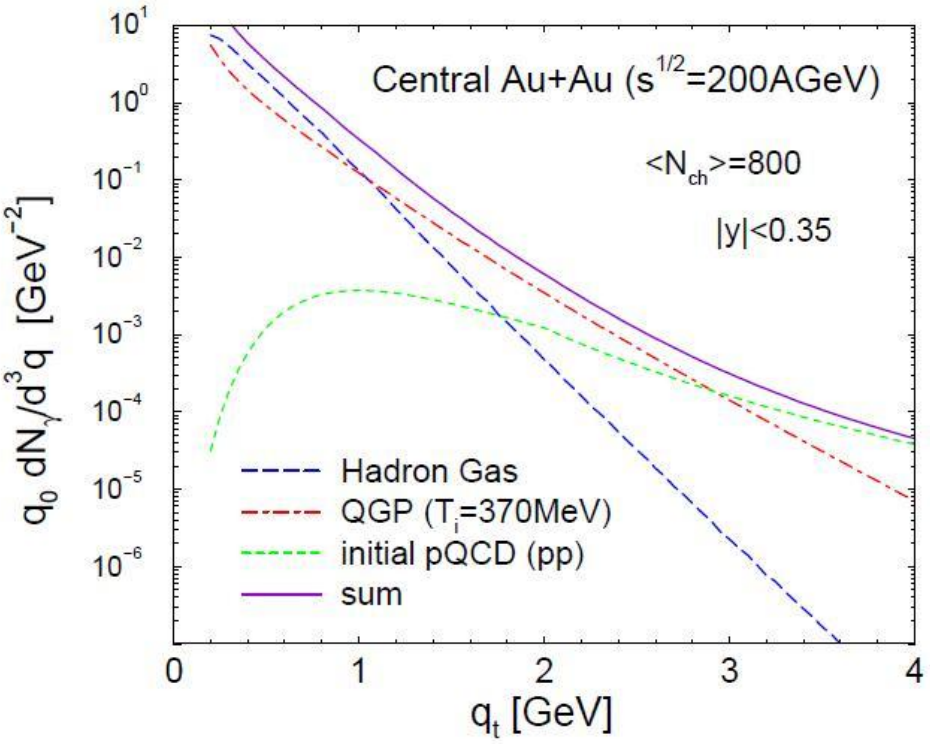

Figure 1.8: Theoretical calculation of photon emission spectra from central Au+Au collisions at RHIC energy by S. Turbide [7]. Short-dashed line: pQCD photons from hard scattering. Dashed-dotted line: thermal QGP radiation. Long-dashed line: thermal hadron gas emission. Solid line: total direct photon yield.

function as in the case of hadron production since it is a θ-function for photons. However, photons can also be produced during the fragmentation process of scattered partons.

Another possible source of non-thermal direct photons is from pre-equilibrium phase where theoretical description is rather difficult due to the uncertainties in the formation time of thermalized phase. It is often treated in parton cascade models for photon production, which combines pQCD with relativistic transport models.

The passage of high energy quark jets through the QGP leads to another source for non-thermal direct photons from jet-medium interactions [64]such as compton scattering with the thermal gluons ($q+g \rightarrow q+\gamma$) and annihilation with thermal antiquarks ($q+\bar{q} \rightarrow g+\gamma$), which may dominate the direct photon

production in the region below p_T=6GeV/c for Au+Au collisions at RHIC.

1.4.4 Earlier Direct Photon Measurements

The CERES(NA45) Collaboration first determined an upper limit on the direct photon yield relative to the decay photon yield in S+Au collisions in 1996 [65]. The first measurement of direct photons in heavy ion collisions has been reported by WA98 experiment at CERN SPS in central Pb+Pb collision at $\sqrt{s_{NN}} = 17.2GeV$ [66]. Fig. 1.9 shows the direct photon spectrum measured by WA98 and it can be interpreted as thermal radiation with initial temperature T_{init} $250MeV$.

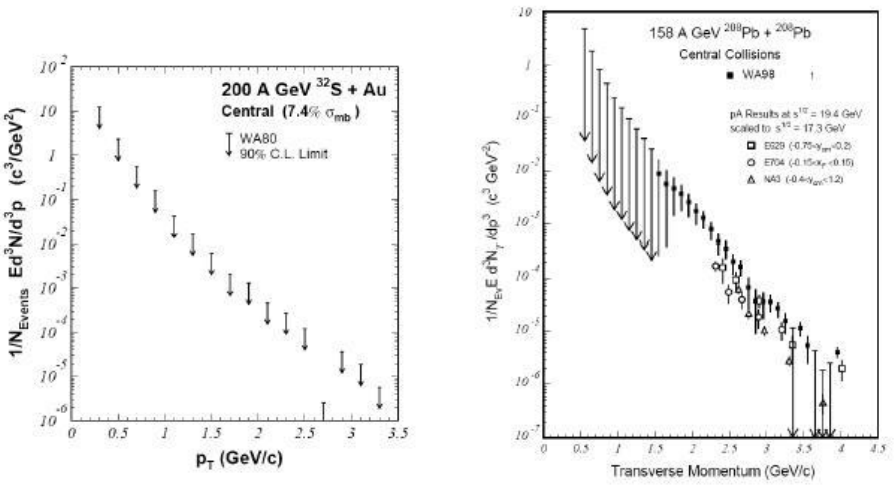

Figure 1.9: Two direct photon results in heavy ion physics before PHENIX measurement. The upper limit was set by WA80 [8] and the first measurement is by WA98 [9].

PHENIX made direct photon measurement up to $p_T \simeq 13GeV/c$ first time back in 2005 in Au+Au collisions at $\sqrt{s_{NN}} = 200GeV$ [1]. The invariant yields of direct photon in different centrality bins are shown in Fig. 1.10. The binary collision scaled predictions are seen to provide a good description of the measured direct photon spectra. The centrality dependence of the high p_T γ R_{AA} represented as a function of the number of participating nucleons, N_{part}, is shown in Fig. 1.11 which suggests that nuclear modification of the quark and gluon distribution function in the relevant region of momentum fraction x are minor. While high p_T direct photon production is observed to scale as p+p photon yield prediction for all centralities, π^0 R_{AA} shows a strong suppression

in more central collisions which is dominantly a final-state effect due to parton energy loss in the dense produced medium, rather than an initial-state effect.

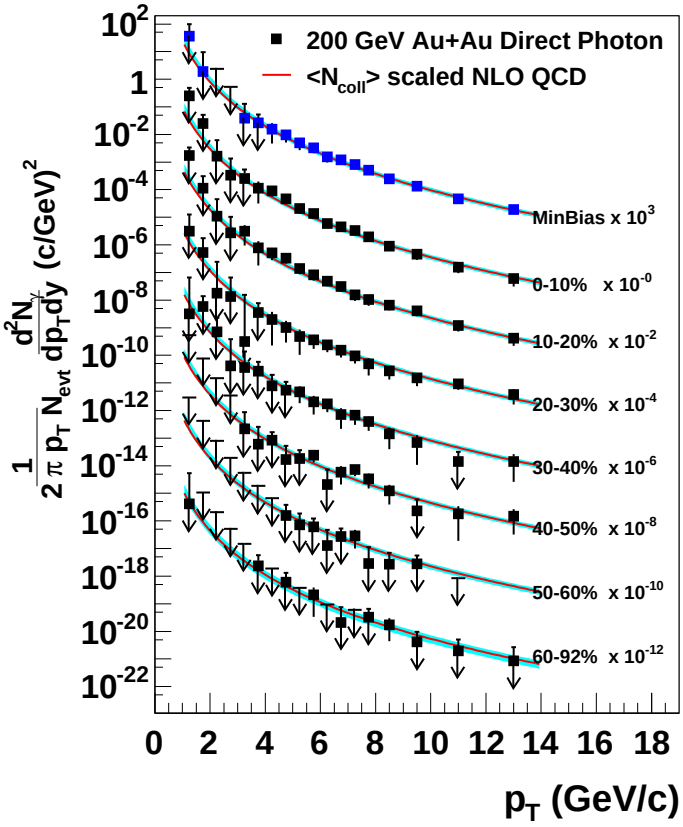

Figure 1.10: Direct photon invariant yields as a function of transverse momentum in different centrality bins. The vertical error bar on each point indicates the total error. Arrows indicate measurements consistent with zero yield with the tail of the arrow indicating the 90% confidence level upper limit. The solid curves are pQCD predictions [10].

However, the measurement of direct photons for $p_T < 3GeV/c$ is notoriously difficult due to a large background from hadronic decay photons. Direct photons contribute only $\simeq 10\%$ above the background photon yield [7] which lead to huge systematic uncertainties in early PHENIX direct photon measurement using a calorimeter. Measurement of photons with smaller energy using the same technique is not practical due to large background and deteriorating energy resolution. On the other hand, the momentum resolution of charged

particles becomes better towards lower p_T since they experience more bend in the magnetic field. Since any real photon can convert to an electron pair $\gamma \to e^+e^-$ and using the fact that PHENIX has excellent electron ID one can reconstruct low-momentum real photons if one can identify an electron pair from a photon conversion. There have been a lot of new successful attempts in recent years at PHENIX to utilize such advantage to measure low p_T direct photon yield by using photon samples from conversion.

Internal Conversion

The PHENIX experiment has measured direct photon yield in Au+Au at $\sqrt{s_{NN}} = 200GeV$ in the p_T region where the thermal radiation is expected ($p_T < 3GeV/c$) and compared it to the spectrum obtained from p+p collision [11] by reconstructing virtual photons from low mass e^+e^- pairs.

The idea of using low-mass lepton pairs as a method of direct photon measurement is not new. It was first used at CERN ISR in 1970's to set a limit on direct photon production [67]. At SppS collider at CERN, UA1 experiment measured low mass, high-p_T di-muon pairs, and their measurement is consistent with expectation of internal conversion of direct photon [68]. It is a good way to measure direct photon with much less hadronic background. The relation between photon production and the associated e^+e^- pair production is given by Eq. 1.8. By assuming $S = 1$, the direct photon yield can be obtained by dividing the yield of the excess e^+e^- pairs for $0.1 < m_{ee} < 0.3GeV/c^2$ before the conversion by a factor of $\frac{2\alpha}{3\pi} log\frac{300}{100} = 1.7 \times 10^{-3}$. All electrons and positrons with $p_T > 0.2GeV/c$ are combined into pairs. Pairs from photon conversions in the detector material are removed by a cut on the orientation of the pair in the magnetic field [69]. The combinatorial background is computed by mixing events and is subtracted by using the same method described in Section 4.4.1. The relation between photon production and the associated e^+e^- pair production can be written as [70].

$$\frac{d^3n_{e^+e^-}}{dmdp_Tdy} = \frac{2\alpha}{3\pi}\frac{1}{m}\sqrt{1-\frac{4m_e^2}{m^2}}(1+\frac{2m_e^2}{m^2})S\frac{d^2n_\gamma}{dp_Tdy} \tag{1.8}$$

where α is the fine structure constant, m_e and m are the masses of the electron and the e^+e^- pair respectively, and S is a process dependent factor that goes to 1 as $m \to 0$ or $m \ll p_T$. Since 80% of the hadronic photons are from π^0 decays, the signal to background ratio for the direct photon signal improves by a factor of five for $m > M_{\pi_0} = 135MeV/c^2$, thereby allowing a direct photon signal that is 10% of the background to be observed as a 50% excess of e^+e^- pairs.

The invariant yield is shown in Fig. 1.13. The direct photon spectrum

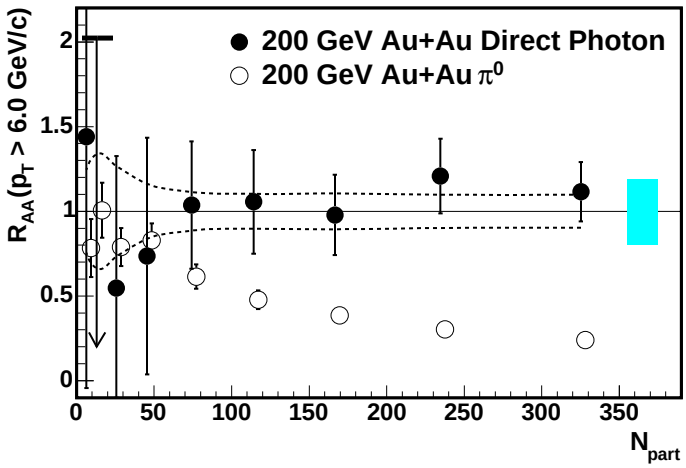

Figure 1.11: Ratio of Au+Au yield to p+p yield normalized by the number of binary nucleon collisions as a function of centrality given by N_{part} for direct photon (closed circles) and π^0 (open circles) yields integrated above 6GeV/c. The error bars indicates the total error excluding the error on $< N_{coll} >$ shown by the dashed lines and the scale uncertainty of the NLO calculation shown by the shaded region at the right.

in p+p collision is fitted with a modified power-law function. The minimum bias Au+Au collisions show larger photon yield in the low-p_T range when comparing with the T_{AA} scaled up p+p cross section. The excess yield in the $1 - 4GeV/c$ region in the most central Au+Au collisions can be seen in Fig. 1.12 and is fitted by an exponential function with an inverse slope of $T = 221 \pm 19^{stat} \pm 19^{syst} MeV$. If direct photons in Au+Au collisions are of thermal origin, the inverse slope T is related to the initial temperature T_{init}. In hydrodynamical models, the T_{init} is 1.5 to 3 times T due to space-time evolution [71, 72].

External Conversion

In Run7 and Run10 [73], PHENIX applied external conversion method for direct photon measurement by using HBD since it provides a well-defined conversion location for photons which leads to a characteristic apparent mass of a reconstructed conversion photon. The backplane of HBD is where GEM stacks and read-out boards reside so it is fairly thick, about 2% of a radiation length, which is a significant localized source of conversions compared to the rest of PHENIX subsystems. Electrons originating from the backplane of HBD, about $60cm$ from the interaction point, will be misconstrued if we

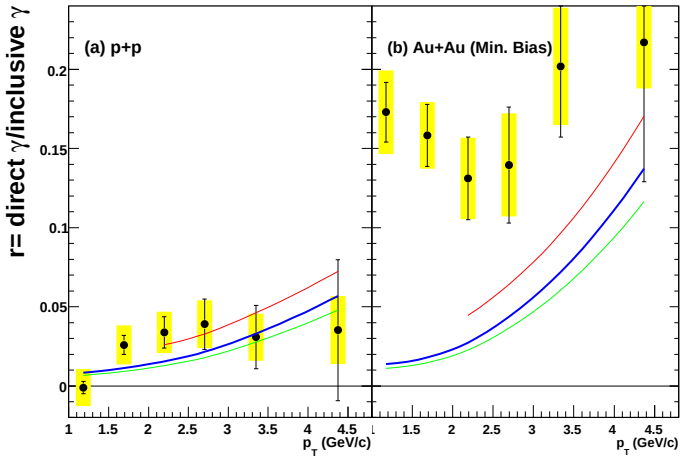

Figure 1.12: The fraction of direct photon component as a function of p_T. The error bars and the error band represent the statistical and systematic uncertainties respectively. The curves are from a NLO pQCD calculation.

incorrectly assumed it came from event vertex. However, we take advantage of this misconstruction and actually correct for it. In contrast to Run7, in Run10 HBD was installed for the whole data taking period and with a larger data set we hope to be able to get better results on virtual photon properties [74].

The amount of misconstruction depends on the radius of conversion. The track will be traced through the entire field map during reconstruction, even though it has passed through significantly less. The signature used to identify e^+e^- pairs that originate from an external photon conversion is the invariant mass of the pair. The angle of the opening plane of the pair relative to the magnetic field is used to discriminate conversions pairs from Dalitz pairs which the smaller magnetic field of the $+-$ configuration makes a less sensitive discriminator of conversion pairs. Hence a conversion recalibrator has been developed to increase our ability to select conversion pairs from the HBD electronics backplane by implementing an alternate track model (ATM) where we assume the particles came from the HBD backplane rather than the event vertex. The ATM is realized by studying Monte Carlo simulations and is simply a reparameterization of the reconstructed momenta with the alternate vertex assumption. The direct photon p_T spectra are shown in Fig. 1.14. Below $p_T = 3GeV/c$ an enhancement above expected prompt production is observed in all centrality bins. The enhancement has a significantly smaller inverse slope than the N_{coll} scaled p+p contribution which agrees with the

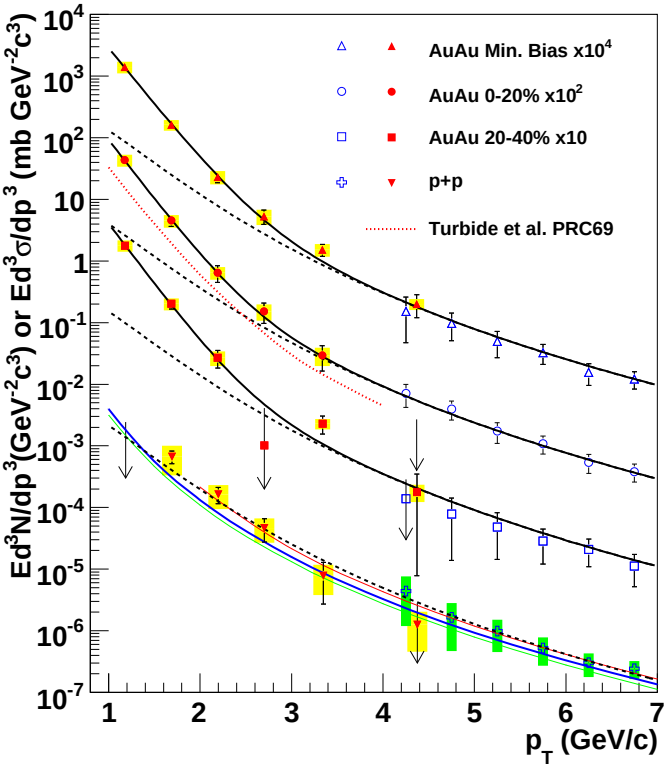

Figure 1.13: Invariant cross section (p+p) and invariant yield (Au+Au) of direct photons as a function of p_T. The filled points are from [11] and open points are from [1, 12]. The three curves on the p+p data represent NLO pQCD calculations and the dashed curves show a modified power-law fit to the p+p data scaled by T_{AA}. The dashed black curves are exponential plus the T_{AA} scaled p+p fit. The dotted red curve near the $0-20\%$ centrality data is theory calculation [7].

same measurement from internal conversion method.

Another interesting probe of the medium is the azimuthal anisotropy of the thermal photons. The photon flow depends on the temperature of the medium and the dynamical flow of the medium. The expected azimuthal anisotropy of direct photons from hydrodynamical models is small [7, 75, 76], as the large fraction of the photons comes from the QGP phase from early times where the flow of the medium is not formed yet. PHENIX has made the v_2 measurement on direct photon over a large momentum range $1 < p_T < 13 GeV/c$ [77] which is shown in Fig. 1.15. At high p_T ($> 6 GeV/c$) the direct photon v_2 is consistent

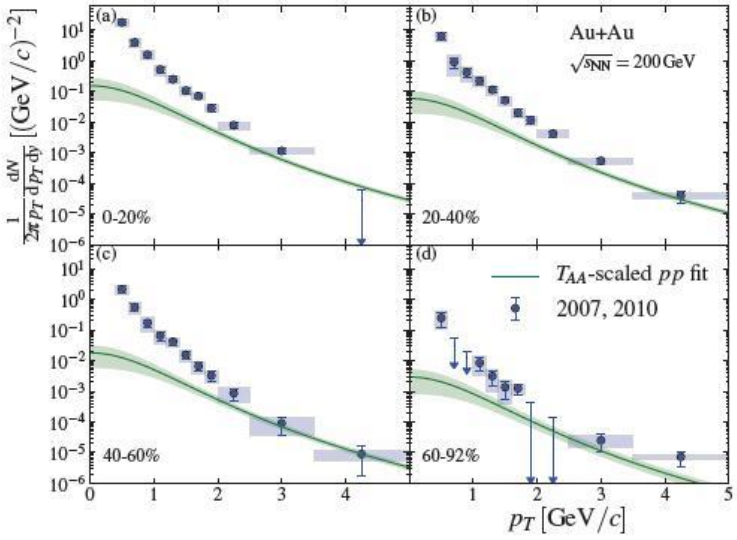

Figure 1.14: Direct photon p_T spectra in centrality bins $0-20\%, 20-40\%, 40-60\% and 60-92\%$ from PHENIX Run7 and Run10 external conversion analysis.

with zero as expected if the dominant source of photon production is initial hard scattering. In the thermal region ($p_T < 4GeV/c$), a positive direct photon v_2 is observed which is comparable in magnitude to the π^0 v_2 and consistent with early thermalization times and low viscosity. However its magnitude is much larger than current theories predict. The statistical and systematic uncertainties do not allow us to see evidence for any other processes that may contribute to a non-zero v_2 at this momentum range. One reasonable scenario to explain dilemma is that direct photon yield observed is indeed dominated by thermal radiation but the radiation mainly comes from late in the collision, giving the much larger v_2.

The purpose of this dissertation is to measure direct photons especially at medium-to-low momentum range with improved systematic uncertainties while still using photon sample from electromagnetic calorimeter as PHENIX measured in the first direct photon published result [1]. In order to minimize systematic uncertainties, a new method to measure direct photon fraction R_γ is proposed. Combined with more collision statistics provided by PHENIX Run4, this analysis provides an important cross-check on PHENIX direct photon measurement using different alternative approaches.

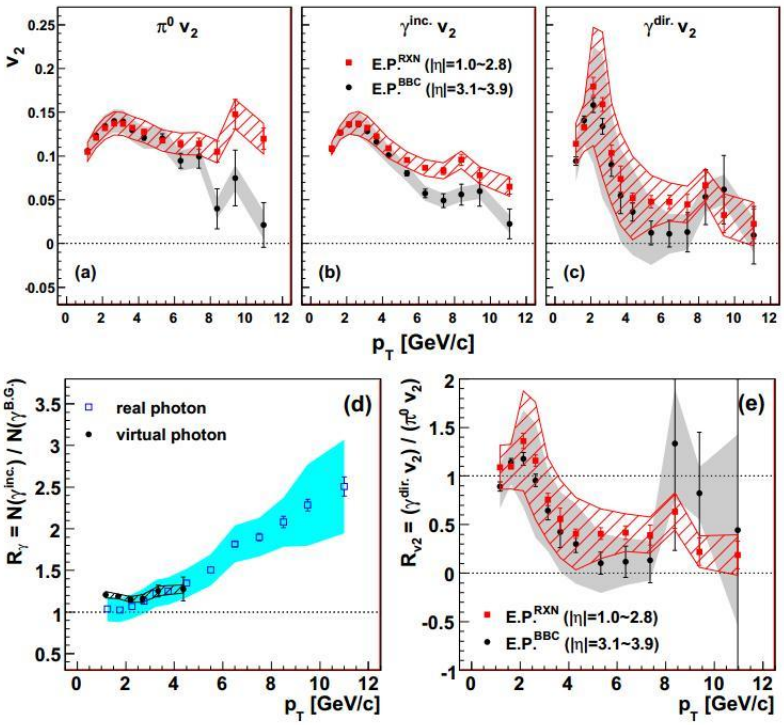

Figure 1.15: (top) v_2 in minimum bias collisions for (a) π^0, (b) inclusive photon and (c) direct photon. (bottom) direct photon fraction R_γ for virtual photons (solid black circles) and real photons (open blue squares) in (d) while ratio of direct photon to π^0 v_2 in (e). The vertical error bars on each data point indicate statistical uncertainties and shaded (gray and cyan) and hatched (red) area around the data points indicate sizes of systematic uncertainties.

Chapter 2

The PHENIX Experiment

This chapter will give a overview about Relativistic Heavy Ion Collider(RHIC) and its variety of detector systems, which allow us to study possible signatures of a deconfined phase of quarks and gluons in heavy ion collisions.

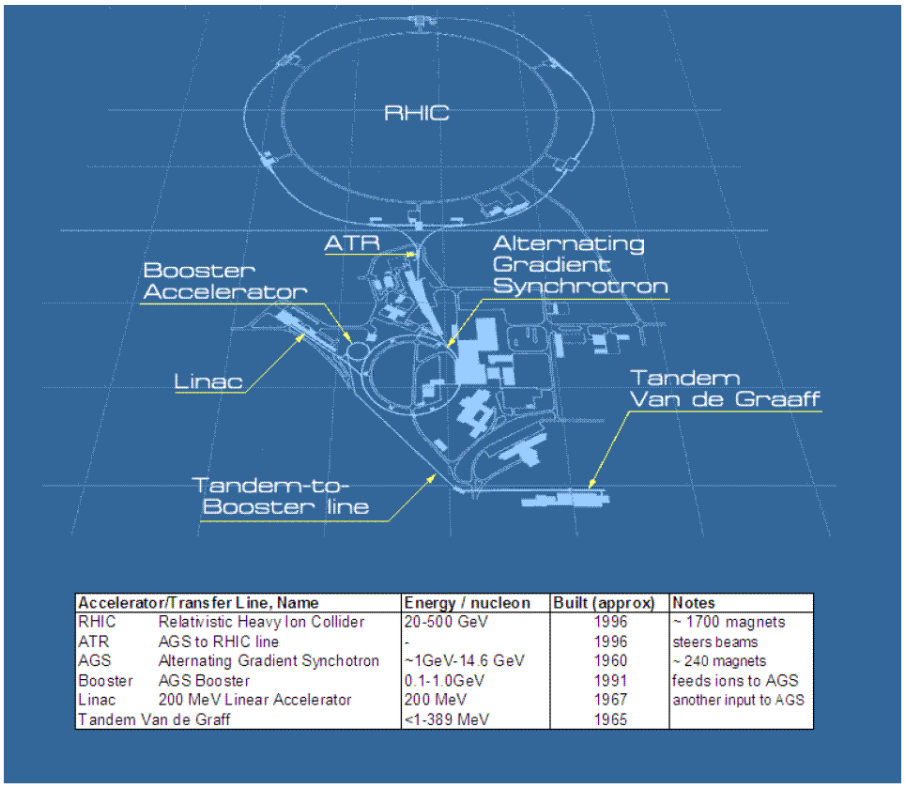

Accelerator/Transfer Line, Name		Energy / nucleon	Built (approx)	Notes
RHIC	Relativistic Heavy Ion Collider	20-500 GeV	1996	~ 1700 magnets
ATR	AGS to RHIC line	-	1996	steers beams
AGS	Alternating Gradient Synchotron	~1GeV-14.6 GeV	1960	~ 240 magnets
Booster	AGS Booster	0.1-1.0GeV	1991	feeds ions to AGS
Linac	200 MeV Linear Accelerator	200 MeV	1967	another input to AGS
Tandem Van de Graff		<1-389 MeV	1965	

Figure 2.1: The AGS-RHIC accelerator complex.

Injection Energy	$\gamma = 10.25(p = 9.5 GeV/c/nucleon)$
Storage Energy	$\gamma = 107.4(p = 100.0 GeV/c/nucleon)$
Bunch Intensity	1.0×10^9 Au ions/bunch
Number of Bunches	56 filled bunches
Transverse Emittance	$15\pi\mu m(normalized, 95\%)$
Longitudinal Emittance	$0.3 eVs/nucleon/bunch$
Interaction Diamond Length(r.m.s.)	$20cm$
Crossing Angle, Nominal(Maximum)	$0(\leq 1.7)$ mrad
Bunch Length	$15cm$
Bunch Radius	$0.2mm(\beta^* = 1)$
Luminosity Life Time	3 hours

Table 2.1: RHIC-AGS physical parameters

2.1 The Relativistic Heavy Ion Collider

The Relativistic Heavy Ion Collider(RHIC) at Brookhaven National Laboratory is a world-class scientific research facility that was proposed in 1983 initially and began operation in 2000 with colliding gold nuclei at a center of mass energy of $\sqrt{s_{NN}} = 130 GeV$, following 10 years of development and construction. For the analysis in this dissertation, data collected from RHIC Run4 Au+Au collisions at 200GeV in 2004 was used. The collider consists of two rings, denoted as yellow and blue, which accelerate the colliding particles in opposite directions. The energy per nucleon in each ring ranges from 2.5 [78] to 100 GeV/nucleon for heavy ions and up to 250 GeV for protons. Fig. 2.1 shows a schematic layout of RHIC accelerator complex.

2.2 PHENIX Overview

The PHENIX[79](Pioneering High Energy Nuclear Interaction eXperiment) is an advanced large spectrometer located in one of the 6 intersection points of the RHIC. It is a sophisticated detector system composed of 11 subsystems, which allows the measurement of hadrons, leptons and photons with excellent momentum and energy resolution. Another major advantage of the PHENIX experiment is the ability to study rare physics using Level-1 and Level-2 triggers to sample events with potential physics interest at the highest luminosity achieved at RHIC. Fig. 2.2 shows the PHENIX experimental setup in Run4(2004). The setup consists of four spectrometer arms – two around mid-rapidity(the central arms) and two at forward rapidity(the muon arms) – as well as a set of global detectors. The east and west central arms

are centered around rapidity zero with 90-degree coverage in azimuthal angle and are instrumented to detect electrons, photons and charged hadrons. The north and south forward arms have full azimuthal coverage and are utilized to detect muons. The global detectors measure the time and the position of the interactions, and the multiplicity of produced particles. Table 2.2 summarizes the rapidity and azimuthal angle coverage together with some basic physics characteristics of each subsystem.

Table 2.2: Summary of the PHENIX Detector Subsystems [20].

Element	$\Delta\eta$	$\Delta\phi$	Purpose and Special Features
Magnet: central (CM)	$\pm$0.35	360°	Up to 1.15 T·m.
muon (MMS)	-1.1 to -2.2	360°	0.72 T·m for $\eta = 2$
muon (MMN)	1.1 to 2.4	360°	0.72 T·m for $\eta = 2$
Silicon (MVD)	$\pm$2.6	360°	$d^2N/d\eta d\phi$, precise vertex, reaction plane determination
Beam-beam (BBC)	$\pm$(3.1 to 3.9)	360°	Start timing, fast vertex.
NTC	$\pm$(1 to 2)	320°	Extend coverage of BBC for p-p and p-A.
ZDC	$\pm$2 mrad	360°	Minimum bias trigger.
Drift chambers (DC)	$\pm$0.35	90°×2	Good momentum and mass resolution, $\Delta m/m = 0.4\%$ at $m = 1$GeV.
Pad chambers (PC)	$\pm$0.35	90°×2	Pattern recognition, tracking for nonbend direction.
TEC	$\pm$0.35	90°	Pattern recognition, dE/dx.
RICH	$\pm$0.35	90°×2	Electron identification.
ToF	$\pm$0.35	45°	Good hadron identification, σ <100 ps.
T0	$\pm$0.35	45°	Improve ToF timing for p-p and p-A.
PbSc EMCal	$\pm$0.35	90°+45°	For both calorimeters, photon and electron detection.
PbGl EMCal	$\pm$0.35	45°	Good $e^{\pm}/\pi^{\pm}$ separation at $p > 1$ GeV/c by EM shower and $p < 0.35$ GeV/c by ToF. $K^{\pm}/\pi^{\pm}$ separation up to 1 GeV/c by ToF.
μ tracker: (μTS)	-1.15 to -2.25	360°	Tracking for muons.
(μTN)	1.15 to 2.44	360°	Muon tracker north installed for year-3
μ identifier: (μIDS)	-1.15 to -2.25	360°	Steel absorbers and Iarocci tubes for
(μIDN)	1.15 to 2.44	360°	muon/hadron separation.

2.3 Global Detectors

There are two types of detectors in PHENIX[80] used to measure the global properties of the collision such as the impact parameter and the charged particle multiplicity. The one is beam-beam counter(BBC) and the other is Zero Degree Calorimeter(ZDC).

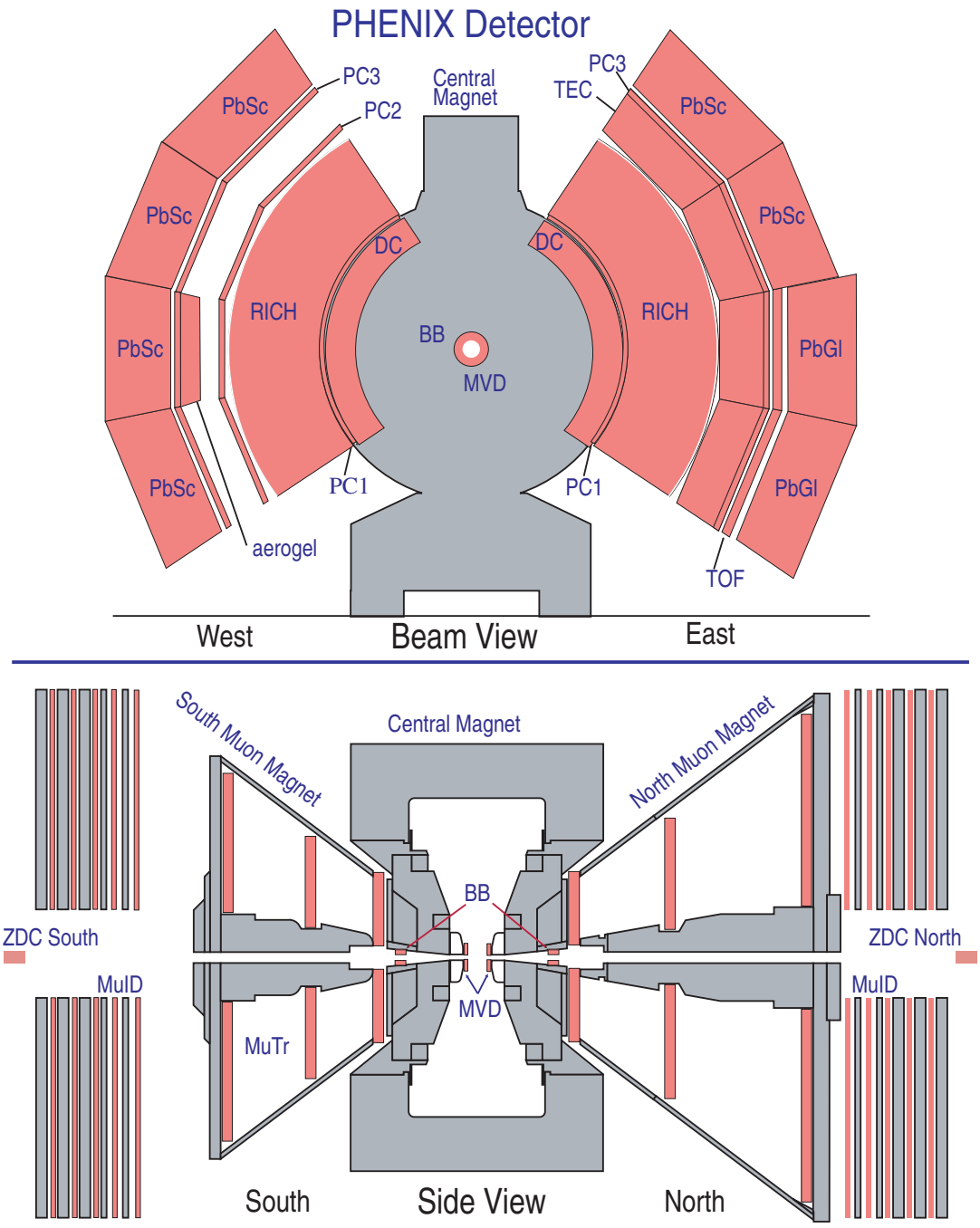

Figure 2.2: PHENIX Detector configuration for Run04(2004).

2.3.1 Beam-Beam Counter

The PHENIX beam-beam counters(BBC) were designed to provide the time at which a collision happens, to produce a signal on which to trigger data acquisition, to measure the position of a collision, and to determine the centrality of a collision along with the zero-degree calorimeter(ZDC). It is also used to determine collision orientation to the reaction plane. Each of BBCs consists of an array of 64 Cherenkov counters which are located $1.44m$ north and south respectively from the nominal collision point, as shown in Fig. 2.4 and Fig. 2.5. They cover very narrow cones around each beam($3.0 \leqslant \eta \leqslant 3.9$ with 2π azimuthal coverage). The inner(outer) radius of the BBC is $5cm(30cm)$, leaving about $1cm$ space from the beampipe. The BBC can be operated under various collision species ranging from 1 to 30 minimum ionizing particles, high radiation and large magnetic filled about $0.3T$.

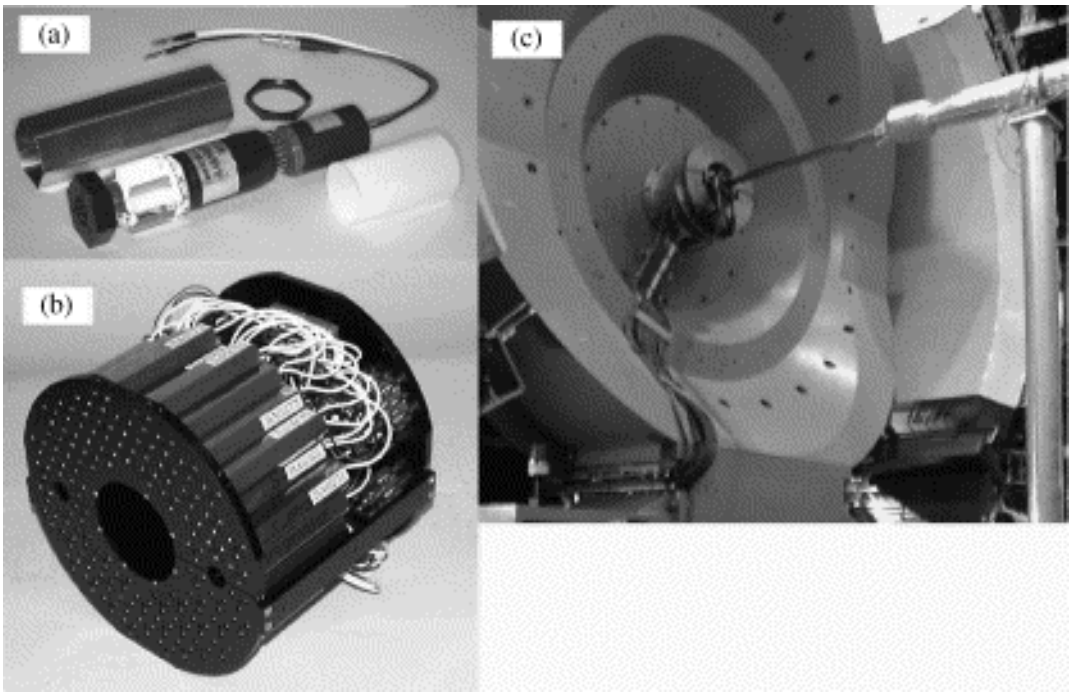

Figure 2.3: (a)Single BBC tower consisting of one mesh dynode photomultiplier tube mounted on a 3cm quartz radiator. (b)A BBC array comprising 64 BBC elements. (c)The BBC is shown mounted on the PHENIX detector. The beam pipe is seen in the middle of the picture. The BBC is installed on the mounting structure just behind the central spectrometer magnet.

Each PMT has a timing resolution of $50ps$. The collision vertex can be found by looking at the difference in the average hit time over the PMTs

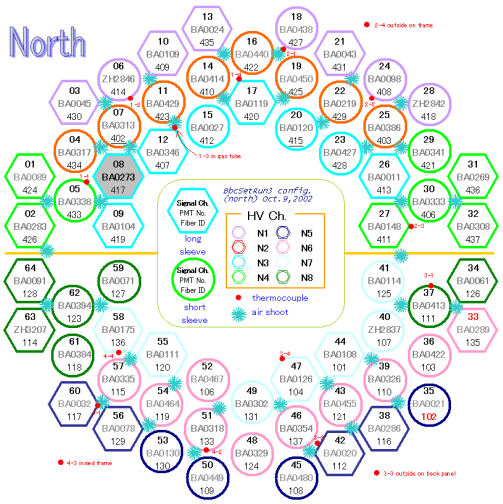

Figure 2.4: Schematic of BBC North in Run-4, with each box corresponding to a PMT.

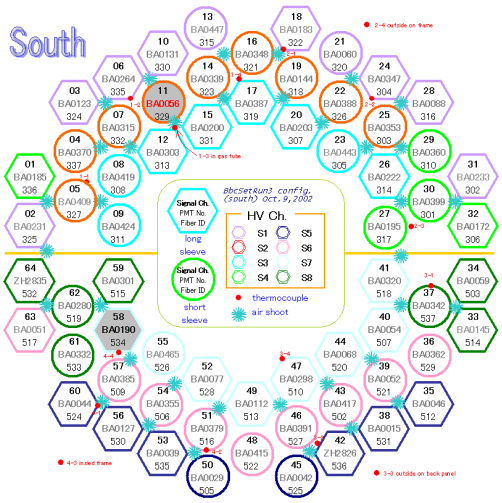

Figure 2.5: Schematic of BBC South in Run-4, with each box corresponding to a PMT.

between the north and south BBC. In p+p collision, the vertex resolution in the beam direction is $1.2cm$, while in central Au+Au collisions the resolution is $0.3cm$. The PHENIX Level-1 trigger accepts signals if the BBC vertex is within $50cm$ of the center of PHENIX, in order to avoid interactions of particles with the magnet poles, scattering particles into the central arm acceptance. Since this trigger is efficient for most interaction processes, it is also referred to as a "Minimum-bias" trigger. Due to the 3 units of rapidity gap from mid-rapidity, the reaction plane determined by the BBC is less sensitive to the non-flow[81] effects in the PHENIX central acceptance.

2.3.2 Zero Degree Calorimeter

The zero degree calorimeters(ZDC) are installed about $18m$ from the center of PHENIX with an angular acceptance of $\mid \theta \mid \leqslant 2mrad$. They are small transverse area hadron calorimeters that are used to measure spectator neutrons from nucleus-nucleus collisions. Because they are located in the beam line behind the beam bending magnets, charged particles such as protons are deflected out of the ZDC acceptance leading to a measurement of neutron energy with very low background. Each single ZDC consists of 3 modules with a depth of 2 hadronic interaction lengths, which then are read out by a single PMT. Both time and amplitude are digitized for each of the 3 PMTs, and an

analog sum is determined of all 3 PMTs for each ZDC. The energy resolution at the one neutron peak is approximately 21%[82]. The intrinsic timing resolution is about $150ps$ and the ZDC vertex can be measured with a resolution of $3cm$.
For both the ZDC and the BBC, the time and vertex position are determined by measuring time difference between the north and the south detectors and the known distance between the two detectors. The start time(T_0) and the vertex position(z_{vtx}) along the beam axis are obtained as:

$$T_0 = \frac{T_N + T_S}{2} - z_{N-S}c, \tag{2.1}$$

$$z_{vtx} = \frac{\mid T_N - T_S \mid}{2} \times c \tag{2.2}$$

wherez_{N-S} is the distance between the north and south detectors, T_N and T_S are the average measured time of arriving particles at North and South, respectively. Fig. 2.6 shows that there is a strong correlation between the vertex by BBC and by ZDC.

Since the multiplicity of both the neutrons in the ZDC and the charged particles in the BBC are correlated with the collision geometry shown in Fig. 2.6, they can also be used to measure the collision centrality(impact parameter $|b|$). While the ZDCs measure forward neutrons that result from fragmentation of the colliding nuclei(mostly spectators), the BBCs are sensitive to charged particles produced in the collisions by participants. Together, both detectors provide valuable information on the impact parameter of the nuclear interaction. These observables, combined with a Glauber model for the collision geometry, allow us to determine different centrality classes.

2.4 Central Arm Detectors

Although the majority of this thesis is based on measurements made by PHENIX EMCal, which is only one detector layer of PHENIX central spectrometers, we will briefly explain the rest of detectors each of which has different roles and advantages in terms of particle tracking and identification. Charge particles tracking and detection is used in this thesis to remove unwanted charge particle contamination from our photon samples-charge particle veto by utilizing Pad Chamber. Since 2004, more detectors have been added to the central spectrometer, namely another time-of-flight detector in the west arm (TOF-W) and hadron-blind detector (HBD).

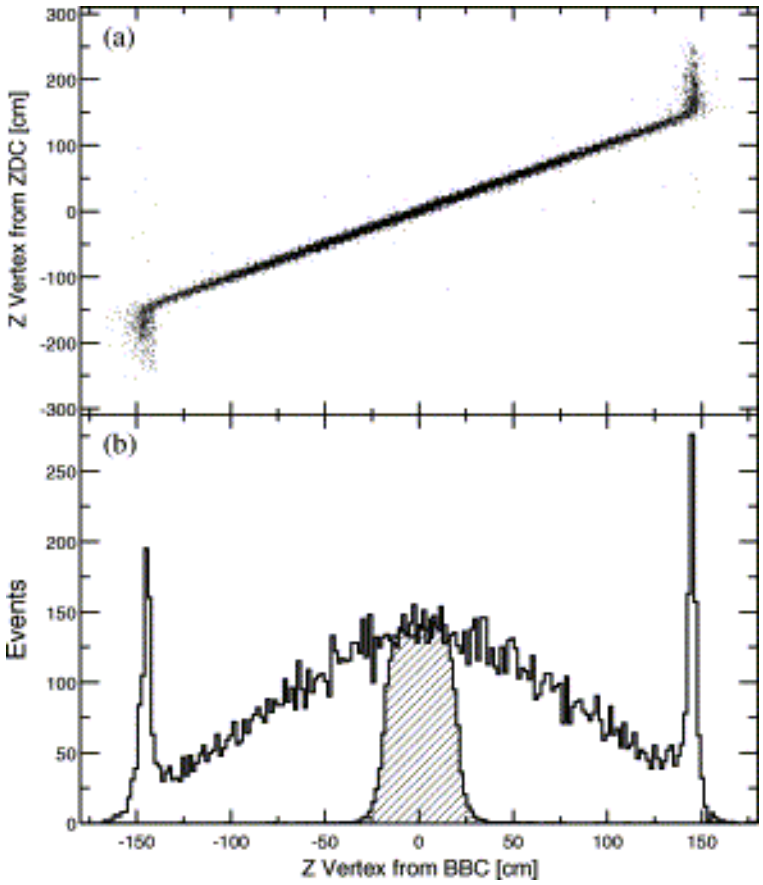

Figure 2.6: (a)Correlation of determined ZVTX between BBC and ZDC. (b)ZVTX distribution from BBC. Hatched area corresponds to the events satisfying the PHENIX Local LVL1 trigger condition.

2.4.1 The Central Magnet System

The transverse momentum of charged particles is determined by their trajectory bending in the magnetic field provided by the Central Magnet (CM) [83]. It consists of two coils that can be operated independently and yield an axial magnetic field of $\int Bdl = 0.43 - 1.15Tm$ over the first $2m$ from the interaction point, depending on the current setup of the magnet. Magnetic field in the region of other tracking devices ($R > 2m$) is nearly zero in order to allow a tracking model which assumes straight tracks and to minimize the smearing of Cherenkov rings in the Ring Imaging Cherenkov Counter. The $+-$ configuration leads to a cancellation of the field in the first 50cm around the vertex to approximately zero field integral, which is used in combination with HBD

[84, 85].

2.4.2 Drift Chamber

Two Drift Chambers (DC) located in each arm are the main tracking detector for charged particles in PHENIX. They measure the deflection of charged particles in the magnetic field of CM with a resolution about $150\mu m$ in the $r-\phi$ plane to determine the momentum of single particles and the invariant mass of particle pairs. Each of them consists of a multiwire gas chamber at a distance of 2.02m to 2.40m from the interaction point outside of magnetic field of CM. When a charged particle traverses through DC, it randomly ionizes the gas and electrons from primary ionization process are drifted in an electrical field towards an anode sense wire after a time proportional to the distance of the track to the wire. Hits in subsequent anodes then can be reconstructed to form the track.

DC also provides position information for pattern recognition and tracking of charged particles through the various detectors of central arms up to 500 tracks [86] by separating each sense wire into two halves at the center to read out independently. To electrically isolate the two halves, they are connected by a $100\mu m$ thick Kapton strip. In total DC has 6500 wires and hence 13000 readout channels.

2.4.3 Pad Chamber

The Pad Chambers (PC) are multiwire proportional chambers outside of central magnet with a cathode pad readout that determine space points along the straight trajectory of charged particles to determine the polar angle θ which allows reconstruction of $\hat{z}$-component of the momentum vector. The Central Arms are equipped with three layers of PC in the west arm and two layers in the east arm. The first layer of Pad Chambers (PC1) is installed just behind the Drift Chambers, while the third layer (PC3) is located right in front of Electromagnetic Calorimeter. The second layer of Pad Chambers (PC2) is only present in the west arm following the Ring Imaging Cherenkov Counter [86].

2.4.4 Ring Imaging Cerenkov Detector

The Ring Imaging Cherenkov Detector (RICH) plays a major role for electron identification. Located in both arms, it is composed of gas volume of $40m^3$. Charged particles with velocities larger than the speed of light βc in a medium with refractive index n will emit Cherenkov radiation under angle

of $cos(\theta_C) = 1/(n\beta)$. Due to different thresholds for electrons and pions to generate Cherenkov radiation, with CO_2 as radiator gas, no pions are detected below $p = 4.65GeV/c$. Therefore RICH provides a good separation of these two particles species [87].

2.4.5 Electromagnetic Calorimeter

The outermost detector of the central arms, with a radial distance of more than $5m$ from beampipe, is the Electromagnetic Calorimeter(EMCal)[14]. It consists of six sectors of lead-scintillator sandwich calorimeter(PbSc) and two sectors of lead-glass Cherenkov calorimeter(PbGl). Each sector covers 22.5° in azimuthal direction. With their fine segmentation ($\Delta\eta \times \Delta\phi \approx 0.011 \times 0.011$ for PbSc and 0.008×0.008 for PbGl) both calorimeters can provide a excellent energy and position resolution for photons and electrons measurement. The calorimeters will be described thoroughly in Chapter. 3.

2.4.6 Time of Flight

The Time-of-Flight spectrometer (TOF) is only installed in front of two sectors of lead-glass calorimeter, which covers only a small angular range of $\delta\phi \approx 45°$. It allows PHENIX to distinguish between kaons and protons up to $p_T = 4GeV/c$ and pion/kaon separation up to $p_T = 2.4GeV/c$ with timing resolution of $\approx 100ps$ [87].

2.5 PHENIX Data Acquisition System

PHENIX data analysis not only requires a versatile detector system with specialized subsystems, but also a flexible and robust data acquisition (DAQ) and triggering system that can handle the high interaction rates of approximately 500kHz in p+p collisions and the large event size in high multiplicity Au+Au events at a rate of a few kHz [88]. Basically two different trigger systems are implemented at PHENIX. The Level-1 (LVL1) triggers are controlled by RHIC beam clock with a rate of 9.43MHz. This clock also steers the lower levels of the parallel readout at PHENIX. The Level-2 (LVL2) triggers, on the other hand, are driven by decisions on the measured data so they are applied after an event already has been processed to a certain level.

A full overview of DAQ system describing general flow of data as well as control signals is shown in Fig. 2.7. The data of each event passing certain selected trigger threshold, e.g. the LVL1 trigger, are transfered to the Data Collection Modules (DCMs) [88] in the counting house by optical fibers. DCMs

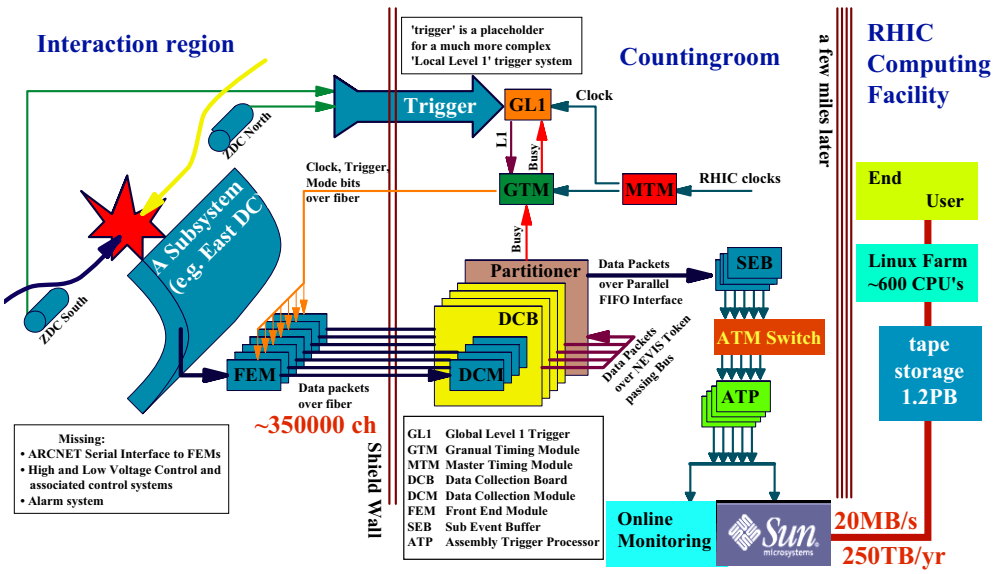

Figure 2.7: Block diagram of DAQ at PHENIX.

collect approximately 375000 channels and format, zero suppress, and check them in parallel. Each of DCMs has four data input streams and serves four Front End Modules (FEMs). Up to five events can be buffered in DCMs before being processed to the Event Builder (EvB). The Granule Timing Module (GTM) is used to control the FEM readout and provides the clock from central RHIC clock to different Granules. EvB is the final system in DAQ where final event assembly is performed in PHENIX before the data are sent to PHENIX Online Control System (ONCS). EvB collects the fragments from each data stream and assembles them into complete events. EvB consists of a set of Sub-Event Buffers (SEBs) that are used to read out the different Granule settings independently. After checking, data are transfered from SEBs to the Assembler/Trigger Modules (ATMs), where LVL2 trigger can be applied to data and data rate is also reduced by this. If the trigger decision is positive, the event is assembled, putting together the different data streams. Finally events that are assembled, are stored on disk for online monitoring and eventually archived at the RHIC Computing Facility (RCF) on a High Performance Storage System (HPSS), a tape-based storage system.

2.6 RHIC ATLAS Computing Facility

In addition to the accelerator complex itself, we have a computing farm dedicated to RHIC data analysis at BNL called the RHIC ATLAS Computing Facility(RACF). It began with the RHIC Computing Facility(RCF) which was established in the 1990's to support the computing needs of the four experiments(BRAHMS, PHENIX, PHOBOS and STAR) at the RHIC. In the mid 1990's, BNL was selected as the U.S. Tier 1 computing facility for the ATLAS experiment at the LHC(CERN). The ATLAS Computing facility(ACF) was then set up on the ideas of a global computing grid, resulting in the RACF. The major components of the RACF are the 14 TFLOPS processing farm (currently with over 4000 processors), the distributed and centralized disk storage farm (1 PB of on-line disk storage), the robotic tape storage silos (7 PB of storage) and the grid computing software infrastructure. The hardware is a combination of commodity-based processing servers, enterprise-class UNIX servers and highly-specialized mass storage systems connected together by a high-speed network infrastructure.
PHENIX also houses a smaller 75 single dual and quad processor machine farm called PHENIX Online Computing Systems(PHONCS) in its counting house for fast online analysis. Occasionally even more computing power has been necessary to meet the computing demands of the ~ 500 collaborators of PHENIX. For this additional resources have been allocated for PHENIX use by the Riken Institute in Japan(CC-J) and at Subatech Research Institute in Franch(PHENIX-France).

Chapter 3

The Electromagnetic Calorimeter at PHENIX

Since the Electromagnetic Calorimeter (EMCal)[14] is the major part of detector subsystems used in this analysis, a separate chapter is devoted to its description. Located at the outermost layer of the central arms in PHENIX, it covers the full central spectrometer acceptance of $70^o \leqslant \theta \leqslant 110^o$ with two walls, each subtending $\Delta\phi = 90^o$ in azimuth. The west wall comprises four sectors of a Pb-scintillator sampling calorimeter (PbSc) and the east wall has two sectors of Pb-scintillator and two of a Pb-glass Cherenkov calorimeter (PbGl). The PbSc is installed at a radial distance of 5.1m behind the PC3 and the PbGl is located behind the TOF at a radial distance of 5.4m. The properties of the PbSc and PbGl calorimeters are very different and they have different advantages and disadvantages. For example, the PbGl has the better granularity and energy resolution while the Pb-scintillator has the better linearity and timing and the response to hadrons is better understood. The different types of detectors with their different systematics can provide a good cross-check of each EMCal measurement therefore increase the confidence level of the physics results.

PHENIX's EMCal has been optimized to measure the spatial position and energy of electrons and photons produced in heavy ion collisions, therefore neutral mesons such as π^0 through the reconstruction of decay particle pairs invariant mass. This is accomplished by the high segmentation in rapidity and azimuthal direction ($\delta\eta \times \delta\phi = 0.011 \times 0.011$ for PbSc and 0.008×0.008 for PbGl). The EMCal can also be used for the determination of the total transverse energy E_T in a heavy ion collision because charged as well as neutral particles deposit at least a fraction of their energy in the EMCal. The particle identification is provided by the excellent timing resolution, in particular of the PbSc, which allows time-of-flight measurements to distinguish photons

Quantity	Value
Geometry	384 Super Modules
Number of SM per sector	192 (16 wide by 12 high)
Number of modules per SM	24 (6 wide by 4 high)
Total number of modules	9216
Module gront surface	$4cm \times 4cm$
Module length	$40cm(14.4X_o)$
Mylar foil thickness	$12\mu m$
Shrink tube thickness	$150\mu m$
Super module front surface	$24.6 \pm 0.02cm.4 \pm 0.02cm$
Pb-glass type	TF1
Pb-oxide content	51%
Density	$3.85g/cm^2$
Weight per module	2.46 kg
Index of refraction	1.648
Total internal reflection angle	36°
Radiation length X_0	2.8 cm
Moliere radius	3.68 cm
Interaction length	38.0 cm
Critical energy	16 MeV

Table 3.1: Lead-glass physical parameters

and electrons from hadrons. The EMCal also offers the unique opportunity to identify antineutrons within PHENIX by measuring their annihilation energy deposited in the calorimeter. This is crucial for the background determination in the analysis of direct photons especially in low p_T range. At last but no least, like all calorimeters, the EMCal at PHENIX provides fast information on particle energy therefore is highly suitable for the trigger system.

3.1 Lead Glass Calorimeter

The Pb-glass calorimeter was previously used in the CERN experiment WA98 [89] where direct photons were measured successfully for the first time in heavy ion collisions. Then it was disassembled and shipped to BNL where it was installed in the PHENIX experiment. The two PbGl calorimeter sectors occupy the lower part of the east central arm of PHENIX. Each PbGl sector comprises 192 so-called supermodules(SM) and each SM forms a self-contained detector with its own reference system(see Fig. 3.1), which allows the easy reassembly

of the detector in a different geometry and does not require a complete new calibration. One PbGl SM contains 24 PbGl modules in a array of 6×4. Each PbGl module is $40 \times 40 \times 400mm$ in size and individually wrapped with carbon fiber and epoxy resin to form a self-supporting SM with a shared calibration system. The physical properties of the employed PbGl module are summarized in Table 3.1. Steel sheets of $0.5mm$ in thickness were used to house the phototubes and bases. The sheets were incorporated during the gluing process. An aluminized plastic foil on the front of the SM contains a hole for each PbGl module which allows entry for the LED light used for gain monitoring. A polystyrene reflective dome encloses the LED system on the front surface of the SM.

The response of PbGl was studied extensively in test beams at the AGS(BNL) and SPS(CERN) to investigate the performance of the device with respect to energy, position and timing measurement [90]. The energy resolution can be fit with the parameterizations $\sigma(E)/E = ([5.9 \pm 0.1]\%/\sqrt{E/GeV}) \oplus [0.8 \pm 0.1]\%$. The position resolution does not show a significant angular dependence and can be parameterized as $\sigma_x(E) = [0.2 \pm 0.1]mm \oplus [8.4 \pm 0.3]mm/\sqrt{E/GeV}$ [14].

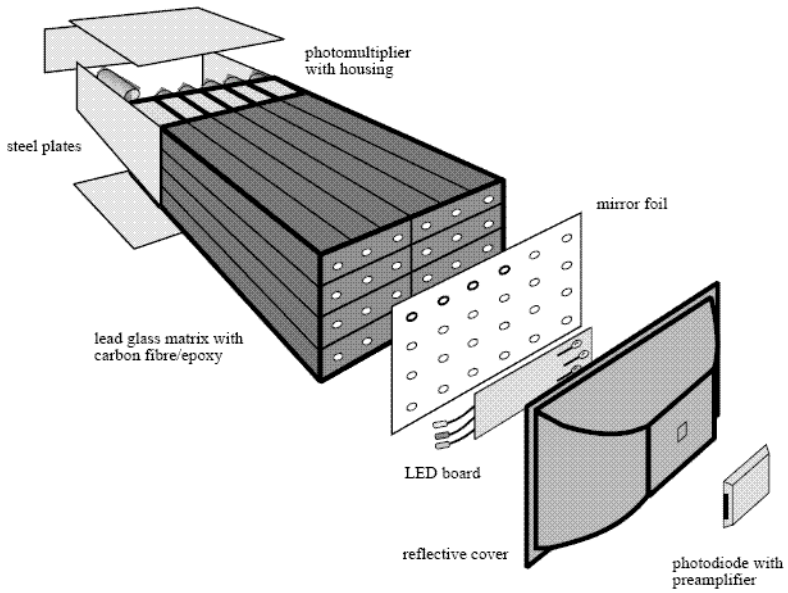

Figure 3.1: Exploded view of a lead glass calorimeter supermodule.

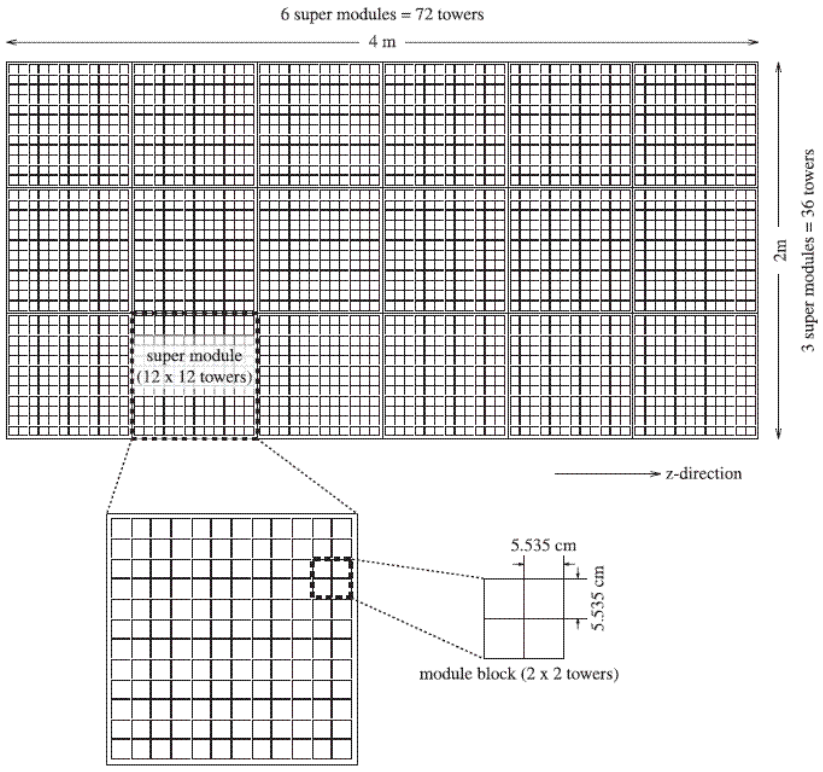

Figure 3.2: Surface view of a PbSc sector which consists of 6×3 super modules. A super modules consists of 12×12 towers.

3.2 Lead Scintillator Calorimeter

The lead-scintillator electromagnetic calorimeter(PbSc) for the PHENIX experiment is a shashlik type detector consisting of 15552 individual towers and covers an area of approximately $48m^2$. There are four sectors of them in the west central arm and two sectors in the east arm of PHENIX. The PbSc is mostly used to determine the energy deposited of a particle by collecting scintillation light produced at various depths in the detector.

The basic building block is a module which comprises four optically isolated towers and each tower is read out individually as shown in Fig. 3.3. The surface size of a tower element is $5.54 \times 5.54cm^2$. All the towers are organized into $6 \times 3 = 18$ "super modules" to form a single sector(Fig. 3.2). A super module consists of 6×6 PbSc building block. Thirty-six module blocks are then attached to a backbone and held together by welded stainless steel skins on the outside and one rigid structure of super module is formed. As the smallest unit within PbSc, one tower contains 66 sampling cells consisting of

Parameter	Value
Lateral segmentation	$5.535 \times 5.535 cm^2$
Active sampling cells	66
Scintillator	Polystyrene (1.5% PT/0.01% POPOP), 0.4 cm
Absorber	Pb, 0.15 cm
Cell thickness	0.56 cm (0.277 X_o)
Active depth	37.5 cm
Radiation length	18 X_0
Nuclear interaction length	0.85
WLS fiber	BCF-99-29a, 0.1 cm
WLS fibers per tower	36
PMT type	FEU115M, MELS, Russia, 3.0 cm
Photocathode	Sb-K-Na-Cs
Luminous sensitivity	$\geqslant 80 \mu a/lm$
Rise time (20-80%)	$\leqslant 5ns$

Table 3.2: Individual Pb-scintillator calorimeter tower parameters

alternating tiles of Pb and scintillator. The edges of the tiles are plated with Al. These cells are optically connected by 36 longitudinally penetrating wavelength shifting(WLS) fibers for light collection. Finally the scintillation lights are read out by $30mm$ FEU115M phototubes at the back of the tower. All major PbSc design parameters are listed in Table 3.2. The scintillating plastic contains an organic scintillator p-bis[2-(5-phenyloxazolyl)]-benzene (POPOP) and a fluorescent additive p-terphenyl (PT).

The PbSc calorimeter went through a rather extensive sequence of preconstruction tests in the particle beams from U70(IHEP, Protvino) from the AGS(BNL) and finally from the SPS(CERN). The energy resolution is given by

$$\sigma(E)/E = (8.1\%/\sqrt{E/GeV}) \oplus 2.1\% \tag{3.1}$$

The main contributors to the constant term are intrinsic non-uniformities, in particular tower boundaries, hot spots at fiber positions and shower depth fluctuations.

3.3 Shower Measurement

Electromagnetic(EM) showers are produced by highly relativistic electrons or photons through the two fundamental processes of Bremsstrahlung radiation

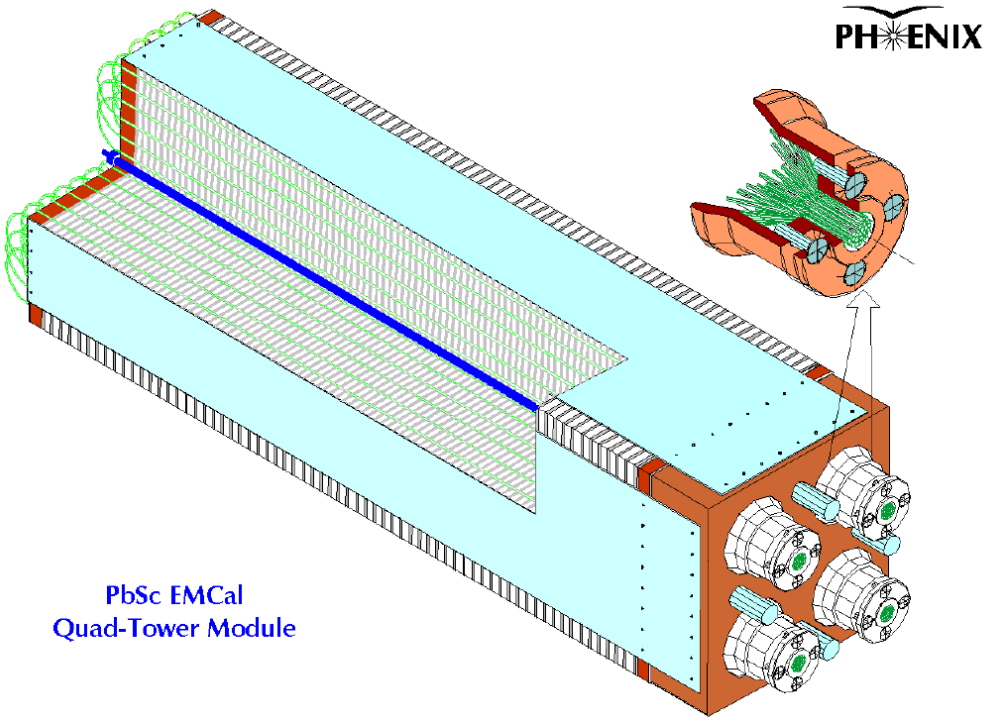

Figure 3.3: Interior view of one PbSc calorimeter module, consisting of four towers. Wavelength-shifting fibers are penetrating layers of scintillator and lead tiles and connected to PMT.

and pair production. Bremsstrahlung radiation occurs when an charge particle is accelerated and thereby must emit a photon. Pair production is the process by which a energetic photon hitting the calorimeter produces a electron-positron pair. The produced electrons and positrons subsequently lose their energy in the electric field of the atomic nuclei by radiating Bremsstrahlung. These photons can again start the process, resulting the exponential division of the original particle's energy into more and more particles which is called an EM shower. It continues until the last generation of photons no longer have sufficient energy $2m_ec^2$ to produce pairs. Except for the first step, electrons and positrons react with EMCal in the same way as photons do. The maximum depth of the shower depends on the initial energy E_0 of the incoming particle and can be expressed in terms of the radiation length X_0.

$$\frac{X_{max}}{X_0} \approx ln(\frac{E_0}{E_c}) + t \tag{3.2}$$

where $t = 0.5$ for photons and $t = -0.5$ for electrons. The critical energy E_c

is where the energy loss via ionization begins to dominate over the energy loss by Bremsstrahlung. Another EM shower property, the lateral size extension of the shower called the Moliere radius R_M is determined by multiple scattering of the shower particles and parameterized as a function of X_0 as well.

$$R_M \approx \frac{21MeV \times X_0}{E_c} \tag{3.3}$$

Hadronic showers occur when a hadron strikes a nucleus and emits out two or more high energy hadronic fragments, mostly pions. Its characteristic quantity is the nuclear interaction length λ, the distance where 63% of the hadrons suffer an inelastic interaction and form further hadrons. One third of the produced pions will generally be neutral and then they will immediately decay into two photons, which will trigger EM showering simultaneously. This is why sometimes hadronic showers will be falsely identified as EM clusters and it will contribute to one source of background for our analysis. However as a large portion of energy is lost during the undetectable hadronic processes of the collision, the total EM energy released is generally a small fraction of the energy of the original particle, whereas for an original electron or photon, they nearly deposit all of the energy. A specific group of charged hadrons are called "Minimum Ionizing Particles(MIPS)" which are charged hadrons that do not participate in an inelastic reaction and deposit only a small fraction of their energy by ionization and possibly Cherenkov radiation. It is constant over a wide energy range leading to the formation of characteristic MIP peak. Therefore, a calorimeter sometimes is designed primarily for hadron detection, such as the PHENIX ZDC and FCal.

3.3.1 Clustering Algorithm

The Molière Radius R_M in Eq. 3.3 roughly defines a lateral cone where 90% of energy of an EM shower is contained. Given the empirical formula for $E_C = 610MeV/(Z+1)$ and $X_0 \approx 2.8cm$ for PbGl($X_0 \approx 2.1cm$ for PbSc), we will have $R_M \approx 3-4cm$ for both types of calorimeters, which means it is highly possible that a shower will spread over several towers. Therefore it is essential for EMCal in PHENIX to be able to identify the cluster of towers corresponding to a single photon or electron EM shower. This process is called clustering. In this thesis, although "shower" is what nature produced(actual energy deposit from a particle) and "cluster" is what the experimentalist reconstructed(maybe erranously), the two words will be used interchangeably unless stated otherwise.

There are many clustering algorithm varying in speed and precision available. A single algorithm is used for both PbSc and PbGl in PHENIX although

there are certain desirable customization for each. Due to the high multiplicity in heavy ion collision, the algorithm must also have the capability to separate overlapping clusters. In this respect the PHENIX algorithm is optimized to separate photon showers. The shape of photon and hadronic showers in the PHENIX detector was first studied extensively using a full hit-level simulation called PISA which is based on GEANT[91]. Later shower response was verified and tuned using results from test beam studies. The clustering at PHENIX is separated into three successive procedures, finding domain of hit towers, finding peaks and shower recognition. The procedures are explained below.

Domain Finding

The energy deposited in a tower i is represented by E_i. Any tower with $E_i > 3MeV$ is defined as a hit tower and then a contiguous two dimensional group of hit towers is identified as a domain, which can have any number of towers.

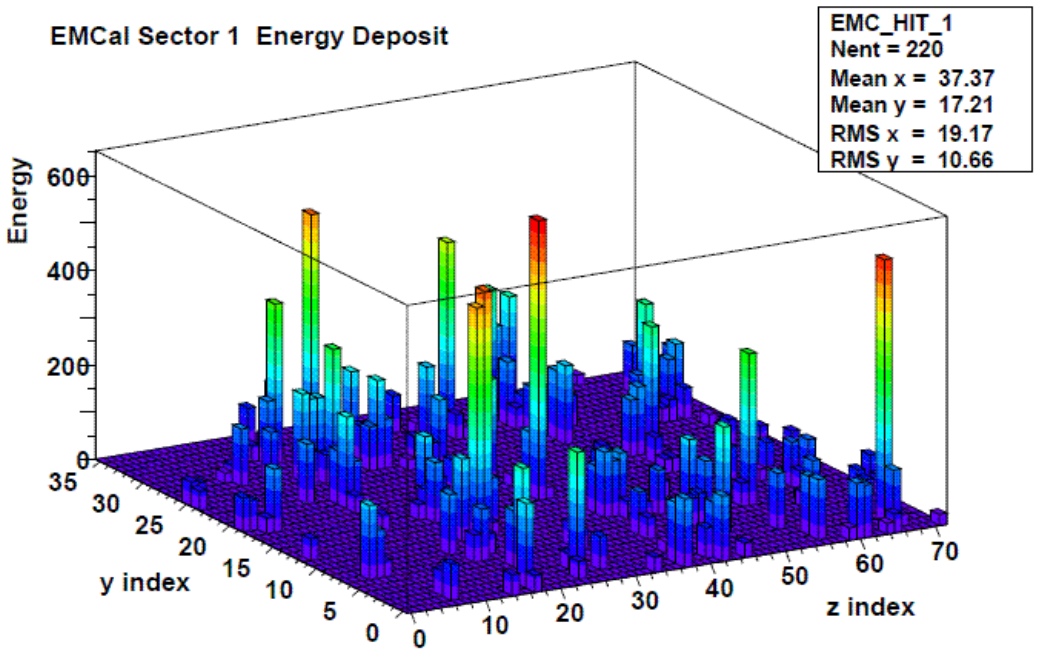

Figure 3.4: An example of energy deposit in the towers for one event.

Peak Finding

For each domain, if a tower has the highest energy of the nearest neighboring towers and the energy is more than $80MeV$, the tower is defined as a candidate of peak. For each peak candidate tower, the total energy and center of gravity of eight neighboring towers of the peak tower is calculated by energy and position of each tower. From the total energy and center of gravity position, the predicted deposited energy if the peak is generated by electromagnetic particle is calculated. The calculation is based on the test beam results.

At this stage, each tower could have contributions from multiple peaks so that the sum of those calculated contribution exceeds the measured energy deposit. Then, the fraction of energy deposited from all peaks is obtained and this energy prediction is performed iteratively. In the next step, the measured energy of each tower is shared by contributing peaks. The ratio of fractional energy of the currently evaluated peak divided by total energy deposit in the tower from all the peaks is used to calculate the total energy of the peak. Overall, six times iterations are performed then peaks are obtained. Each peak has the peak tower and associated towers. A tower could be associated to multiple peaks with fractional energy. In each peak, if the fractional energy of the tower is less than $2MeV$, it is neglected.

Shower Recognition

If a peak consists of N towers located at $(x_0, y_0), (x_1, y_1), ..., (x_{N-1}, y_{N-1})$, with their energy deposit of $E_0, E_1, ..., E_{N-1}$, where x_i and y_i are the center of tower i. The peak total energy is calculated by

$$E_{tot} = \sum_{i=0}^{N-1} E_i \tag{3.4}$$

and the center of peak is calculated by

$$(x_c, y_c) = \frac{1}{E_{tot}} \sum_{i=0}^{N-1} E_i \times (x_i, y_i) \tag{3.5}$$

In the ideal case, if the peak has no secondary contribution and has only one electromagnetic particle, the values (E_{tot}, x_c, y_c) are particle's energy and hit position. Then the shower shape parameter is calculated by

$$\chi^2 = \frac{1}{N} \sum_{i=0}^{N-1} \frac{(E_i - E_i^{pred})^2}{\sigma_i^2} \tag{3.6}$$

where N is the number of towers associated to the peak, E_i^{pred} from model is the predicted energy by assuming the peak is originated from an electromagnetic shower with energy E_{tot}, and σ_i is the variance of tower energy parameterized as a function of E_i^{pred}, E_{tot} and position(Eq.3.14). For non-zero angular incidence the center of peak does not correspond to the true impact position. The connection between the center of peak and true impact position is influenced by the finite size of the modules and the angle of the incoming particles. During the clustering process the center of peak is corrected for these dependencies based on test beam results and simulations to the actual impact point on the detector surface[92].

3.3.2 Shower Merging

When the momentum of the π^0 reaches a certain value, the decay kinematics are such that the minimum opening angle θ_{min} between the γ pair is so small that the photons will hit the calorimeter to create only a single local maximum. Since it is very important for each calorimeter to distinguish two photons resulting from the decay of a high p_T π^0, a more sophisticated cluster splitting algorithm is used to separate such photons, using a modified fit function which parameterizes well the merged photon clusters. However, for this analysis, this feature of the code was not necessary since we focus on low-to-mid p_T range. Nonetheless there is a noticeable drop in the probability of separation due to this effect in high end of p_T region shown in Fig. 3.5.

3.3.3 Shower Corrected Energy E_{core}

The E_{core} variable is the core energy of the shower under the assumption that it is electromagnetic and it is derived as follows from [93]. It was introduced to reduce shower overlap effect. If two photon showers overlap, they are most likely to do so only in their peripheries. From the test beam results, for a specific tower i included in the cluster, we can calculate distance r_i between the position of tower center (x_i, y_i) and particle hit position (x_{corr}, y_{corr}). Then the parameterized fraction of tower energy is presented by

$$F_i^p = P_1 exp\{-\frac{(r_i r_0)^3}{P_2}\} + P_3 exp\{-\frac{(r_i r_0)}{P_4}\} \tag{3.7}$$

where r_0 is the size of EMCal tower($5.54cm$) and $P_i(i = 1, 2, 3, 4)$ are parameterized to be

$$P_1 = 0.59 - (1.45 + 0.13 ln E_{tot}) sin^2\alpha, \tag{3.8}$$

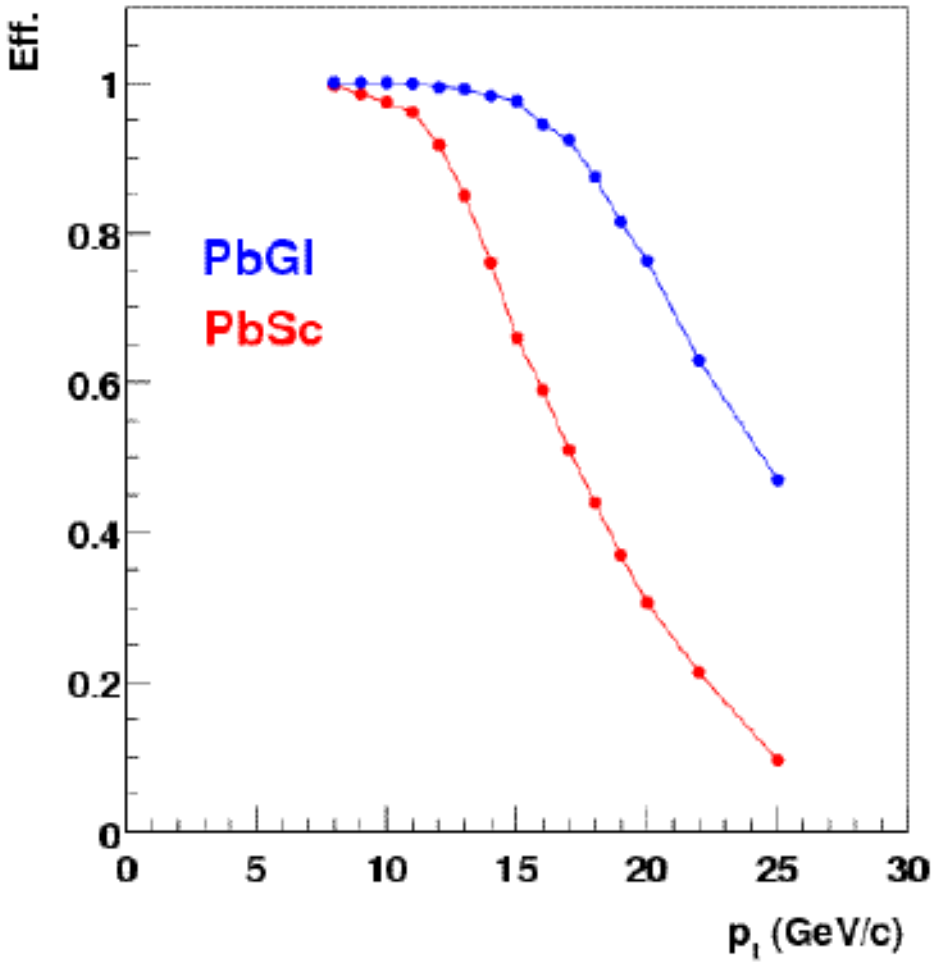

Figure 3.5: The probability that a π^0 is lost due to the merging inefficiency at high p_T[13].

$$P_2 = 0.265 + (0.80 + 0.32 ln E_{tot}) sin^2\alpha, \tag{3.9}$$

$$P_3 = 0.25 + (0.45 - 0.036 ln E_{tot}) sin^2\alpha, \tag{3.10}$$

$$P_4 = 0.42 \tag{3.11}$$

If a photon hits at the center of a tower perpendicularly as shown in Fig. 3.6, $P_1 + P_3 \simeq 84\%$ of shower energy is deposited. And other towers have less

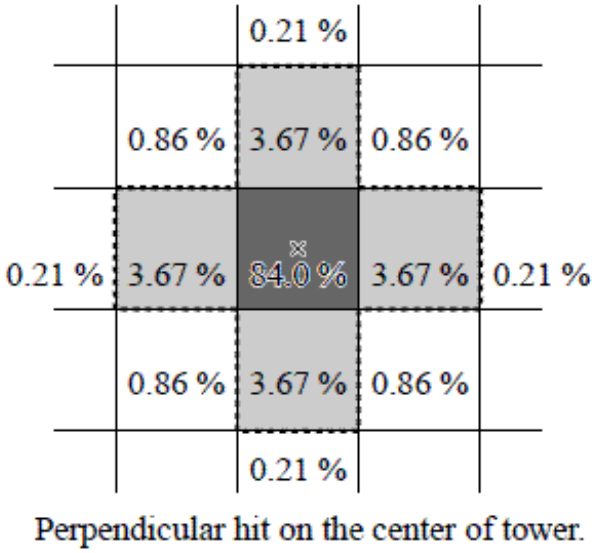

Figure 3.6: An example of predicted shower energy fraction in towers for a perpendicular hit of EM particle. Five towers surrounded by dotted line are used for E_{core} calculation. Energy deposit from the secondary contamination to the towers except for the five towers does not modify the E_{core} value.

than 4% energy. By using the predicted fractions F_i^p, the shower core energy E_{core} is defined. If the F_i^p is less than 2%, the tower is not used in core energy measurement. Then the sum of these is defined by

$$E_{core} = \sum_{for F_i^p > 0.02} E_i \tag{3.12}$$

where E_i is the "measured" energy deposit in the tower i which is used in Eq. 3.4. In the Fig. 3.6, the towers included in E_{core} calculation are towers in the region surrounded by dotted lines. E_{core} is expected to be more robust when the particle multiplicity is high. The number of towers used for E_{core} depends on the hit position and angle on the tower surface. In the Fig. 3.6, $\simeq$ 4% of shower energy is missing. The correction on the E_{core} for algorithm itself and input angle is parameterized as Eq. 3.13 based on test beam data.

$$\frac{E_{core}}{E_{core}^{corr}} = a_1 \times (1 - a_2 sin^4\theta \times (1 - a_3 \times lnE_{core})) \tag{3.13}$$

where $a_1 = 0.918$, $a_2 = 1.35$ and $a_3 = 0.003$. E_{core}^{corr} is the corrected E_{core} and will be used as E_{core} onward.

3.3.4 Shower Shape Parameter Cut

$\chi 2$ is the most commonly used variable to characterize the "photonness" of a a shower. To identify clusters produced by photons, clusters are compared to the known photon cluster shape, which is known to be the same as electron except for that the photon shower starts at a few mm ($\sim$ one radiation length) from the EMCal surface. The difference between photons and electrons causes a small difference in the energy scale ($\sim 2\%$) and the correction was performed.

For the electron, the energy deposit in several towers is known from test electron beam results and Monte Carlo simulation. To evaluate how the experimentally measured shower shape is close to the electromagnetic shower, $\chi 2$ is defined by the same function as 3.6. The variance σ_i is parametrized as the function of predicted energy E_i^{pred} in a specific tower, shower total energy and the impact angle α of the tower showed below.

$$\sigma_i^2 = \sigma_C^2 E_i^{pred}(1 + k\sqrt{E_{tot}} sin^4\alpha)(1 - \frac{E_i^{pred}}{E_{tot}}) + q_0^2 + q_1^2 E_{tot}^2 \tag{3.14}$$

where E_{tot} is the shower total energy in 3.4. The constant $\sigma_C^2 = 0.03 GeV^2$ is the scale for energy fluctuations in the shower measured from the test beam data. The factor $(1 - E_i^{pred}/E_{tot})$ introduces the correlations between energies in the towers while keeping the covariance matrix diagonal. The parametrization for energy and impact angle dependence of the errors $k\sqrt{E_{tot}} sin^4\alpha$ was chosen to fit test beam data. Also the constant coefficients q_0 and q_1 account for electronics noise. For example, for a $1GeV$ photon with perpendicular hit on the EMCal, if the hit position of the photon is the center of a tower and the predicted energy deposit on the central tower is $840MeV$ and this fluctuates with the variance $\sigma_i = 64MeV$ and $\sigma_i/E_i = 7.6\%$.

The χ^2 distribution was found to be close to the theoretical one and it is almost independent of the energy or the impact angle of the electron. Fig. 3.7 shows the χ^2 distribution from the test beam result for 2GeV/c electrons and pions[14]. The arrow marks the χ^2 cut corresponding to 90% electron efficiency and 20% for pions. The default cut to identify photons is set to $\chi^2 < 3$. This is determined based on the signal-to-noise ratio and detection efficiency.

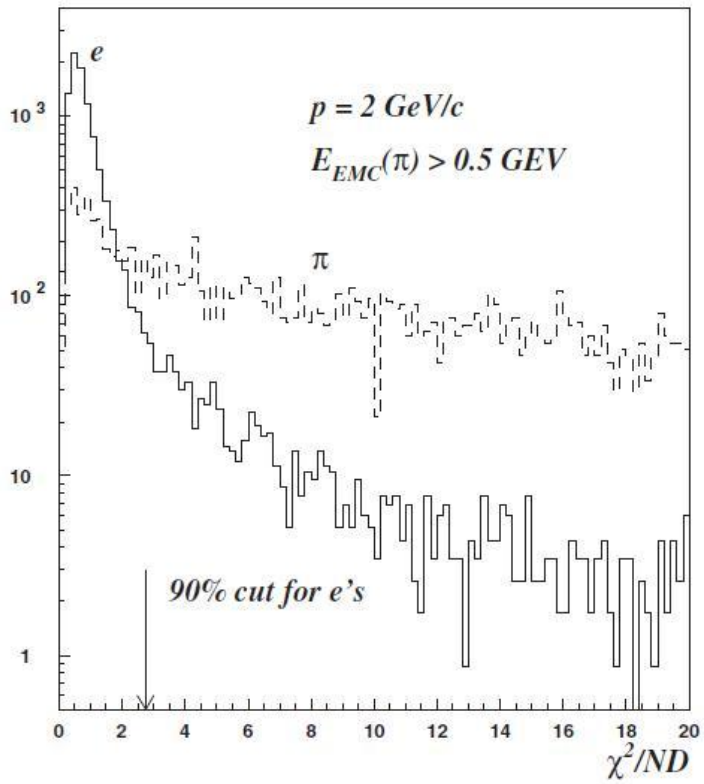

Figure 3.7: The χ^2 distribution from the test beam result for 2GeV/c electron and pion samples with energy deposit above minimum ionization[14]. The arrow marks the χ^2 cut corresponding to 90% electron efficiency.

Chapter 4

Data Analysis

In the following two chapters, we will discuss the details of direct photon analysis in Au+Au collision at $\sqrt{S_{NN}} = 200GeV$ for minimum bias based on RHIC-Year4 run in 2004. This analysis consists of at least three primary components. A new tagging method to determine the direct photon yield which leads to smaller systematic uncertainty compared to the traditional method explained in Section 4.1. The fully corrected inclusive photon spectrum with different photon PID cuts constructed from EMCal clusters is discussed in Section 4.3 and photons tagged by π^0 are extracted by using event mixing technique in Section 4.4.1. Section 4.6 presents the same calculation of inclusive photons for photons from hadronic decays using fast Monte-Carlo simulation. The analysis procedure for inclusive photon yield and double-ratio has large overlap so they are discussed in parallel but difference will be emphasized where they are present.

The double-ratio and direct photon yield will be discussed and compared to similar analysis from PHENIX Run7 and Run10 results as well as theoretical papers in Chapter 5.

4.1 Analysis and Double Ratio γ/π^0 Technique Overview

The traditional standard method of the measurement of direct photons in PHENIX is well described in [1], which is also called substraction method. The inclusive photon spectrum is measured using EMCal. Then the background photons from hadronic decays such as π^0 and η are estimated with actual measurement from PHENIX and subtracted from inclusive photon spectrum to obtain direct photon yield, which includes not only photon emitted from all the states such as initial state of the Quark-Gluon Plasma (QGP) and the final

hadron-gas state, but also from jet-fragmentation and jet-plasma interactions such as jet-bremsstrahlung and jet-photon conversion.

In order to minimize systematic effects, both inclusive photon and π^0 yield are measured then γ_{inc}/π^0 is calculated to determine if a photon excess over the expected decay background is observed. This is done by comparing the ratio of γ_{hadron}/π^0 from simulation, which only includes photons from hadronic decays, to the measured ratio γ_{inc}/π^0. The decay photon γ_{hadron} calculations are based on the measured π^0 and η spectra assuming m_T-scaling from all other radiative decays ($\eta^{'}, K^0_s, \omega$). Common systematic effects such as energy scale thus cancel during this double-ratio R_γ calculation, which then will be used to obtain direct photon yield as described below. Fig. 4.1 shows R_γ result as a function of p_T from [1] for different centralities and minimum bias.

$$R_\gamma(p_T) = \frac{(\gamma_{inc}/\pi^0)_{measured}}{(\gamma_{hadron}/\pi^0)_{simulation}} \tag{4.1}$$

$$\gamma_{direct} = \gamma_{inc} - \gamma_{hadron} = \gamma_{inc} - \frac{\gamma_{inc}}{R_\gamma} = \gamma_{inc}(1 - \frac{1}{R_\gamma}) \tag{4.2}$$

For this analysis, we adopt the same double ratio technique to benefit from the cancelation of systematic effects but are able to avoid measuring π^0 yield explicitly in order to further minimize systematic errors. At first, we obtain two types of photon samples from EMCal, one with strict PID cuts including utilizing PC3-veto to remove charged particle contamination in the clean photon sample (showed as γ_1 below in Eq. 4.3) and another with minimal photon PID cut as loose-cut photons (showed as γ_3 below in Eq. 4.4). Both spectra with their related PID cuts are explained in Section 4.3. Then by using event mixing technique described in Section 4.4.1 with these two different photon samples, we will be able to subtract background and get portion of clean photons yield from π^0 decay, which is indicated as $N^{\pi^0}_{\gamma_1}$ below.

$$N^{incl}_{\gamma_1}(p_T) = (1 - X_{hadron})\epsilon_{\gamma_1}\alpha_{\gamma_1}\gamma^{incl}_1(p_T)/(1 - p_{conv}) \tag{4.3}$$

$$N^{\pi^0}_{\gamma_1}(p_T) = \epsilon_{\gamma_3}\epsilon_{\gamma_1}\alpha_{\gamma_1} f\gamma^{\pi^0}_1(p_T)/(1 - p_{conv})^2 \tag{4.4}$$

Where ϵ_{γ_3} is loose-cut photons efficiency, which is higher and has much smaller systematic uncertainty than ϵ_{γ_1}, clean photon efficiency. α_{γ_1} is geometry acceptance for clean photon sample, which depends on active area of PC3 due to PC3-veto cut we applied. However, by calculating the ratio of these two measurements from Eq. 4.9 and 4.4, efficiency and acceptance for clean photons are canceled out completely as shown below. Only correction factors left are hadronic contamination X_{hadron}, photon loss from conversion p_{conv},

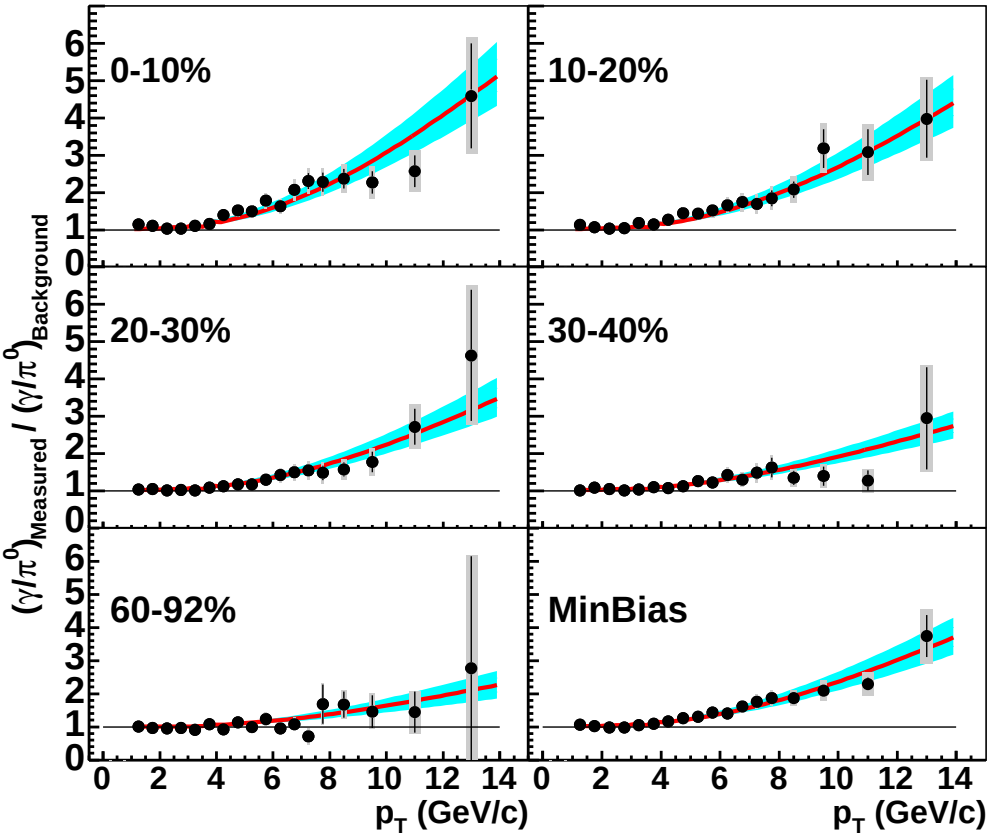

Figure 4.1: Double ratio of measured $(\gamma/\pi^0)_{measured}$ invariant yield ratio to the background decay $(\gamma/\pi^0)_{background}$ ratio as a function of p_T for minimum bias and for five centralities of Au+Au collisions at $\sqrt{S_{NN}} = 200GeV$(0-10% is the most central). Statistical and total errors are indicated separately on each data point by the vertical bar and shaded region, respectively. The solid curves are the ratio of pQCD predictions scaled by the number of binary nucleon collisions. The shaded region around the curves indicate the variation of the pQCD calculation for scale changes from $p_T/2$ to $2p_T$, plus the $< N_{coll} >$ uncertainty [1].

loose-cut photon efficiency ϵ_{γ_3} and factor f, which is conditional probability of having a loose-cut photon in the acceptance given that clean photon from the same π^0 is already in the acceptance. Details on how to estimate these correction factors as well as their systematic errors are laid out in Section 4.5 and 4.7.

$$R_{measured}(p_T) = \frac{N_{\gamma_1}^{incl}(p_T)}{N_{\gamma_1}^{\pi^0}(p_T)} = \frac{(1 - X_{hadron})(1 - p_{conv})}{\epsilon_{\gamma_3} f}(\gamma_1^{incl}/\gamma_1^{\pi^0}) \quad (4.5)$$

Then we can calculate the same ratio for photons only from hadronic decays through Monte-Carlo simulation, which is explained in Section 4.6.

$$R_{MC}(p_T) = \frac{N_{\gamma_1}^{hadron}(p_T)}{N_{\gamma_1}^{\pi^0}(p_T)} = \gamma_1^{hadron}(p_T)/\gamma_1^{\pi^0}(p_T) \quad (4.6)$$

By using the same double ratio technique in Eq. 4.1, the yield of inclusive clean photons over photons from hadronic decays can be calculated as follows

$$R_{\gamma_1}(p_T) = \frac{N_{\gamma_1}^{incl}(p_T)}{N_{\gamma_1}^{hadron}(p_T)} = \frac{R_{measure}(p_T)}{R_{MC}(p_T)} = (1-X_{hadron})(1-p_{conv})\frac{(\gamma_1/\gamma_1^{\pi^0})}{(\gamma_1^{hadron}/(\epsilon_3 f)\gamma_1^{\pi^0})} \quad (4.7)$$

4.2 Events Selection

This analysis is based on the data set collected during the RHIC-Year4 run(Jan. 1st, 2004-May 14th, 2004), the Au+Au at $\sqrt{s_{NN}} = 200GeV$ collisions. Appendix A summarizes run numbers which are used for this analysis. The run selection assumes uniform detector configuration and minimizes run-to-run variations. We exclude bad runs with the following criteria.

- Runs with nonuniform centrality distribution are excluded. While the ϕ angle for the centrality determination is fixed by the stable runs, the centrality distributions of some runs are not flat and could have some bumps. The left plot of Fig. 4.2 shows a typical centrality distribution. For each run, centrality distributions are fitted with the first order polynomial and each χ^2/NDF is evaluated as the flatness of centrality distribution as shown in the right plot of Fig. 4.2. About 5% of total number of events are excluded due to the bad flatness where $\chi^2/NDF > 3$.

- Runs with non-flat reaction plane distribution are excluded, which is also evaluated by fitting.

- Runs where EMCal can not properly measure energy of electromagnetic clusters are excluded. The stability of energy linearity and resolution of EMCal is evaluated based on π^0 peak position and MIP peak position. Most runs pass this criteria.

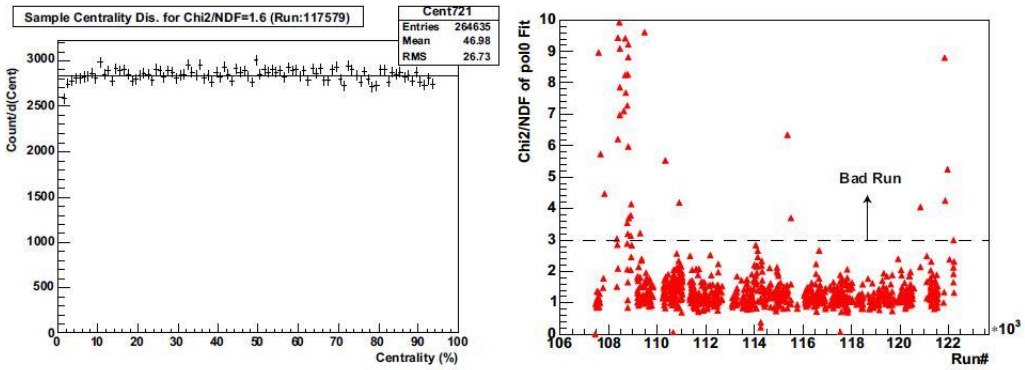

Figure 4.2: Centrality distribution measured by BBC and ZDC correlation. Left: Typical centrality distribution. Right: χ^2/NDF of fitted first order polynomial to centrality distribution as a function of run numbers. Runs with $\chi^2/NDF > 3$ are not used for this analysis

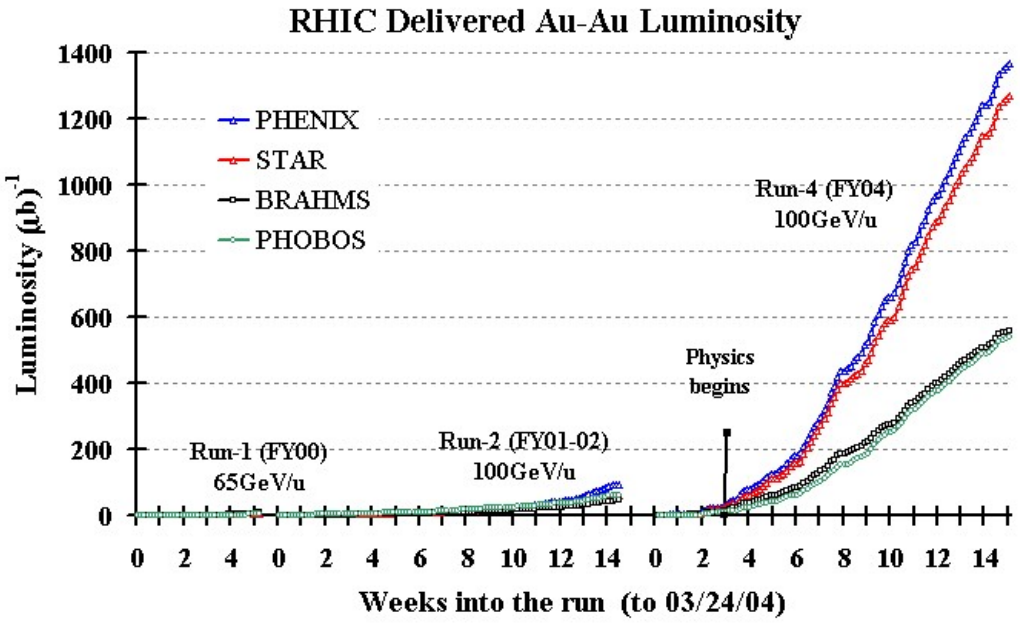

Figure 4.3: The integrated luminosity in Year-4 Au+Au run at PHENIX $\sqrt{s_{NN}} = 200GeV$ compared to previous runs and three other detectors as a function of elapsed weeks, which indicates the data of $3.6\mu b^{-1}$ is recorded by PHENIX everyday on average.

4.2.1 Minimum Bias Trigger Definition

The data were taken with the "Minimum Bias" trigger, which is defined as $BBCNS \geq 2 \cap ZDCNS \cap (\mid z_{bbc} \mid < 38cm)$. $BBCNS \geq 2$ means that at least 2 hits are required in both the north and south BBC. ZDCNS requires that both the north and south ZDC have at least one neutron hit. z_{bbc} is z-vertex obtained by the BBC Level-l(BBCLL1) trigger online. This trigger accepts $\simeq 92\%$ of the geometrical cross section for Au+Au collisions.

4.2.2 Centrality Definition

The events selected by the minimum bias trigger described above are classified according to the centrality, which is determined via the correlation between the energy deposit in the ZDC and the charge deposit in the BBC. The BBC measures the multiplicity of charged particles in rapidity region of $3.1 < |\eta| < 3.9$ while the ZDC measures spectator neutrons close to the beam axis. Both of them are sensitive to the impact parameter of Au+Au collisions. This behavior is illustrated in Fig. 4.4 for the complete minimum bias sample. The distribution is divided into the different centralities by an angle ϕ_{cent} in the BBC-ZDC plane defined as the following:

$$\phi_{cent} = arctan(\frac{(Q_{BBC} - Q_0)/Q_{max}}{E_{ZDC}/E_{max}}) \tag{4.8}$$

where E_{max} is the maximum energy deposited in the ZDC and Q_{max} is the maximum charge-equivalent measured by BBC. The value of Q_0 as well as choice of angular cuts shown in Fig. 4.4 is based on a simulation of BBC and ZDC signal together with the Glauber model of the Au+Au collisions as described in [94]. The cut is chosen in a way that the selected event sample represents a specified fraction of the total geometrical cross section σ_{tot} so distribution of ϕ_{cent} is flat.

4.3 Inclusive Photon

As described in Section 4.1, two different photon spectra are required for this analysis where loose-cut photons γ_3 is a superset of the clean photons γ_1. Different PID cuts are applied to obtain these photon samples as discussed in this section.

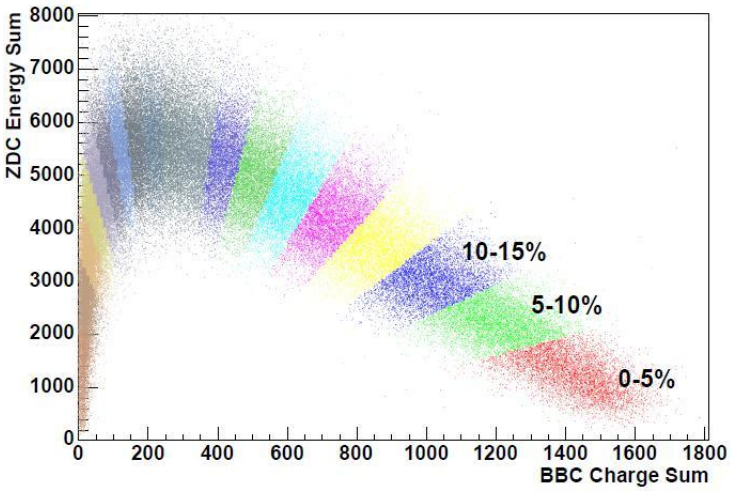

Figure 4.4: Total ZDC signal versus total charge measured by BBC and the division into different centralities based on this distribution.

4.3.1 Loose-cut Photons from EMCal

Cuts based upon shower-shape are commonly used in calorimeters to distinguish between showers produced by photons/electrons and hadrons, because the pattern of energy deposit is quite different. In PHENIX the default cut(used in most analysis) to identify photons is $\chi^2 < 3$. The χ^2 compares the known electromagnetic shower-shape at a given energy, impact point and angle to the observed pattern of energy deposit within a cluster. On top of χ^2 cut, a minimal transverse momentum cut of $p_T < 0.2GeV/c$ is also applied to obtain loose-cut photon spectrum.

$$\frac{d^2N_\gamma}{dp_T dy} = \frac{1}{2\pi N_{evt}} \frac{(1-X_{n\bar{n}})(1-X_{ch})}{\epsilon_\gamma \alpha_\gamma (1-p_c)} \frac{dN_{cluster}}{\delta p_T \delta y} \tag{4.9}$$

With the same set of correction factors such as efficiency and acceptance in Eq. 4.3, X_{hadron} in Eq. 4.5 is further broken down to two terms with X_{ch} denoting the fraction of charged particles in the cluster spectrum and $X_{n\bar{n}}$ being the fraction of neutrons and anti-neutrons in the neutral cluster spectrum (other neutral hadrons will not reach the EMCal since their life times are too short) because some of these particles are not removed by PID cuts. The fully corrected Lorentz invariant yield per event for minimum bias collisions can be calculated by scaling down $\frac{1}{2\pi p_T N_{evt}}$ where N_{evt} is the number of analyzed collision events. Finally the yield is normalized per unit transverse momentum δp_T and rapidity δy. The raw spectrum without these correction of loose-cut photons is shown in Fig. 4.5. All the correction factors are determined in

Section 4.5 and the fully-corrected inclusive photon spectrum with systematic errors is shown in Section 5.2.

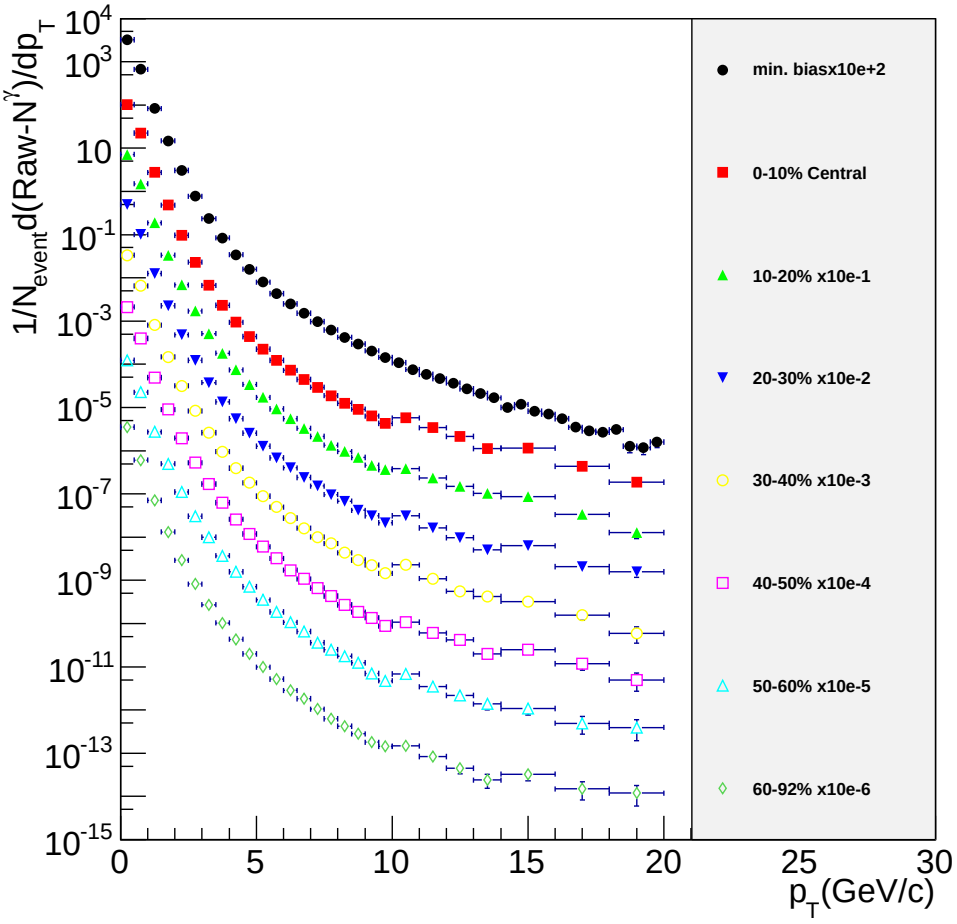

Figure 4.5: Raw cluster energy spectrum after χ^2 cut in PbSc.

4.3.2 Clean Photons from EMCal

The following PID cuts are applied to get the clean photons sample for this analysis. Since a large source of background for the inclusive photon measurement, especially at low p_T, is from charged particles, the most straightforward idea of removing them would be to use the pad chamber PC3 located right in

front of EMCal, as a veto detector and simply remove all EMCal hits connected to a PC3 hit within a certain radius.

- $p_T > 200 MeV/c$
- $\chi^2 < 3.0$
- EMCal deadmap and warnmap 0x1ce70
- $tof_{corr} < 1.35 ns$
- $pc3dz < 10.0 cm$
- $pc3dphi < 0.02 rad$
- $PC3deadmap$

Since the intrinsic efficiency of PC3 is close to be 100%[95], the veto-efficiency of PC3 is mostly determined by the active area. In order to overcome this artifact, a PC3 deadmap is developed. First, the acceptance of PC3 is projected onto EMCal by EMCal tower size. Then all the EMCal hits satisfied much tighter PC3-veto cuts of $pc3dz < 2cm$ and $pc3dphi < 0.001$ are filled into a so-called PC3 veto map. Areas with significantly less PC3 hits are defined as PC3 deadmap showed in Fig. B.2. Such areas are attributed either to the structure of PC3 or to problems in PC3 pads. Additionally false PC3 rejection can caused by low momentum electrons and the rate of this false rejection is estimated $\simeq 1.2\%$ [96] by the probability to have a very low energy secondary ($< 2MeV$) for photons.

As a excellent cross-check, the stochastic cuts from [97] are also used to obtain a clean photon sample instead of PC3-veto cuts. The basic idea behind stochastic cuts is to characterize the shower-shape with more than one quantity, e.g. the χ^2, the ratio of energy deposit in the central tower and the total cluster energy and the ellipticity of the shower. Whereas these quantities are not independent of each other, they are not perfectly correlated either and each of them will highlight a somewhat different aspect of the shower. A small χ^2 value is already an indication that the shower is a photon, but if in addition most of its energy is in the center, this is an even stronger indication.

Threshold for different stochastic cuts is determined from simulation similar to a likelihood-function. At first, based upon simulation, the efficiency vs the actual value of the cut is established where efficiency is defined as ratio between number of photons passing the cut and number of non-photons passing the same cut. Next each efficiency is fitted by a function of cut value up to its highest value plateau, then weighted with the fraction of photons that survive

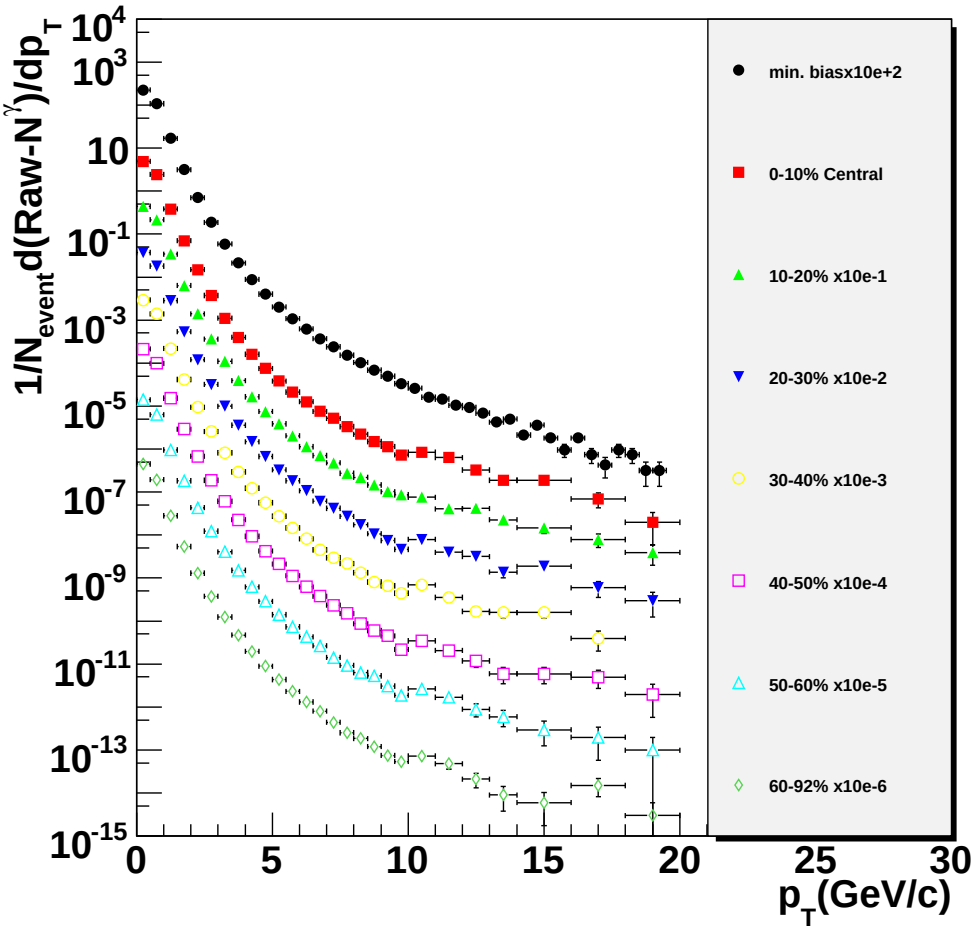

Figure 4.6: Raw cluster energy spectrum after PC3Veto+TOF cut in PbSc.

the cut when it reaches its plateau. This way the overall photon efficiency still remains relatively high while maximizing the cleanness of the sample.

$$Cut2 : (0.3 + 4 \times exp(-ecore/ecent) \times (1.9 - 0.67\chi^2) > 1.4 \qquad (4.10)$$

In this analysis, the following Stochastic Cut2 in Eq. 4.10 is used where ecent is the energy in the central tower and ecore is total cluster energy. The effect of this cut is illustrated in Fig. 4.7 and Fig. 4.8. In Fig. 4.7, the horizontal scale stands for deposited energy, not only for photons, but also

for hadrons that we want to reject. As thick curves indicates, stochastic cut2 gives a much cleaner sample at the expense of lower electron efficiency, which stabilizes above 1GeV with little variation. Fig. 4.8 shows the distribution of stochastic cut2 value for EMCal clusters from photons, neutrons/antineutrons and charged particles in Hijing simulation. Both uncorrected raw photon spectra from pc3-veto cuts and stochastic cut2 are shown in Fig. 4.6 and Fig.4.9.

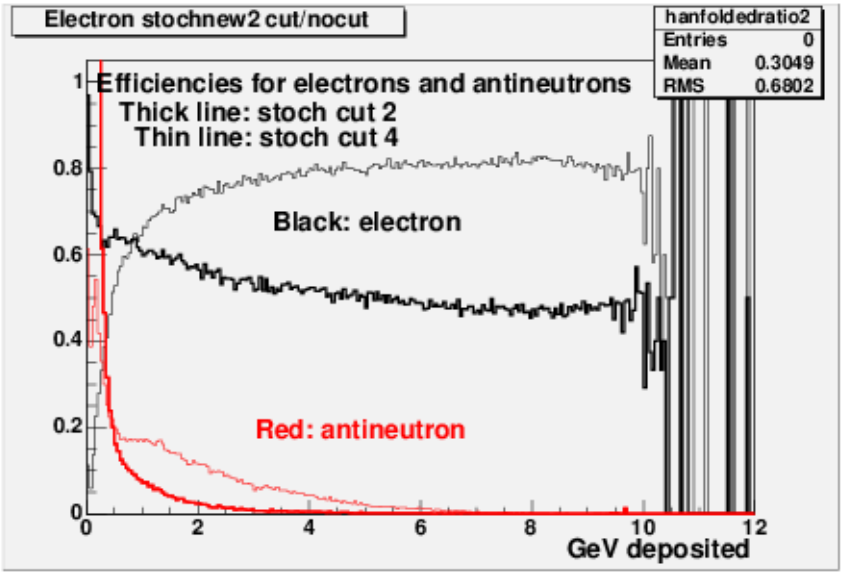

Figure 4.7: Simulated efficiencies of two stchastic cuts for electrons and antineutrons as a function of deposited energy. For $\bar{n}$ the measured p_T spectrum is folded with the distributions of deposited energy as a function of p_T. Thick lines are for stochastic cut2. Black curves are efficiencies for electrons and red for antineutrons. Above $6GeV$ antineutrons are suppressed by more than a factor of 1000.

4.3.3 Bin-Shift Correction

Particles yield spectrum such as γ, π^0 and η produced in heavy-ion collisions are roughly following a falling exponential at low p_T and power law distribution at high p_T, both of which fall steeply towards high transverse momenta. Therefore, the value of particle yield (or cross section) in the center of each finite-size p_T bin does not represent the true value without applying a further correction. This correction either moves bin-center towards lower-p_T while the

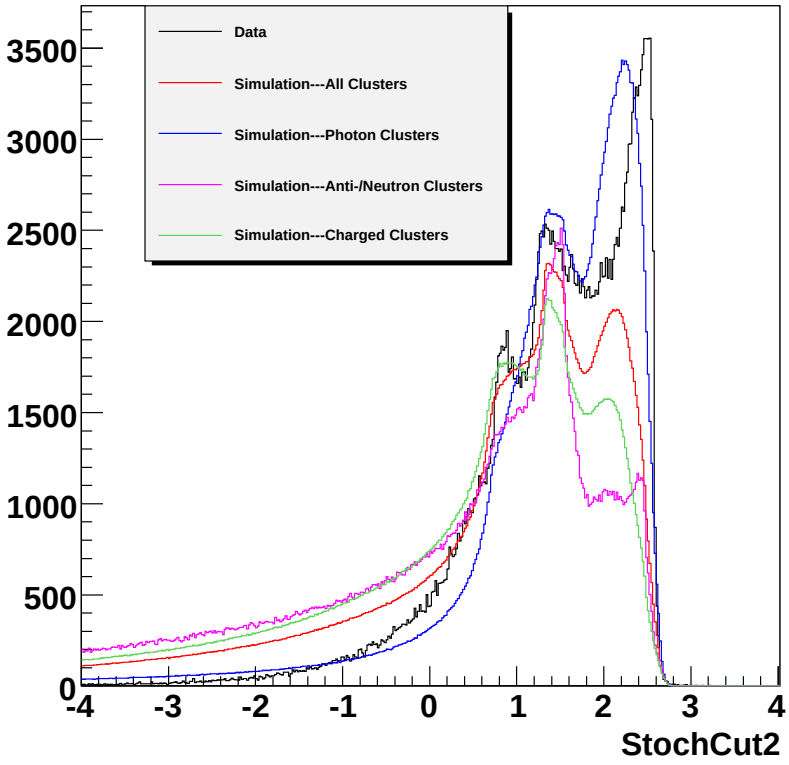

Figure 4.8: Distribution comparison of Stochastic Cut2 for EMCal clusters between data and Hijing simulation. The difference between photons, neutron/antineutron and charged particles clusters has been also shown for Hijing simulation.

data points keep their position in y direction or moves the data points vertically to the lower true yield while keeping the same bin-center as p_T value. In this analysis, the second method is used which makes it consistent with other data such as η/π^0 ratio used later and easier to compare with PHENIX published result.

In order to calculate this correction, in principle the true shape of the spectrum has to be known. Since this is to be measured, an iterative procedure is applied to correct for the bin-shift by using a simulated photon spectrum from hadronic sources such as π^0 and η, which is described as cocktail in Section 4.6. With the help of cocktail, photon spectrum $f(p_T)$ from hadronic decay is generated by fast Monte Carlo simulation. Then the true value of the yield in the center of a given p_T bin is calculated by being scaled down by

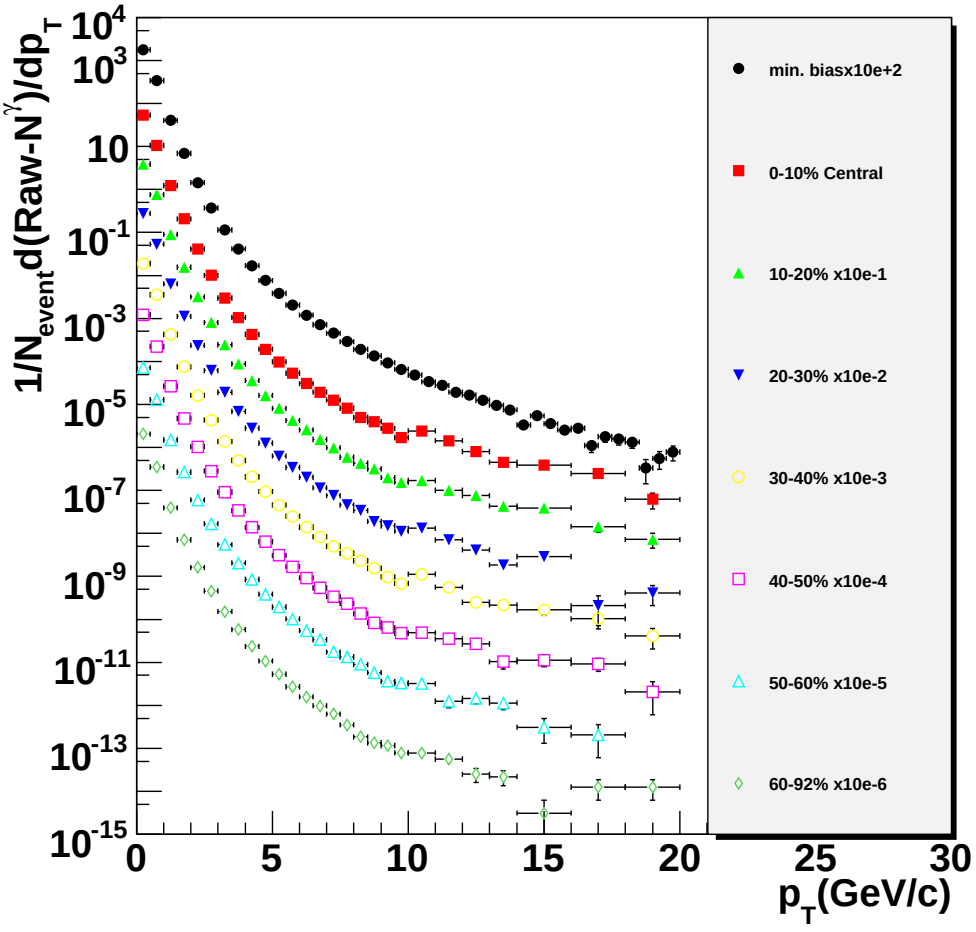

Figure 4.9: Raw cluster energy spectrum after Stochastic Cut2 in PbSc.

the following factor, where p_T^c is the bin center and δ is the bin width from measurement.

$$R_{binshift} = \frac{1/\delta \int_{p_T^c-\delta/2}^{p_T^c+\delta/2} \gamma_{\text{cocktail}}(p_T), \mathrm{d}p_T}{\gamma_{cocktail}(p_T^c)} \tag{4.11}$$

4.4 π^0 Tagged Photon Yield Extraction

By pairing loose-cut photons sample and clean photons sample (by either PC3-veto or Stochastic cut2) from EMCal and calculating their invariant mass,

clean photons originating from π^0 decay can be obtained if photon pair's invariant mass falls into π^0 mass window.

4.4.1 Event Mixing

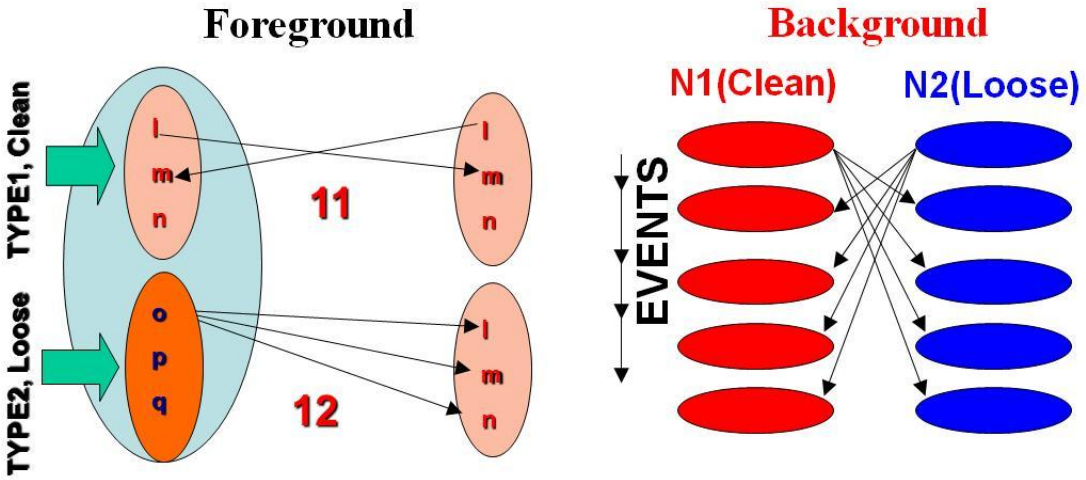

Figure 4.10: Event mixing schema for foreground from the same collision and background from different events.

As illustrated in Fig. 4.10, since the loose-cut photons γ_3 are always superset of the clean photons γ_1, in order to make event mixing and pair counting straightforward, a complementary set of photon sample γ_2 is created as $\gamma_3 - \gamma_1$. And invariant mass of all possible unique pairs of $\gamma_1\gamma_1(FG11)$ and $\gamma_1\gamma_2(FG12)$ is calculated and added together as final foreground signal FG13.

$$\begin{aligned} N_{FG11} &= N(\gamma_1) \times (N(\gamma_1) - 1)/2 \\ N_{FG12} &= N(\gamma_1) \times N(\gamma_2) \\ N_{FG13} &= N_{FG11} + N_{FG12} \end{aligned} \tag{4.12}$$

The same method is applied by pairing photons from different events ($i \neq j$) to get the background shape shown in Eq. 4.13 below, where i and j are event number. In practice, a fixed-length FIFO (first-in-first-out) queue structure is maintained to hold most recent events γ_1 and γ_2 information, which is used for mixing of current collision event assuming photons across events are not correlated.

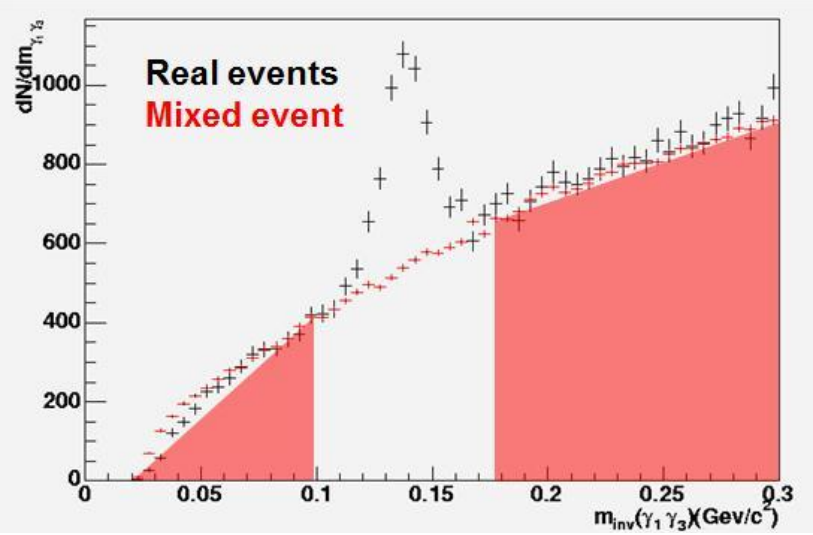

Figure 4.11: Pairs between loose-cut photons and clean photons from the same events form black points as foreground and the same pairs from different events form red points as combinatorial background.

$$
\begin{aligned}
N_{BG11} &= 2 \times N(\gamma_1)(i) \times N(\gamma_1)(j) \\
N_{BG12} &= N(\gamma_1)(i) \times N(\gamma_2)(j) + N(\gamma_2)(i) \times N(\gamma_1)(j) \\
N_{BG13} &= N_{BG11} + N_{BG12}
\end{aligned}
\tag{4.13}
$$

4.4.2 Peak Extraction

Fig. 4.11 shows an example of invariant mass distributions of $\gamma_1\gamma_3$ pairs for $p_T(\gamma_1)$ (not p_T of $\gamma_1\gamma_3$ pair) between $5.0GeV/c$ and $5.5GeV/c$ for minimum bias Au+Au collision. The background under the clear π^0 mass peak is mostly from combinatorial mixing of photons from different decaying π^0 or from pairs containing non-photon clusters that nonetheless pass the cuts for photon identification.

The mixed event histograms are normalized to the corresponding real photon pair invariant mass distribution below and about the π^0 peak. It is then subtracted from the real distribution to produce the true π^0 invariant mass peak which is shown in Fig. 4.12, which is fitted with a Gaussian plus a second-order polynomial function to remove residual underneath the peak. The yield is determined by counting the number of entries in the histogram for the window of 3σ around mean after the background subtraction then scaling up the full Gaussian distribution. The completed sets of plots showing peak extrac-

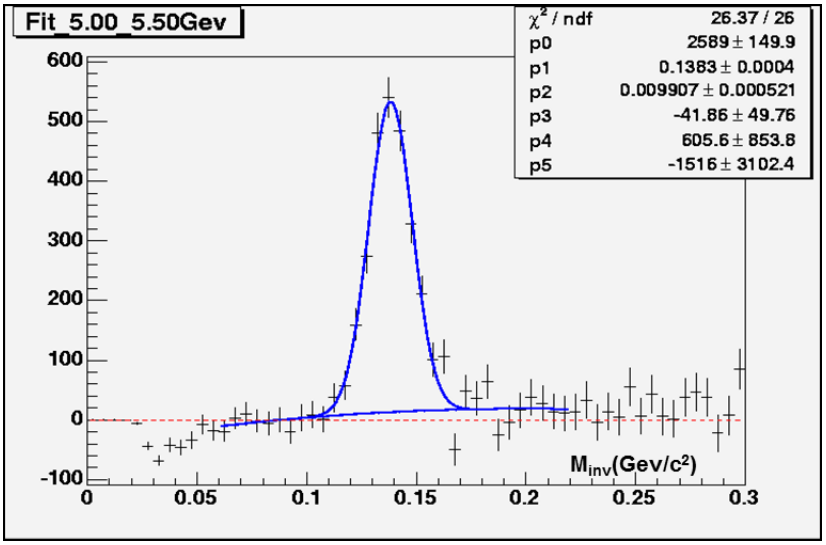

Figure 4.12: π^0 peak after subtraction of normalized background from foreground. The fit result of a Gaussian plus a second-order polynomial function is plotted in blue.

tion for both PC3-veto and Stochastic Cut2 dataset are listed in Chapter C and D up to p_T of $8.0 GeV/c$.

To simply integrate the background-subtracted distribution rather than calculate the yield from a Gaussian fit of the π^0-peak has several advantages. The integration facilitates to determine the yield even when the statistics becomes so low that a Gaussian fit might no longer be trusted. Also, in contrast to a fit, the integral method is insensitive to the details of the peak shape and therefore is not affected by non-Gaussian tails of the π^0-peak which might result from overlap effects, which must be accurately reproduced when using a fit method.

4.5 Correction Factors

As shown in Eq. 4.7 and Eq. 4.9, various correction factors such as photon detection efficiency and acceptance are required in order to get direct photon excessive yield ratio R_{γ_1} and fully corrected inclusive photon spectrum.

4.5.1 Single Photon Efficiency from Embedding

Photon detection efficiency describes the response of EMCal to photons that hit its surface. It is influenced by the position and energy resolution of EMCal

as well as by the event multiplicity which determines the probabilities for EMCal clusters to overlap. Furthermore, the efficiency depends on various photon PID cuts. Since both photon detection efficiency and acceptance correction for clean photon sample are canceled in double ratio, we only need to determine these values for loose-cut photons which will minimize the systematic error brought into double ratio shown in Eq. 4.1. The efficiency correction can be generally defined as function of transverse momentum.

$$\epsilon(p_T) = \frac{f(p_T)_{output}}{f(p_T)_{input}} \tag{4.14}$$

The input spectrum $f(p_T)_{input}$ for the efficiency determination is in principle unknown but the issue is circumvented by assuming a spectrum for the first pass which is usually based on the measured raw spectrum. This spectrum is used to determine the efficiency for the first correction of raw spectrum, resulting in a new input distribution. Iterative repetition of this procedure leads to a quick convergence of the calculation.

Due to the limited energy resolution of EMCal and steeply falling input photon spectrum, the photon yield feed-down from higher p_T is smaller than from lower p_T . This leads to an overall shift of the yield toward higher transverse momenta and an efficiency larger than one. In addition, in central collisions the electromagnetic showers from different particles are likely to overlap which can either form one single cluster with an energy not connected to one single incident particle or cause cluster breakup. This so-called shower overlap leads to a further smearing of energy measured with EMCal. As the simulation of a sufficient number of full events would need too much CPU time, the shower overlap is modeled by embedding simulated particles into real events, which gives a realistic description of EMCal occupancy in the events as a real occupancy is used.

To simulate the PHENIX detector response for the input particles, GEANT 3.21 is mainly used. Each subsystems of PHENIX spectrometer are located in the simulation virtually and the GEANT output is corrected with the parameterizations obtained by test beam result. The output data from simulated single π^0 and γ samples are then embedded into real Au+Au events. The simulated deposited energy in EMCal tower is merged with real data and clusters are reconstructed through clustering algorithm. The embedded photons are accumulated for each cluster multiplicity and weighted by the multiplicity of clusters which hit EMCal.

Reconstructing the properties of these embedded particles allows a detailed study of how the measured spectrum is influenced by the detector and high-multiplicity environment. The main advantage of this technique is that the

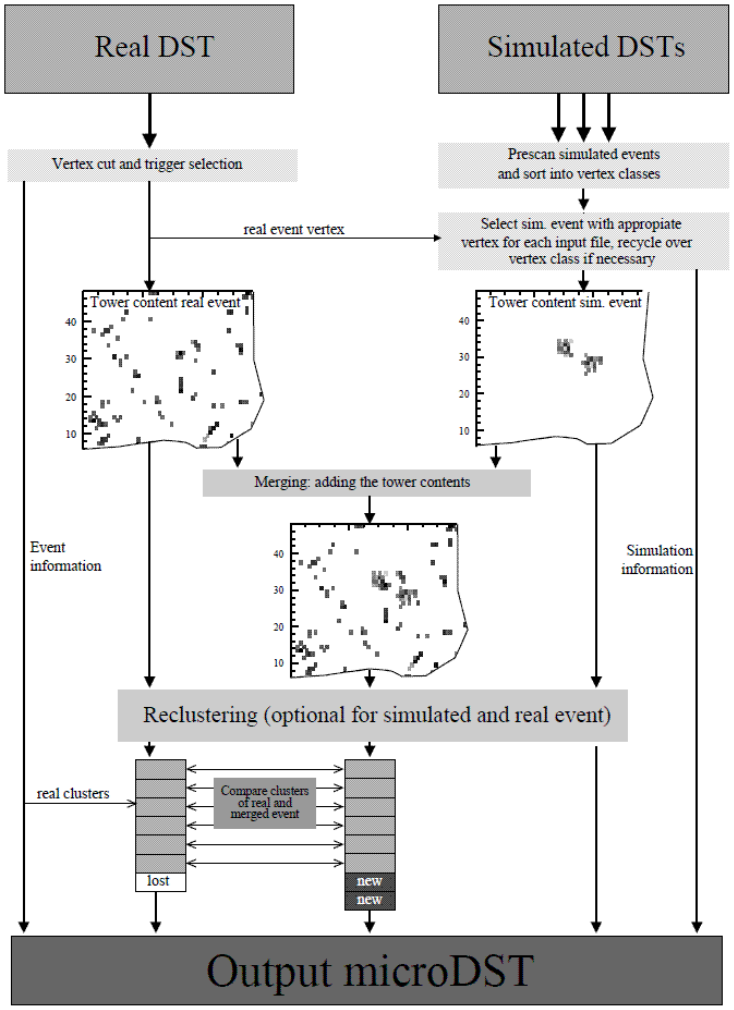

Figure 4.13: Main program flow of the embedding algorithm for EMCal clusters.

merged event can be processed within the same clustering algorithm discussed in Section 3.3.1 and analyzed within the same framework as the real data. Furthermore, the combination with the real events provides measured behavior of EMCal in a high multiplicity environment which no simulation can accomplish so accurately.

The photon identification efficiency ϵ is calculated from embedding studies as ratio between the energy spectrum after and before a cut is applied as function of the true p_T of the embedded real photons where the clustering efficiency is assumed to be 100%. There is always at least one cluster found

for photons above $1 - 2GeV/c$ so the assumption is reasonable for the energy range of interest for this analysis. Efficiency for the loose-cut photons is showed in Fig. 4.14.

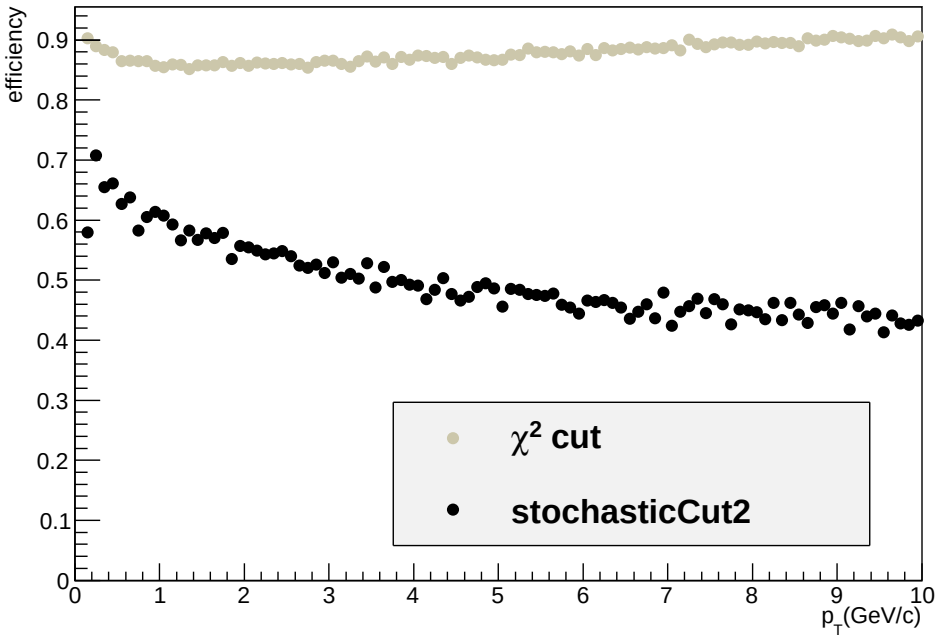

Figure 4.14: EMCal detection efficiency in Au+Au collision for photon for two different PID cuts in PbSc.

4.5.2 Single Photon Acceptance

Due to the limited geometrical coverage of EMCal, the acceptance correction has to be taken into account in order to get photon yield in full azimuth and rapidity space. For example, clusters on towers at the edges of sectors are not used in this analysis because part of energy is likely to leak outside EMCal in such case. EMCal bad towers, which contain wrong or suspicious energy information, are also excluded together with their neighbors.

The acceptance correction is calculated with fast Monte-Carlo simulation. Neutral particles like photon have straight line trajectories as opposed to charged particles which are bent by the magnetic field. Therefore the correction simply corresponds to the fraction over the whole azimuth and rapidity interval. It is constant with p_T as shown in Fig. 4.15. The main challenge in the acceptance calculation is to implement bad EMCal module map for

PbSc. Fortunately only one set of bad module map is used for PbSc during the entire run period hence uncertainty caused by run-to-run dependency is minimized. The acceptance correction can be also calculated in embedding studies discussed in Section 4.5.1 in which the acceptance will drop slightly at very high p_T because it is more likely that large showers caused by high p_T photons will overlap with bad tower and edge of EMCal hence get rejected by clustering algorithm.

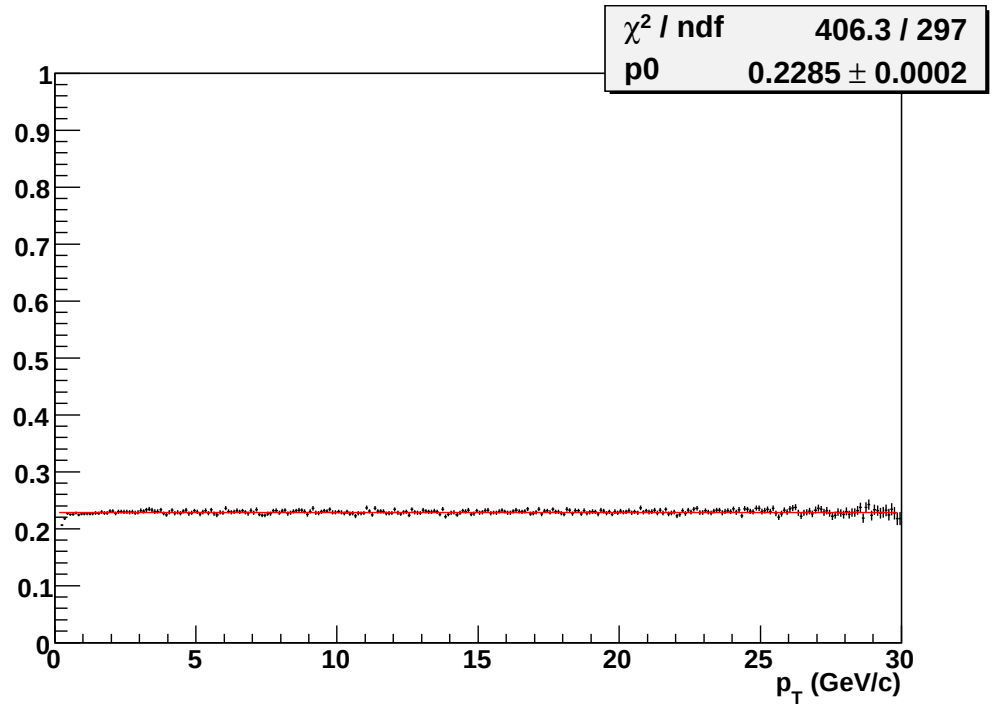

Figure 4.15: Single photon acceptance in PbSc. The red line is the fit by constant.

However, for π^0, we can only capture it when both of its decay photons are within EMCal coverage. Since the opening angle of decay photons depends on the Lorentz boost of π^0, the distribution depends on p_T. As π^0 p_T goes higher, it will approach single photon acceptance. In this analysis, the acceptance correction for π^0 is not explicitly calculated but it is included in conditional acceptance f as shown in Eq. 4.1, which will be discussed in Section 4.6.

4.5.3 Background from Charged Particles

For inclusive photon measurement, a large amount of background comes from charged particles especially at low p_T. Charged hadrons deposit on average only a fraction of their energy in the EMCal and dominate the charged particle background at low energies or transverse momenta. At higher p_T, charged particle background is dominated by photon conversions.

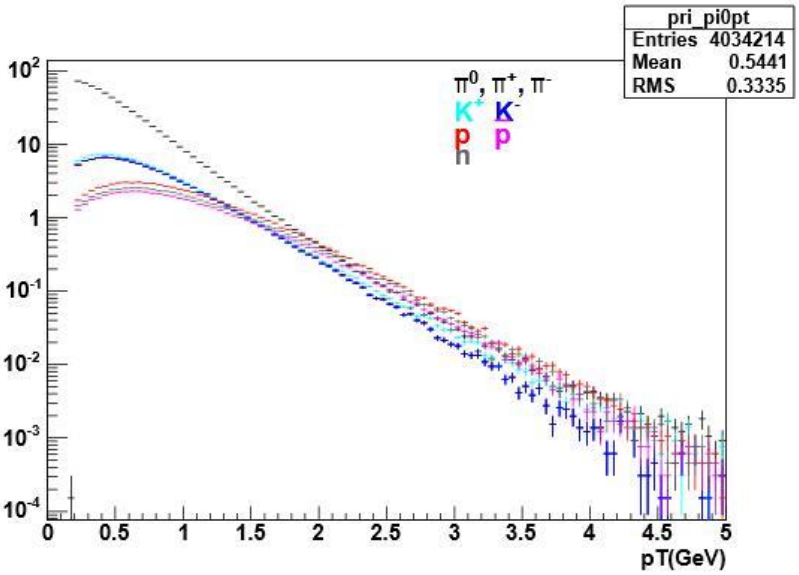

Figure 4.16: Simulated $\pi^{\pm,0}, K^{\pm}, \bar{p}, p, \bar{n}, n$ distribution by PHENIX Event Generator. The unit is $\frac{dN}{dydp_T}$.

The fraction of remaining hadron hits to all hits that satisfy the PID cuts are estimated with a full PISA(the PHENIX Experiment Simulation Package) simulation [93] where input particles are generated with an event generator based on actual PHENIX measurement of $\pi^0, \pi, K^{\pm}$ and $p\bar{p}$ spectra shown in Fig 4.16. The hadron rejection obtained with different PID cuts is shown in Fig. 4.17, for the loosest cut (χ^2 cut) and the tighter one (StochasticCut2). The results depend on how well hadrons are described by the simulation, both their overall energy deposit and the shape of hadron showers which PID cuts rely on. While the hadron contribution levels off at a small constant value above $p_T = 3GeV/c$, the hadron contribution remains as a major source of systematic uncertainty at low-p_T due to imperfect agreement especially for $p\bar{p}$ [93]. The value of this constant extrapolation is determined by a fit to

$1 - X_{hadron}$ distribution and then used in this analysis to avoid fluctuations of correction caused by lack of statistics in PISA simulation.

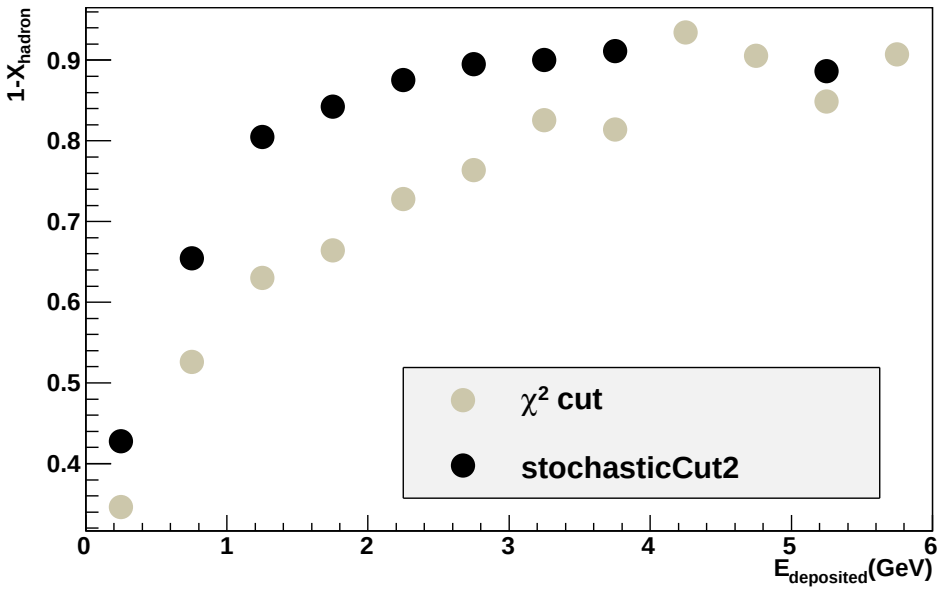

Figure 4.17: Charged particles correction factor $(1 - X_{hadron})$ after PID cuts in minimum bias events for PbSc.

4.5.4 Background from Neutrons and Antineutrons

Neutrons and antineutrons spectrum is estimated by a parametrization of identified proton and antiproton spectrum measured in AuAu collision at PHENIX for different centrality selections [98]. The basic assumption is that the production of nucleons does not depend on the isospin. Hence the number of antineutrons and neutrons produced in the collision, not originated from nuclei, is equal to the number of newly produced antiprotons and protons. It is also assumed that the production of nucleons and antinucleons is equivalent. The yields are then given by:

$$\frac{d^2N}{dp_T dy}\mid_n = \frac{d^2N}{dp_T dy}\mid_{\bar{p}} + (\frac{d^2N}{dp_T dy}\mid_p - \frac{d^2N}{dp_T dy}\mid_{\bar{p}})\frac{A-Z}{Z} \tag{4.15}$$

$$\frac{d^2N}{dp_T dy}\mid_{\bar{n}} = \frac{d^2N}{dp_T dy}\mid_{\bar{p}} \tag{4.16}$$

where A and Z are the mass number and atomic number respectively. The second term in Eq. 4.15 is the contribution of neutrons from the nucleus.

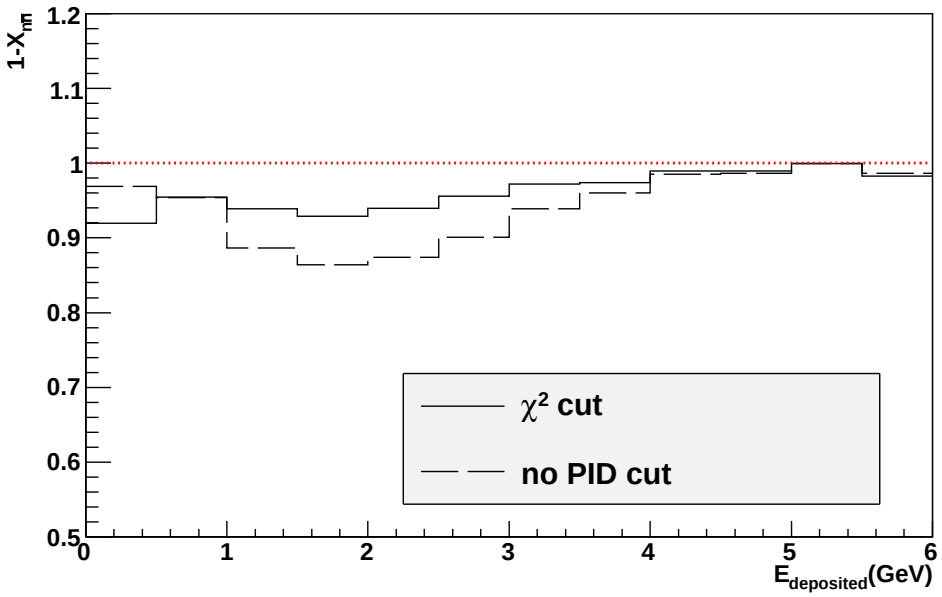

Figure 4.18: Neutron and anti-neutron correction factor $(1-X_{n\bar{n}})$ without any PID cut and with shower shape cut in minimum bias events for PbSc.

The correction factor $1 - X_{n\bar{n}}$ calculation for neutron and anti-neutron is obtained using the same embedding method employed for single photon efficiency study in Section 4.5.1. As shown in Fig. 4.18, the contaminations is largest around $p_T = 1 - 2GeV/c$ due to the large contribution of annihilating of antineutrons. It is very effectively reduced by the shower shape cut in the PbSc and becomes negligible above $p_T = 5GeV/c$.

4.5.5 Conversion Correction

The conversion probability due to the material in front of EMCal is evaluated based on both simulation and budget estimation and summarized in Table 4.1.

e^+e^- pair from conversion outside of the magnetic field can end up in the same cluster in the EMCal since the opening angle between the e^+e^- pair is very small and there is no magnetic field to bend them away from each other. As described in Section 2.4.1, the magnetic field is small at the radial range of $r > 2m$ from vertex, where most of the detector is mounted. e^+e^- pair

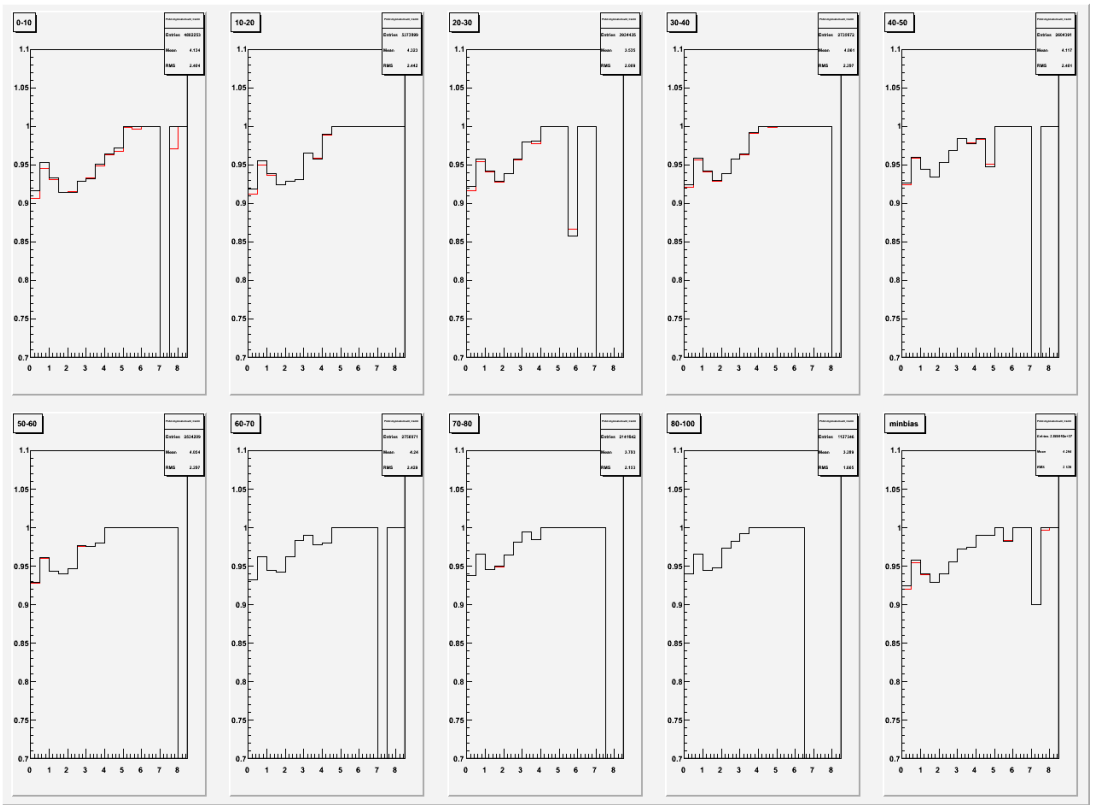

Figure 4.19: Neutron and anti-neutron correction factor $(1-X_{n\bar{n}})$ without any PID cut and with shower shape cut for different centralities events for PbSc.

conserves the most of energy from primary photon and satisfies the identification cuts for photons. Due to the difference of the detector response between photon and electron, the mean of the smearing function for electron clusters is smaller than that for photon clusters by a factor of $\simeq 3\%$. According to the single photon simulation for the sector W0 (10.1% conversion probability), 8.7% of all photons are converted to e^+e^- (or e) ending up in a single cluster and depositing the energy of the primary photon. 1.4% of all photons are converted and lost.

It is also known that the cross section for photon conversion based on the world data set [21] appears to rise slightly by an approximately a couple percent.

Despite of these considerations, since the uncertainty in this trend for both effects is not significant to better than this level, we choose to make a constant conversion loss correction of $p_{conv} = 1-exp(7/9\dot{x}/X_0) = 6\%$ for single photons and include the difference as systematic uncertainties. This results in a total

	Beam Pipe	DC	PC1	RICH	PC2	AGEL	TEC	PC3	TOF	Total
PbSc(W0,2,3)					2.1%	-	-		-	10.1%
PbSc(W1)	0.3%	0.9%	1.2%	3.2%		6.2%	-	2.3%	-	14.8%
PbSc(E2,3)					-	-	5.6%		-	12.7%
PbGl(E0,1)					-	-			1.2%	13.7%

Table 4.1: Conversion probability due to the material in front of the EMCal.

uncertainty in the conversion correction of 2% which covers the uncertainty in the budget estimation as well as the possible rising trends.

4.6 Fast Monte-Carlo Simulation

A fast Monte Carlo simulation based on Exodus with PHENIX Run4 setup is used to determine R_{MC} in Eq. 4.6. Within this fast Monte Carlo, π^0 are generated with the following characteristics:

- Flat transverse momentum distribution $0 < p_T < 20 GeV/c$
- Uniform vertex distribution $\|z_{vtx}\| < 30 cm$
- Gaussian rapidity distribution around zero in the interval $\|y\| < 0.45$.
- Uniform ϕ distribution

Then the decay photon p_T spectrum is weighted by the measured π^0 spectrum with a fit to PHENIX data with a modified Hagedorn function.

$$\frac{1}{(2\pi p_T)}\frac{d^2N}{dp_T dy} = \frac{c}{(exp(-ap_T - bp_T^2) + p_T/p_0)^n} \tag{4.17}$$

where $c = 377 \pm 60 mb GeV^{-2}$, $a - 0.356 \pm 0.014 (GeV/c)^{-1}$, $b = 0.068 \pm 0.019 (GeV/c)^{-2}$, $p_0 = 0.7 \pm 0.02 GeV/c$ and $n = 9.25 \pm 0.04$ [16]. To parameterize other hadron spectra, the modified Hagedorn fit of π^0 data is m_T scaled by replacing p_T in Eq. 4.17 by $\sqrt{(p_T/c)^2 - m_{\pi_0}^2 + m_h^2}$ where m_h is the mass of the hadron. The good description of data by Hagedorn function fit for π^0 is shown in Fig. 4.20.

Under the m_T scaling assumption, the spectra shapes are all assumed to be the same when plotted as a function of m_T but with different absolute normalization at high p_T with respect to π^0. For the η, which dominates the decay photon background besides π^0 at about 20% level, we use normalization factor of 0.45 based on PHENIX published measurement [99] shown in Fig 4.21. For the η' and ω mesons, the normalization is based on world average

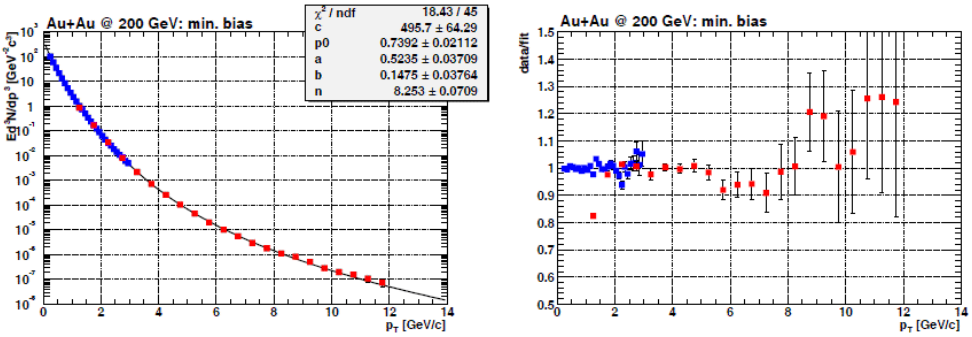

Figure 4.20: Fit of the combined charged $\pi^+\pi^-$ (blue symbols at low p_T) and π^0 spectra (red symbols at hight p_T) according to Eq.4.17 in minimum bias collisions (left panel) and ratio of data and fit (right panel). Error bars are statistical uncertainties only.

[100], a conservative value of 0.8 is employed. Both of these mesons contribute decay photons at the less-than-few percent level.

Once the meson yield and the p_T spectra are known, the photon spectrum from hadronic sources is given by the decay kinematics and the branching ratios in Table 4.2, which are implemented in EXODUS simulation framework. For Dalitz decays $\pi^0, \eta \rightarrow \gamma e^+ e^-$, the Kroll-Wada expression [101] is used with electromagnetic transition form factors measured by the Lepton-G collaboration [102]. All vector mesons are assumed to be unpolarized. For Dalitz decays of which the third body is a photon, the angular distribution is sampled according to $1 + \lambda cos^2\theta_{CS}$ distribution, where θ_{CS} is the polar angle of the electrons in the Collins-Soper frame [103].

Photons from hadron decays are filtered into the PHENIX EMCal acceptance with an implementation of the EMCal and PC3 deadmap. Unlike embedding framework to determine single photon detection efficiency in Section 4.5.1, this fast Monte Carlo simulation does not generate shower by depositing photon energy at EMCal tower level and reclustering. It simply assumes that photon will be measured if it hits the active area. The momentum is smeared to take into account the effect of the EMCal energy resolution as defined in Eq. 3.1. The resulting R_{MC} is shown in Fig. 4.22.

4.7 Summary of Systematic Uncertainties

Various sources of systematic uncertainties are described in this section. The systematic uncertainties on inclusive photon yield and direct photon excess

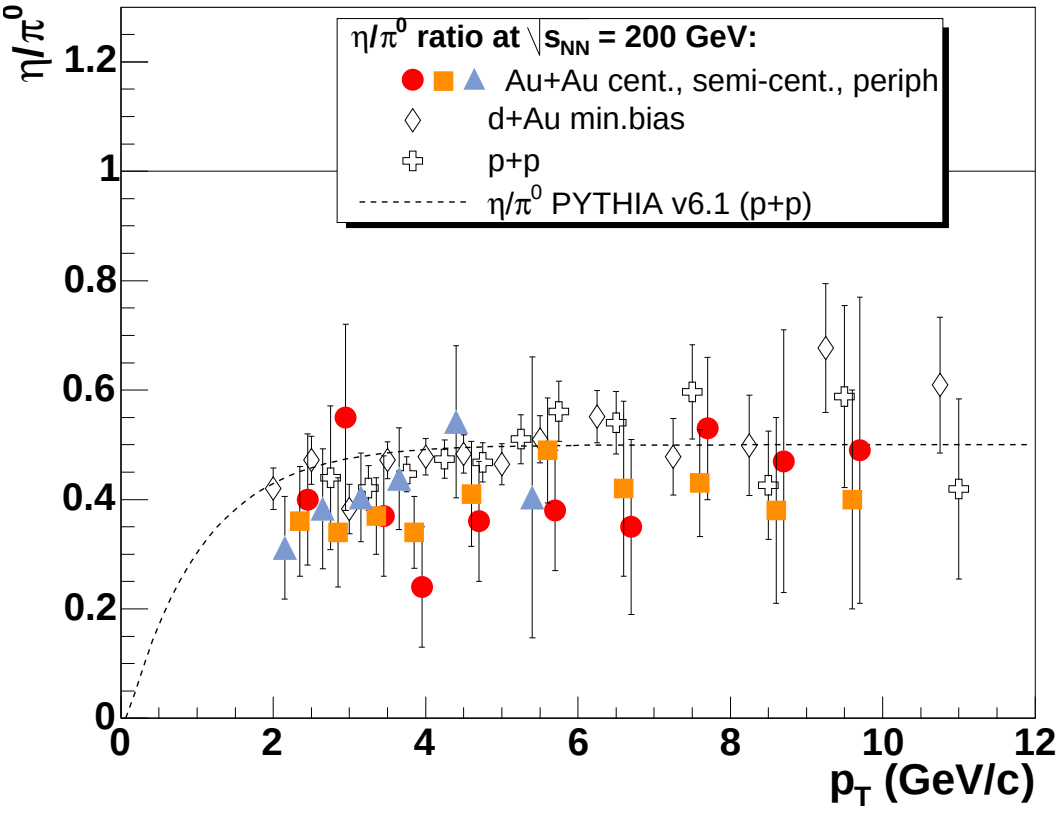

Figure 4.21: Au+Au R_{η/π^0} ratio in MB and three centrality classes (0-20, 20-60, 60-92%) as a function of p_T compared to the ratio in $d+Au$ and $p+p$ collisions. The error bars include all point-to-point errors. The dashed line is the prediction of PYTHIA[15] for $p+p$ at this center-of-mass energy. A few $R_{\eta/\pi^0}(p_T)$ ratios have been slightly displaced to the left or right($\pm 50 MeV/c$) along the p_T axis to improve the clarity of the plot.

ratio are respectively summarized in Table 4.4 and Table 4.3. As described in Sec 4.1, some parts of the systematic uncertainties in direct photon excess ratio, such as the clean photon efficiency and acceptance which are hard to estimate, cancel out. Uncertainties on some correction factors such as conversion loss are already discussed in previous sections. The following sections describe in more detail uncertainties which were not covered before. The largest uncertainties in both direct photon excess ratio and inclusive photons come from the hadron contamination especially at low-p_T.

Particle State	Mass(MeV)	R_{h/π^0}	Decay Channel	Branching Ratio
π^0	134.98	-	$\gamma\gamma$	98.798%
			$e^+e^-\gamma$	1.198%
η	547.8	0.45	$\gamma\gamma$	39.43%
			$\pi^+\pi^-\gamma$	4.68%
			$e^+e^-\gamma$	$6.0 \cdot 10^{-3}$
			$\pi^0\gamma\gamma$	$7.2 \cdot 10^{-4}$
			$\mu^+\mu^-\gamma$	$3.1 \cdot 10^{-4}$
ρ^0	769.0	1.0	$\pi^+\pi^-\gamma$	$9.9 \cdot 10^{-3}$
			$\pi^0\gamma$	$6.0 \cdot 10^{-4}$
			$\eta\gamma$	$3.0 \cdot 10^{-4}$
ω	782.6	1.0	$\pi^0\gamma$	8.92%
			$\eta\gamma$	$4.9 \cdot 10^{-4}$
η'	957.8	1.0	$\rho^0\gamma$	29.5%
			$\omega\gamma$	3.0%
			$\gamma\gamma$	2.12%
			$\mu^+\mu^-\gamma$	$1.0 \cdot 10^{-4}$
K_S^0	497.65	1.0	$\pi^0\pi^0$	31.05%

Table 4.2: Dominant sources of background photons from decays of hadrons and the corresponding m_T scaling factors relative to the π^0 measurement R_{h/π^0}. The listed masses, decay branches, and the branching ratios are taken from [21]

.

4.7.1 Systematic uncertainty for γ efficiency

We are only concerned about how accurate our efficiency calculation derived from simulation really are. In this section we mean to exclude the additional complications of the embedding reproduction of occupancy effects due to the high multiplicities of central events, rather focusing on the base PISA simulation itself and its response to photons with various cuts, especially PID cuts introduced in Section 4.3.1 for this analysis.

The best way to derive an uncertainty in the simulation is to identify a clean photon or electron sample and study the distribution of clustering and shower shape parameters which can be measured and compared to real data. When a difference is found, a tuning parameter that causes the distribution to change in the simulation can be modified until the simulation reproduces the real data, or until the propagated uncertainty due to the difference is understood. This is how systematic uncertainties can be reduced. Such work is very time consuming because of the large computation time involved in the full showering

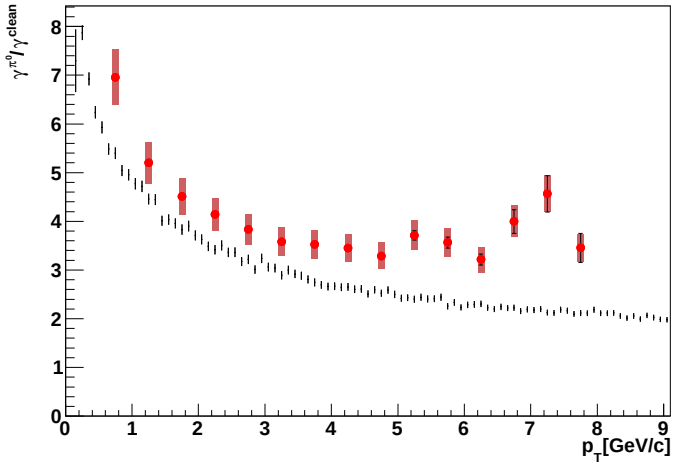

Figure 4.22: $\gamma^{\pi^0}/\gamma^{clean}$ from data(red) and Monte-Carlo simulation(black), where γ^{clean} is after PC3Veto PID cut from real data but for Monte-Carlo simulation γ^{clean} is only from hadronic decays.

	p_T indep.	1GeV/c	3GeV/c	5GeV/c
peak extraction	3%			
γ efficiency	1%			
$n\bar{n}$ contamination		3.5%	1%	1%
charged hadron contam.		2.4%/16.4%	1.1%/4.7%	0.6%/1.2%
conversion correction	2%			
acceptance	5%			
η/π^0	3%			
π^0 param	1%			
p_T cut	2%			
Total		8.4%/18.3%	7.4/8.7%	7.4%/7.4%

Table 4.3: Systematic uncertainties of direct photon excess double ratio. The total uncertainties for a given p_T column is the quadratic sum of the p_T-dependent uncertainties given in that column and the p_T-independent uncertainties. Different systematic uncertainties in charged hadron contamination and Total are shown separately for clean photon sample from PC3-veto cut(left) and StochasticCut2(right).

reconstructions in GEANT. However because the base PISA simulation does a good job on energy response for electromagnetic showers and describes hadron showers reasonably well[93], we can simply vary the shower shape χ^2 PID cut

	p_T indep.	2GeV/c	6GeV/c
γ efficiency	1%		
hadron contamination		7%	6%
conversion correction	2%		
acceptance	5%		
p_T cut	2%		
energy smearing		8%	6%
Total		12.1%	10.3%

Table 4.4: Systematic uncertainties of inclusive photons. The total error for a given p_T column is the quadratic sum of the p_T-dependent uncertainties given in that column and the p_T-independent uncertainties.

by 1σ and compare how the simulation reproduces the real data, which gives us realistic measurement of how large the uncertainty in the simulation is (Fig. 4.23). We make a conservative estimation of the systematic uncertainties for single photon efficiency with χ^2 PID cut 1%.

4.7.2 Systematic uncertainty for π^0-tagged photons

As indicated in Section 4.4.2, even after combinatorial background subtraction, there are still some residuals underneath π^0 peak, which is the major source of uncertainties on peak extraction. Therefore different counting methods described below are implemented to estimate this variation.

- integrate in $\mu \pm 1.0\sigma$
- integrate in $\mu \pm 2.0\sigma$
- integrate in $\mu \pm 3.0\sigma(default)$
- subtract polynomial background then integrate in $\mu \pm 1.0\sigma$
- subtract polynomial background then integrate in $\mu \pm 2.0\sigma$
- subtract polynomial background then integrate in $\mu \pm 3.0\sigma$

π^0 tagged photons from these six different counting methods then are compared with default measurement and difference in ratio are plotted in Fig. 4.24. Therefore 3% systematic uncertainty is assigned which can be used to cover 2σ of these variations.

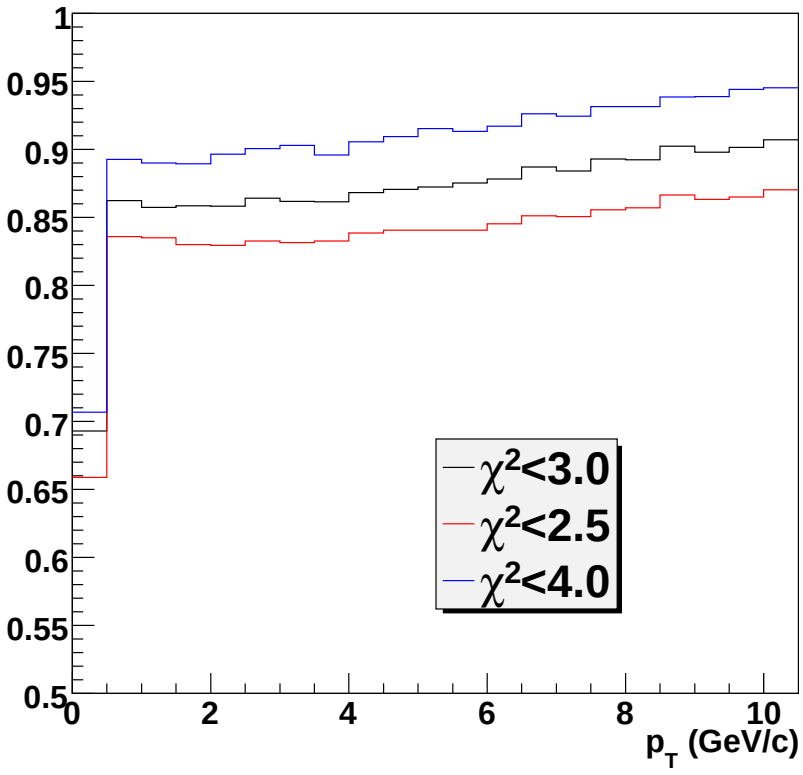

Figure 4.23: Single photon reconstruction efficiency for Au+Au 200GeV min. bias collisions in PbSc with various χ^2 cut on loose photons.

4.7.3 Systematic uncertainty for hadron contamination

The hadron contamination is estimated with a full GEANT simulation which also includes the detector response. The results depend on how well hadrons are described by the simulation for both their overall energy deposit and the shape of hadron shower. For low-p_T region, the hadron contamination is quite large as shown in Fig. 4.17. The corresponding systematic uncertainty is estimated by comparing the fully corrected inclusive photon spectrum, calculated with different particle identification criteria. The systematic uncertainty is relatively small at high-p_T because the hadron contribution is dominant at low-p_T region around MIP, while there is large deviation between no particle identification and other particle identification at $p_T = 0 - 3GeV/c$, which means that the hadron contamination is not fully reproduced with GEANT simulation. However for clean photon sample with PC3-veto cut the contamination ratio

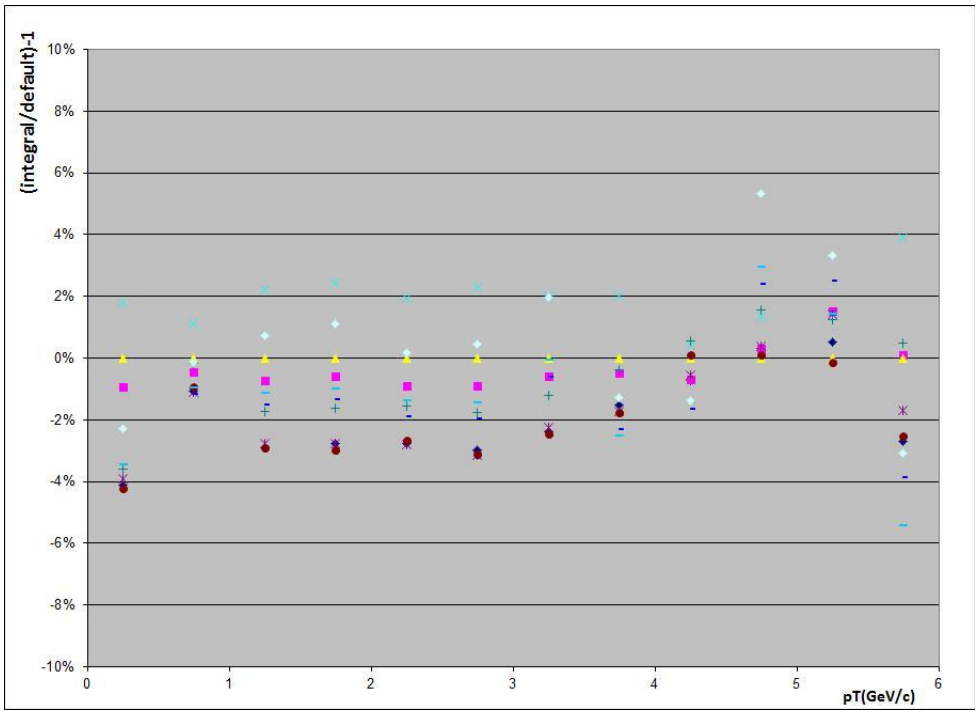

Figure 4.24: Comparison of π^0-tagged photons for different window and counting methods. It shows ratio difference between different counting methods and default one.

X_{hadron} is significantly reduced with a very conservative estimation of PC3 efficiency at level of 95% [95], which leads to $1-3\%$ systematic uncertainty. Fig. 4.17 shows StochasticCut2 does a much better job on rejecting hadron than χ^2 cut but there is still considerable amount of contamination at low-p_T therefore a much larger systematic uncertainty of $1-15\%$ is assigned by using half of contamination ratio X_{hadron}.

Chapter 5

Results and Discussion

5.1 γ/π^0 Double Ratio

The direct photon fraction R_γ shown in Fig. 5.1 is calculated using the new tagging method described in Section 4.1. Results for two different photon PID cuts used to get clean photon sample from EMCal are displayed. Both results are given as a function of p_T for minimum bias Au+Au collisions at $\sqrt{s_{NN}} = 200GeV$. While it is challenging to extract the direct photon signal due to the large background, the ratios appears to be consistent with each other underlining the robustness of the new tagging method. In Fig. 5.2, R_γ is compared to the earlier measurement using a totally different method based on internal conversions (see Section 1.4.4). The two methods produce consistent results.

Recently the tagging method developed in this thesis was used with photons reconstructed through photon conversions to e^+e^- pairs in the detector materials. Preliminary measurement of R_γ from PHENIX Run7 and Run10 data [104] are presented in Fig. 5.3 together with results from this thesis, where a good agreement is observed again. There is a clear and well established enhancement of R_γ above unity as well as the presence of direct photon at low p_T.

5.2 Direct Photon Yield

In this section the direct photon yield is determined from the masurement of R_γ. This can be achieved by either starting from the measured inclusive photon yield or the modeled yield of photons from hadronic decays. The conversion is given in Eq. 5.1 and 5.2.

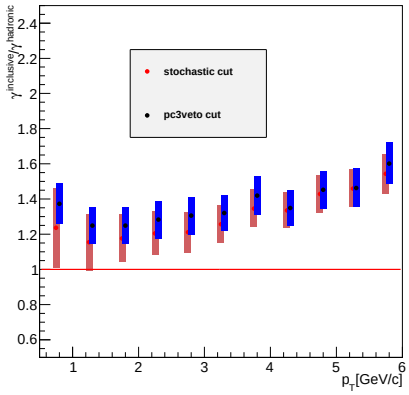

Figure 5.1: Double-ratio comparison between two different clean photon sources with different PID cuts from EMCal for PHENIX Run4 min-bias in Au+Au $\sqrt{s_{NN}} = 200GeV/c$. Red is using clean photons from StochasticCut and Black is using PC3Veto plus TOF as photon PID cuts discussed in Section 4.3.2.

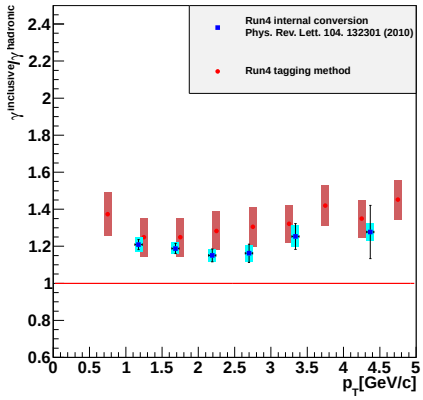

Figure 5.2: Double-ratio comparison between two different methods for PHENIX Run4 Au+Au min-bias $\sqrt{s_{NN}} = 200Gev/c$ result. Blue is from internal conversion method [11] and Red is from tagging method.

$$\gamma_{direct} = \gamma_{inc} - \gamma_{hadron} = R_\gamma \gamma_{hadron} - \gamma_{hadron} = (R_\gamma - 1)\gamma_{hadron} \tag{5.1}$$

$$\gamma_{direct} = \gamma_{inc} - \gamma_{hadron} = \gamma_{inc} - \gamma_{inc}/R_\gamma = (1 - \frac{1}{R_\gamma}) \times \gamma_{inc} \tag{5.2}$$

The inclusive photon yield and the yield of decay photons are shown in Fig. 5.4. The inclusive photon spectrum is derived from the raw cluster spectrum and is fully corrected as discussed in Section 4.5 following Eq. 4.9. The hadron decay photon yield is calculated from a fast Monte Carlo simulation EXODUS as discussed in Section 4.6, which has the advantage of smaller systematic uncertainties since photon efficiency and other correction factors are not needed.

The spectra shown in Fig. 5.4 are converted into direct photon spectra using Eq. 5.1, 5.2 and the measured R_γ. The comparison is shown in Fig. 5.5 where the direct photon yield calculated from R_γ and the measured inclusive photon yield has larger systematic uncertainties than the direct photon yield

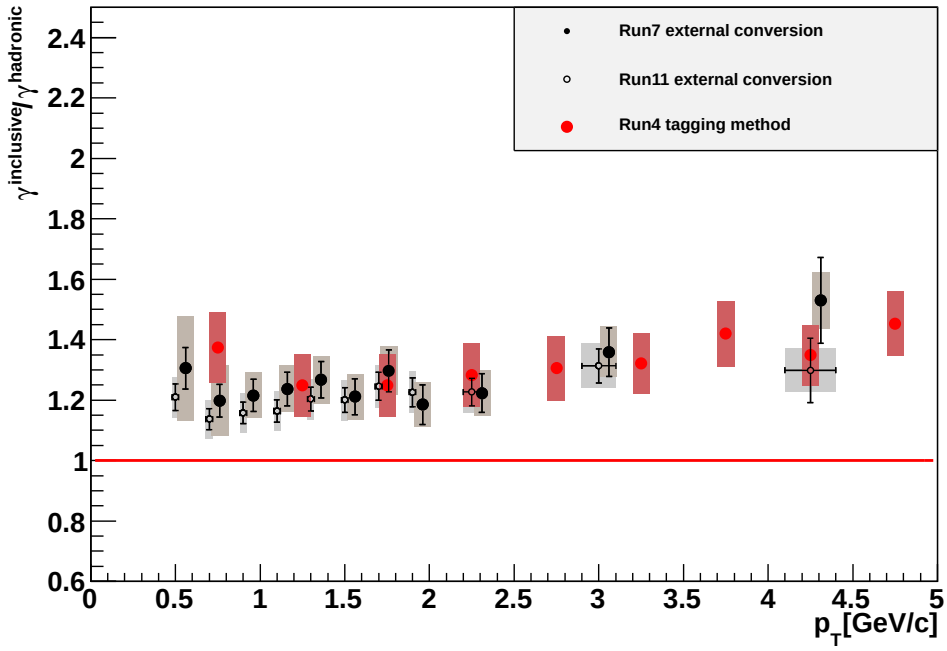

Figure 5.3: Double-ratio comparison with PHENIX Run7 (black solid) and Run10 (black circle) published result using the same method but with different clean photon sources of external conversion from HBD than EMCal clusters (red).

calculated from the hadronic decay photon cocktail yield since the photon acceptance and efficiency do not cancel as they do in the double ratio of R_γ. The lower panel of the figure shows the ratio of these two direct photon measurements. The agreement is good within uncertainties. In the top panel the earlier PHENIX measurements of direct photon [1, 11] from the internal conversion method are also reproduced and the agreement is again excellent. In the low-p_T region the direct photon spectra are approximately exponential and can be well characterized by their inverse logarithmic slope T_{eff}. Above 3GeV/c p_T region the spectrum has a power-law shape characteristic for contributions from hard scattering processes, indicating that this part of the direct photons are from hard scattering processes early in the collision before a medium is formed.

The direct photon yield in p+p collisions can be used as baseline to remove primordial production. To determine this contribution, a fit to the published p+p data in [11, 12, 105] is done with a modified power law function ($A_{pp}(1+p_T^2/b)^{-n}$). The result is showed in Fig. 5.6. The pp fit can be scaled by the

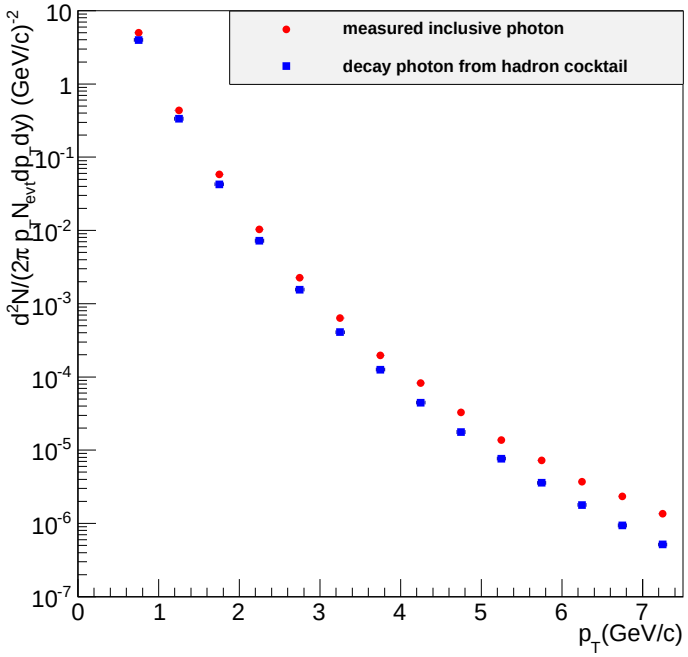

Figure 5.4: Fully corrected inclusive photon spectrum (red) for PHENIX Run4 min-bias in Au+Au $\sqrt{s_{NN}} = 200 GeV/c$ collisions with decay photon spectrum (blue) from Exodus simulation by using hadron cocktail [16].

nuclear thickness function T_{AA}, which accounts for the increased probability of hard scattering in Au+Au compared to p+p due to more participant particles. T_{AA} is calculated from a Glauber Monte Carlo simulation and listed in Table 5.1 with the corresponding systematic uncertainties from [22].

The direct photon spectrum is now analyzed by fitting an exponential plus the T_{AA}-scaled p+p fit function $(Ae^{p_T/T} + T_{AA} \times A_{pp}(1 + p_T^2/b)^{-n})$ to the Au+Au data. The only free parameters in the fit are A and the inverse slope T of the exponential term. The results of the fit is presented in Fig. 5.7. The extracted inverse slope parameter from the fit $T_{eff} = 210 \pm 17(stat) \pm 15(sys) MeV$ for min-bias collisions with statistical error (extracted from the fit) and systematic uncertainty (extracted by moving all points up and down by their respective systematic uncertainties and refitting). The value is in agreement with previously published result $T_{eff} = 233 \pm 14(stat) \pm 19 sys MeV$ [11].

The value of effective temperature is well above the critical temperature $T_c \simeq 155 - 170 MeV$ [106, 107] for the deconfinement phase transition. The

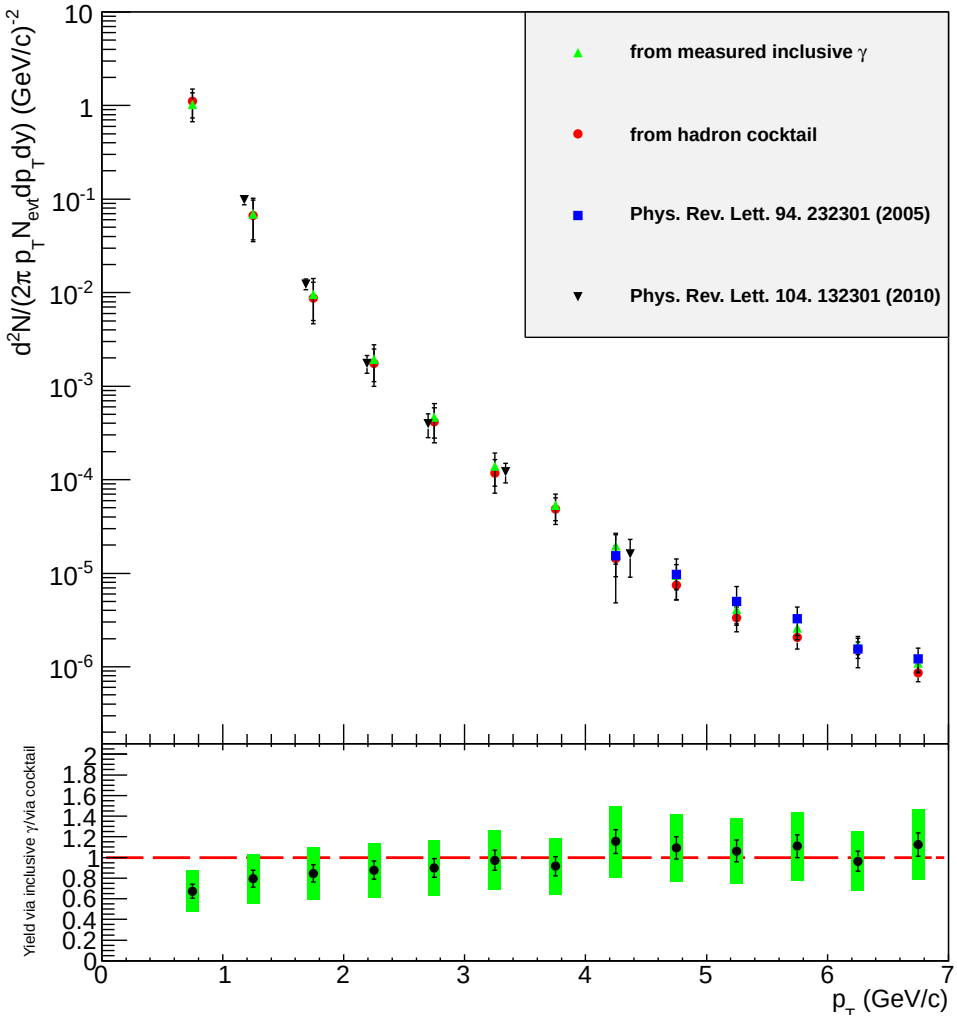

Figure 5.5: Direct photon spectrum for PHENIX Run4 Au+Au $\sqrt{s_{NN}} = 200GeV/c$ min-bias. The top plot shows direct photon invariant yield from this tagging method analysis by using both measured inclusive photons (Green) and photons from hadronic decay (Red). The bottom plot shows the ratio of the two. The combined result of two (Blue and Black) direct photon measurement published by PHENIX is also presented in the top plot.

hydrodynamic model studies reported in [11, 108] show that this observation is consistent with much higher temperatures at a very early stage of the expansion of the collision fireball. The fact of T_{eff} being larger than T_c in itself does not prove that the radiation was emitted from a quark-gluon plasma. It

Centrality	T_{AA}	sys. error	N_{part}	sys. error	N_{coll}	sys. error
0-20%	18.55	1.27	279.9	4.0	735.2	14.6
20-40%	7.06	0.58	140.4	4.9	333.2	10.7
40-60%	2.15	0.25	59.9	3.5	126.5	6.1
60-90%	0.35	0.1	14.5	2.5	30.2	4.7
0-90%	6.14	0.45	109.1	4.1	290.0	8.8

Table 5.1: T_{AA}, N_{part} and N_{coll} values calculated from a Glauber Monte Carlo simulation [22].

could in principle also be due to radiation from the late stages of the collision where the true fireball temperature is already below T_c but strong radial flow boosts the emission spectrum to an effective temperature $T_{eff} > T_c$. A more detailed comparison to theoretical models is needed to interprete the results.

5.3 Comparison with theoretical models

There are two fundamentally different standard theoretical approaches to calculate thermal photon emission. Transport models are based on transport theory of relativistic quantum many-body systems which follows individual particles throughout the collisions and simulates their scattering processes in time steps. Photons are emitted in individual scattering processes. In contrast, hydrodynamical approach simulates a space-time evolution of the collisions, under the assumption of local conservation of energy and momentum. The collision system evolves according to the equations of motion of perfect relativistic hydrodynamics complemented with a set of initial conditions (e.g. initial temperature T_{init} at thermalization time τ_0, the equation-of-state of the system and the freeze-out conditions). In each time step photons are emitted from volume cells according to thermal rates calculated from relativistic kinetic theory[7].

Standard Hydrodynamics

Ideal hydrodynamics, which does not include viscous effects, was first used to describe bulk properties of heavy-ion collisions [109–111] before the first RHIC results became available. The good agreement of experimental RHIC data with these models is one of the foundations to conclude that the QGP produced at RHIC behaves like a strongly coupled liquid. Precise data available today have also established the importance of viscous effects and that the shear viscosity to entropy ratio is very small.

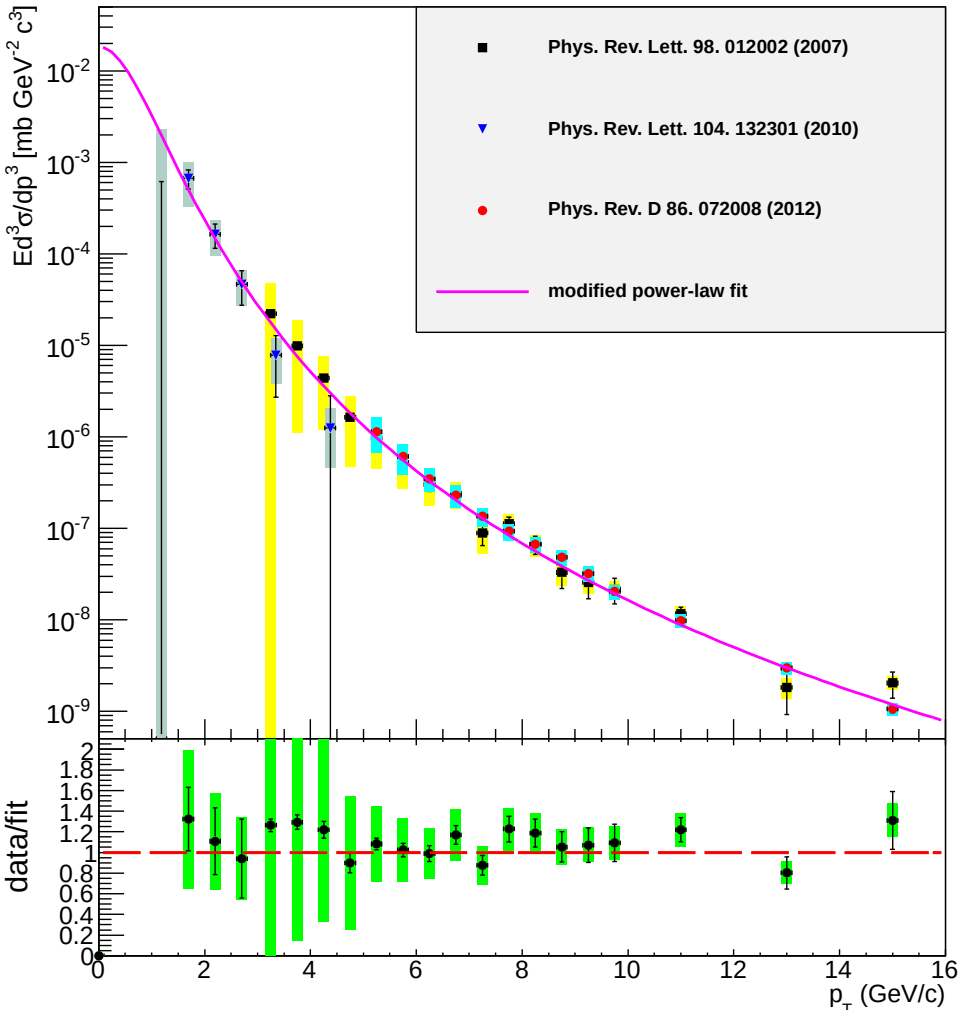

Figure 5.6: Fits to various PHENIX published direct photon data in $\sqrt{s_{NN}} = 200GeV$ p+p collisions where $A_{pp} = 0.01834 \pm 0.01457$, $b = 1.432 \pm 0.5949$ and $n = 3.27 \pm 0.1746$ with $\chi^2/ndf = 10.19/15$.

In [17] the hydrodynamic simulation for the photon emission starts the evolution at $\tau_0 = 0.6fm/c$, corresponding to a peak initial temperature in the medium center of $T_0 = 370MeV(e_0 = 35GeV/fm^3)$ for Au+Au collisions at $0 - 20\%$ centraility and ends on an isothermal hadronic freeze-out surface of temperature $T_{dec} = 120MeV$. The result includes the thermal rates corrected for shear viscosity effects integrated over the viscous hydrodynamical space-time evolution. The interplay of the collective expansion and effective temper-

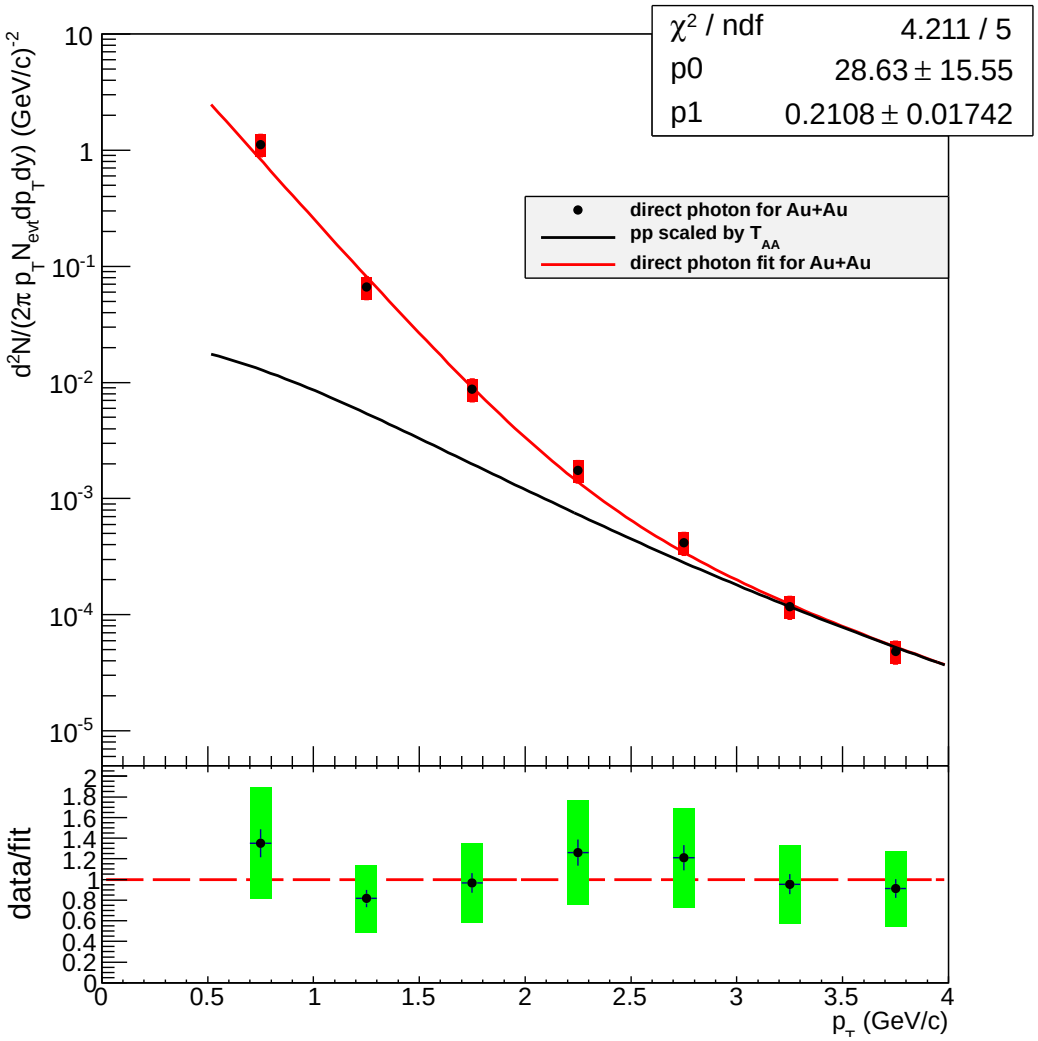

Figure 5.7: Fits to direct photon invariant yield in $\sqrt{s_{NN}} = 200GeV$ Au+Au collisions.

ature (or inverse slope) of the thermal photon spectrum discussed previously in a qualitative way can be studied quantitatively in these models. Fig. 5.8 maps temperature, yield and effective slope of the thermal photon spectrum through the space time evolution. The circles in Fig. 5.8 show the effective temperatures of photons emitted with equilibrium rates (open black circles) and with viscously corrected rates (filled red circles) from cells of a given temperature within the hydrodynamically evolving viscous medium [17]. The area of the circles is proportional to the total photon yield emitted from all cells

at that temperature. As the system cools, Fig. 5.8 shows that the effective photon temperature begins to deviate upward from the true temperature. Below $T \simeq 220MeV$ the effective photon temperature actually begins to increase again while the true temperature continues to decrease, which is caused by the strengthening radial flow. Most photons are emitted from a relatively narrow temperature band between 165 and $200MeV$. Fewer photons come from late in the collision or much earlier.

As discussed in [17], the emission of thermal photons near the phase boundary is strongly affected by the 'blue shift' due to collective flow, thus the large T_{eff} does not directly prove the emission of electromagnetic radiation from the quark-gluon plasma with temperatures well above T_c. However, the large T_{eff} through the comparison with models provides evidence that temperatures above T_c were reached.

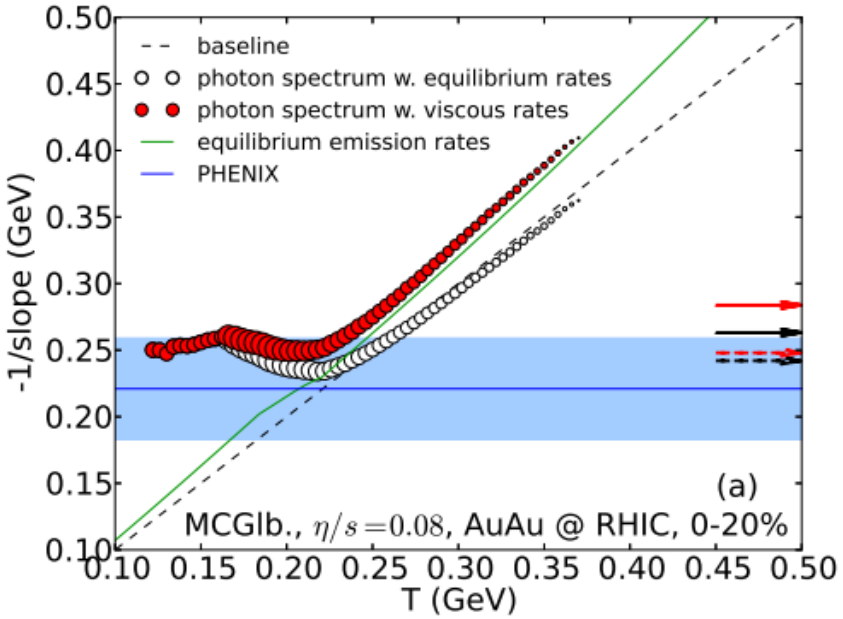

Figure 5.8: The inverse photon slope parameter $T_{eff} = -1/slope$ as a function of the local fluid cell temperature, from the equilibrium thermal emission rates (solid green lines) and from hydrodynamic simulation (open and filled circles) [17], compared with Au+Au collisions at RHIC.

Up to now this discussion has focused on the slope of the spectra. Next we will look at the yield. In order to obtain min-bias direct photon spectrum from $0-20\%$ and $20-40\%$ spectra presented in [17], a correction factor is applied to include more peripheral bins. The yield per event is scaled down to $0-92\%$ centrality by assuming for each centrality class the yield scales

as $N_{part}^{1.5}$, which is consistent with [112], and that the spectral shape does not change significantly. The result is shown as blue line in Fig. 5.9. While the effective temperature was described well in Fig. 5.8, the yield is underpredicted by a factor of $\simeq 5$. Similiar underprediction of the yield is found in other hydrodynamics calculations [113–115].

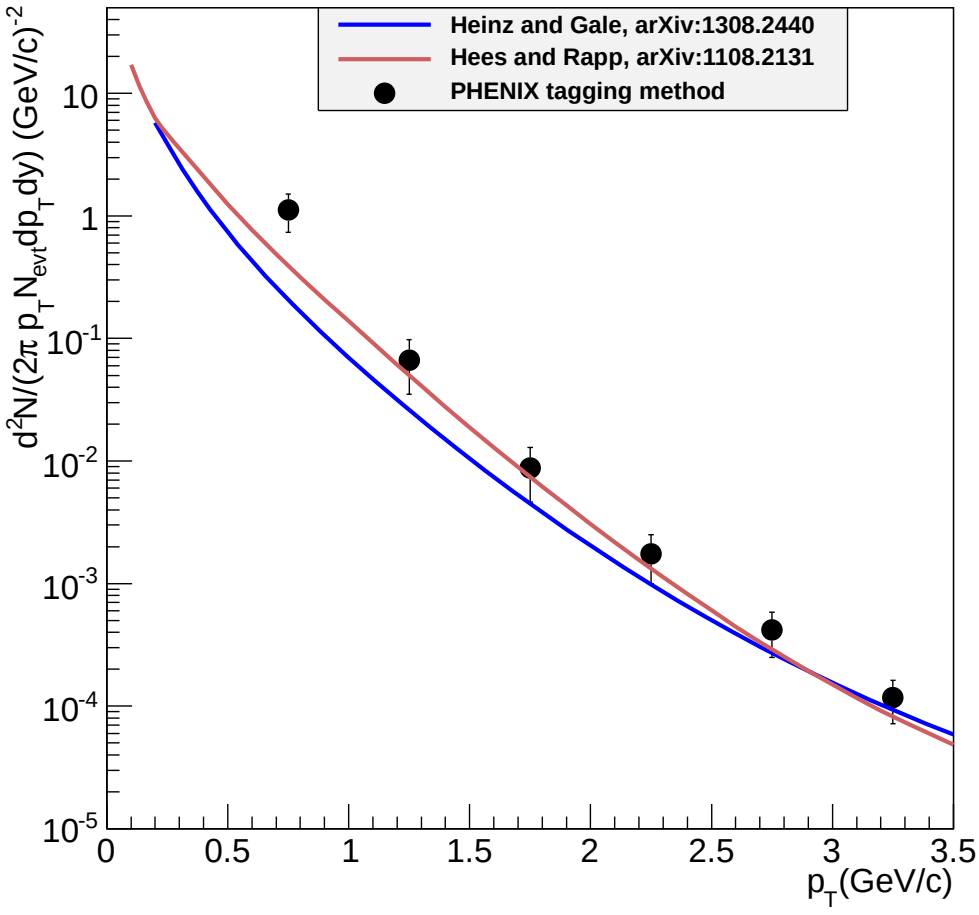

Figure 5.9: Direct photons from different hydrodynamics approach (blue[17] and brown[18] line, adjusted from calculation of central collisions to minimal bias assuming the yield of each centrality class scales as $N_{part}^{1.5}$) in comparison to PHENIX Run4 data for minimal bias collisions of Au+Au at $\sqrt{s_{NN}} = 200GeV$ (black symbols).

Recent PHENIX measurements of the elliptic flow of direct photons [77] have further shown that the pertinent flow coefficient v_2 is as large as that

of charged pions is difficult to reconcile with current standard hydrodynamic model calculations. A parametrized expanding fireball model is proposed in [18] to improve the description of thermal photon production at RHIC by having a larger space-time volume contributing to low-temperature emission. The space-time evolution of each cell and its temperature is tracked with time while the photon emission for each time step is calculated according to an emission rate for the appopriate phase of the matter. It assumes an initial longitudinal fireball size of $z_0 = 0.6fm$ with total entropies of $S = 7900$ and 3600 for $0-20\%$ and $20-40\%$ centrality class, which translates into average initial temperatures of $T_0 \simeq 355MeV$ and $325MeV$. The fireball of lifetime $\tau \simeq 15fm/c$ results in a freezout temperature of $T_{fo} = 98MeV$ with a surface transverse flow of $\beta_s = 0.77$.

After taking into account the radial flow built up in the fireball at the end of the QGP phase which is underestimated in typical hydrodynamical evolutions, contributions from baryons and chemical off-equilibrium effects in the hadronic phase, the direct photon spectra calculated in [18] indicates that the hadronic radiation spectrum becomes noticeably harder while the spectral distribution of the QGP radiation is barely affected. In combination with an improved estimate of the primordial emission, adjusted to available PHENIX *pp* data, the result (red line) in Fig. 5.9 shows better agreement with our measurement (black dots) but still underestimates the yield by a factor of ~ 2.

Parton-Hadron-String Dynamics

The Parton-Hadron-String Dynamics (PHSD) transport approach is based on a microscopic and non-equilibrium evolution of the nucleus-nucleus collision which can calculate a multitude of hadronic and electro-magnetic observables in a wide energy range [116–118]. It has provided a consistent description of the bulk properties of heavy-ion collisions including rapidity spectra, transverse mass distributions and azimuthal asymmetries of various particle species from SPS to RHIC energies [119] and was successfully used also for the analysis of dilepton production from hadronic and partonic sources at SPS, RHIC and LHC energies [117]. It is also well suited to calculate direct photon production in relativistic heavy-ion collisions. The photons are emitted from hadronic and partonic scattering processes in the transport calculation.

The following sources of direct photons are taken into account in Fig. 5.10.

- the decays of $\omega, \eta^{'}, \phi$ and a_1
- the reactions $\pi + \rho \rightarrow \pi + \gamma, \pi + \pi \rightarrow \rho + \gamma$
- the photon bremsstrahlung in meson-meson and meson-baryon collisions $m + m \rightarrow m + m + \gamma$, $m + B \rightarrow m + B + \gamma$

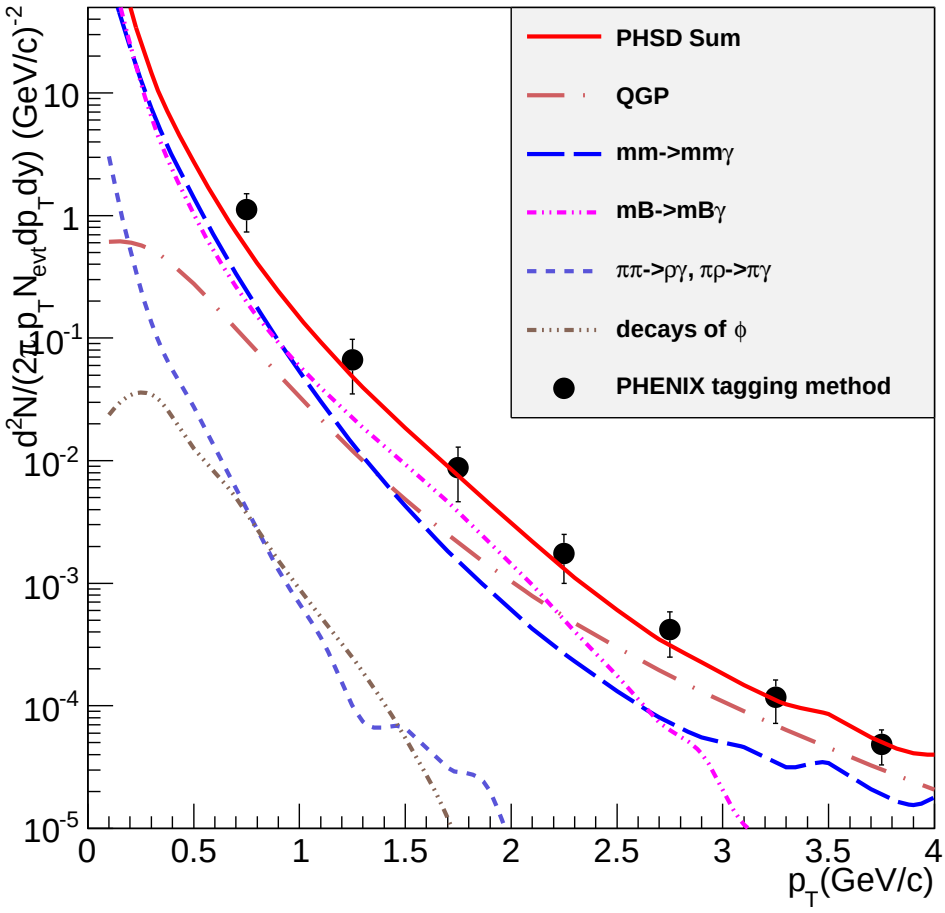

Figure 5.10: Direct photons from PHSD approach (red solid line) in comparison to PHENIX Run4 data for minimal bias collisions of Au+Au at $\sqrt{s_{NN}} = 200GeV$ (black symbols). The various channels are described in the legend.

- the photon production in the QGP in the processes of $q + \bar{q} \rightarrow g + \gamma$ and $q(\bar{q}) + g \rightarrow q(\bar{q}) + \gamma$ as well as the photon production in the initial hard collisions (pQCD) which is given by the hard photon yield in p+p collisions scaled with the number of binary collisions N_{coll}.

We find that PHSD calculations, shown in Fig. 5.10 as PHSD sum in red, are in a reasonable agreement, at least within a factor of 2, with this analysis and show a clear dominance of the hadronic production channels over the

partonic channels for transverse momenta below about 0.7GeV/c. In particular, the bremsstrahlung contributions are responsible for the non-exponential shape of the spectrum and the strong increase for low p_T. This increase should be softened to some degree by the Landau-Pomeranchuk-Migdal (LPM) effect [120] when it is taken into account.

The inverse slope of the spectrum is about $\simeq 260MeV$[17]. Due to the non-exponential shape of the photon spectra this slope depends on the fitting interval in p_T. Since in PHSD the dominant contributions to the thermal photon yield are hadronic bremsstrahlung channels, the high slope parameters predominantly reflect the 'blue shift' of the photon spectra[17]. However the overall yield is still somewhat lower than the observed yield.

5.4 Conclusions

We have presented an analysis of both the inclusive and the direct photon yields in the low-to-mid p_T range at mid-rapidity in Au+Au min-bias collisions at $\sqrt{s_{NN}} = 200GeV/c$ for the PHENIX 2004 dataset. The measurement employed a novel tagging technique in which a photon sample of high purity is generated using a stringent charged particle veto and tight fiducial cuts. The direct photon fraction R_γ is calculated through a double ratio to further reduce systematic uncertainties by tagging photons as π^0 decay photons. The reconstruction efficiency and acceptance of the tagged photons, which are major sources of systematic uncertainties, explicitly cancel. The same method has subsequently been successfully applied to direct photon measurements via external conversions[73, 74] to further remove hadronic contamination and measure down to lower p_T for PHENIX 2007 and 2010 data set. All these measurements show good consistency with each other, indicating the success of this method in significantly reducing uncertainties on R_γ compared to previously published result[1]. This analysis also serves as an important cross-check for the direct photon measurement through the internal conversion method[11]. The direct photon fraction R_γ measured from real photons and from virtual photons is consistent within uncertainties and indicates a well established direct photon yield, which is $\geq 20\%$ of inclusive photon yield.

This analysis also extended p_T reach to below $1GeV/c$ compared to [11] which allows for an improved constraint on the possible exponential shape of the spectrum. The effective temperature of data is $T_{eff} \simeq 210MeV$, which points towarding initial temperature $T_0 \geq 300MeV$, much higher than the critical temperature $T_c \simeq 155 - 170MeV$ for the deconfinement phase transition. Even though current theoretical models [17–19] can interpret this value as the consequence of a 'blue-shift' of the photon spectra due to the collective flow

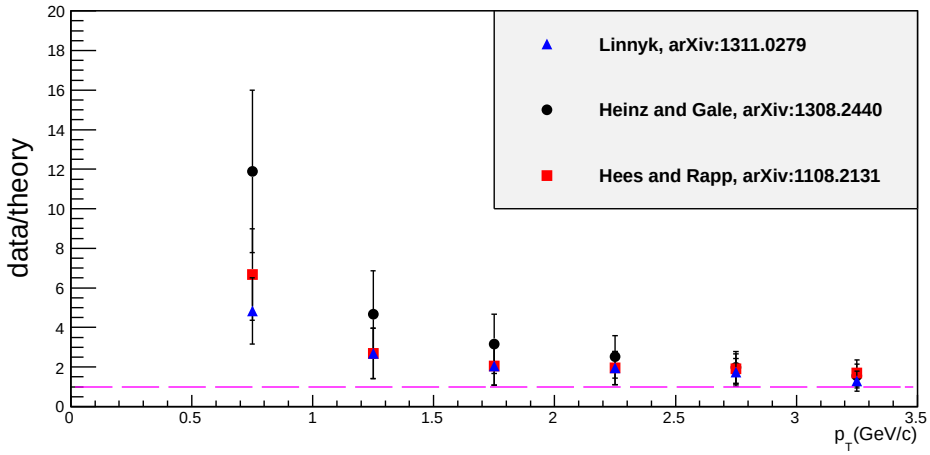

Figure 5.11: Ratio between direct photons yield from the tagging method measurement using PHENIX Run4 data and different theoretical model calculation [17–19] for min-bias collisions of Au+Au at $\sqrt{s_{NN}} = 200GeV$.

of hadrons which distorts the exponential shape, a quantitative comparison shows in Fig. 5.11 that the yield under the same assumption is significantly under-estimated by a factor of 2 at moderate p_T and 4-12 at low p_T. Many novel sources of direct photons have been proposed to solve this discrepancy of the thermal photon yield.

In [121], the photon production rate to next-leading-order (NLO) of an equilibrated weakly-coupled QGP is computed, since there are some concerns that a leading order (LO) calculation is not very reliable for the photon production rate due to rather large coupling constant at the modest temperature achieved in heavy ion collisions and uncertainty of the perturbative expansion. The contributions to the LO rate can be divided into distinct kinematical regimes – the hard, soft and collinear regions. The striking features is that the NLO correction is composed of two largely canceling contributions, the positive one from the collinear region and the negative one from the soft and semi-collinear region. The calculation shows the NLO correction at the order of $\simeq 20\%$, which does not alter qualitatively the current theoretical prediction on thermal photon emission.

Strong magnetic field produced in heavy ion collisions could be another possible source for direct photon. The enhancement of the thermal yield in the presence of the strong magnetic field perpendicular to the reaction plane is shown in [122, 123] via gauge and gravity duality, which can create a large anisotropy. It is also expected that quarks moving through the strong magnetic field will produce synchrotron radiation[124]. This has an effect on both

photon production (via thermal quarks emitting electromagnetic synchrotron radiation) and on jet quenching (via fast quark emitting gluonic synchrotron radiation).

Another significant source of low p_T direct photons can be the pre-equilibrium Glasma stage very early in the collision [125]. The Glasma begins in the earliest stages of heavy ion collisions as an ensemble of longitudinal color electric and color magnetic lines of flux, and then decays into a far-from-equilibrium gluon-dominated matter. Owing to the high occupancy of gluons that coherently amplifies scattering, the resulting Glasma appears strongly interacting during the time toward thermalization even though the coupling is weak.

It should be noted that many of these novel ideas and calculations are still in the early stages of development. More work is required to make realistic and accurate statement to close in the gap between theoretical prediction on thermal photon emission and experimentally measured one. And the results in this thesis provide important constrains for possible solutions in the future.

Bibliography

[1] S. S. Adler et al. *Phys. Rev. Lett.*, 94:232301, 2005.

[2] PHENIX Collaboration. *Phys. Rev. D*, 71:071102, 2005.

[3] PHENIX Collaboration. *Phys. Letter. B*, 561:82, 2003.

[4] P. Braun-Munzinger, K.Redlich, and J.Stachel. Particle production in heavy ion collisions. arXiv:nucl-th/0304013.

[5] F.Karsch. Lattice qcd at high temperature and density. *Letc. Notes Phys.*, 583:209–249, 2002.

[6] P.F. Kolb. Expansion rates at RHIC. *Heavy Ion Phys.*, 21:243–248, 2004.

[7] S. Turbide, R. Rapp, and C. Gale. *Phys. Rev. C*, 69:014903, 2004.

[8] T. C. Awes. *Nucl. Phys.*, A590:81c–91c, 1995.

[9] T. Peitzmann. *Nucl. Phys.*, A685:399–406, 2001.

[10] L. E. Gordon and W. Vogelsang. *Phys. Rev.*, D48:3136, 1993.

[11] A. Adare et al. *Phys. Rev. Lett.*, 104:132301, 2010.

[12] S. S. Adler et al. *Phys. Rev. Lett.*, 98:012002, 2007.

[13] A. Bazilevsky A. Desphpande Y. Goto Y. Fukao B. Fox T. Horaguchi K. Okada K. Tanida H. Torii C. Aidala, F. Bauer. PHENIX Internal Analysis Note 224, 2003.

[14] L. Aphecetche et al. Phenix calorimeter. *Nuclear Instruments and Methods in Physics Research Section A: Accelerators, Spectrometers, Detectors and Associated Equipment*, 499(2-3):521–536, March 2003.

[15] Torbjorn Sjostrand et al. High-energy-physics event generation with PYTHIA 6.1. *Comput. Phys. Commun.*, 135:238–259, 2001.

[16] Ralf Averbeck. PHENIX Internal Analysis Note 349, 2005.

[17] C. Shen et al. arXiv:nucl-th/1308.2440, 2013.

[18] H. van Hees, C. Gale, and R. Rapp. *Phys. Rev.*, C84:054906, 2011.

[19] O. Linnyk et al. *Phys. Rev.*, C89:034908, 2014.

[20] PHENIX Collaboration. PHENIX Conceptional Design Report, 1993.

[21] W. M. Yao et al. Review of Particle Physics. *Journal of Physics G*, 33:1+, 2006.

[22] K. Reygers. PHENIX Internal Analysis Note 169, 2003.

[23] K. Adcox et al. *Nucl. Phys.*, A757:184, 2005.

[24] C. Caso et al. *Eur. Phys. J.*, C3:1, 1998.

[25] J. C. Collins, D. E. Soper, and G. Sterman. *Nucl. Phys.*, B261:104, 1985.

[26] K.Johnson et al. A. Chodos, R. L. Jaffe. *Phys. Rev. D*, 9:3471, 1974.

[27] C.Y. Wong. *Introduction to High-Energy Heavy-Ion Collisions*. World Scientifick, Singapore, 1994.

[28] K. G. Wilson. *Phys. Rev.*, D10:2445, 1974.

[29] Karl Jansen. Lattice QCD: a critical status report. arXiv:hep-lat/0810.5634.

[30] P. Petreczky. Lattice QCD at finite temperature: present status. *Nucl. Phys.*, A830:11c–18c, 2009.

[31] A. Bazavov et al. *Phys. Rev.*, D80:014504, 2009.

[32] F. Karsch. *Lect. Notes Phys.*, 583:209, 2002.

[33] L. D. Landau. *Izv. Akad. Nauk SSSR Ser. Fiz.*, 17:51, 1953.

[34] J. D. Bjorken. *Lect. Notes Phys.*, 56:93, 1976.

[35] J. D. Bjorken. Highly relativistic nucleus-nucleus collisions: The central rapidity region. *Phys. Rev.*, D27:371–382, 1983.

[36] J. W. Harris and B. Muller. *Ann. Rev. Nucl. Part. Sci.*, 46:71, 1996.

[37] J. Adams et al. *Nucl. Phys.*, A757:102, 2005.

[38] K. Adcox et al. *Nucl. Phys.*, A757:184, 2005.

[39] I. Arsene et al. *Nucl. Phys.*, A757:1, 2005.

[40] B. B. Back et al. *Nucl. Phys.*, A757:28, 2005.

[41] S. Afanasiev et al. arXiv:nucl-ex/0706.3034.

[42] J. Adams et al. *Phys. Rev. Lett.*, 93:012301, 2004.

[43] S. S. Adler et al. *Phys. Rev. Lett.*, 93:152302, 2004.

[44] S. Pratt. arXiv:nucl-th/0907.1094.

[45] S. S. Adler et al. *Phys. Rev. Lett.*, 91:182301, 2003.

[46] J. Adams et al. *Phys. Rev. Lett.*, 92:052302, 2004.

[47] Koshuke Yagi, Tetsuo Hatsuda, and Yasuo Miake. *Quark-Gluon Plasma.* Cambridge University Press, Cambridge, 2008.

[48] Z. Xu, C. Greiner, and H. Stocker. *Phys. Rev. Lett.*, 101:162301, 2008.

[49] V. Greco, M. Colonna, M. Di Toro, and G. Ferini. *Prog. Part. Nucl. Phys.*, 62:562, 2009.

[50] R. S. Bhalerao et al. *Phys. Lett.*, B627.

[51] S. S. Adler et al. *Phys. Rev. Lett.*, 105:062301, 2010.

[52] K. Adcox et al. Centrality dependence of the high p_T charged hadron suppression in au + au collisions at $\sqrt{s_{NN}} = 130GeV$. *Phys. Lett.*, B561:82–92, 2003.

[53] M. Gyulassy and M. Plumer. *Phys. Lett.*, B243:432, 1990.

[54] R. Baier, Y.L. Dokshitzer, S. Peigne, et al. *Phys. Lett.*, B345:277, 1995.

[55] J. W. Cronin et al. *Phys. Rev.*, D11:3105, 1975.

[56] J. J. Aubert et al. *Phys. Lett.*, B123:275, 1983.

[57] G. Piller and W. Weise. *Phys. Rept.*, 330:1, 2000.

[58] X. N. Wang and M. Gyulassy. *Phys. Rev. Lett.*, 68:1480, 1992.

[59] T. Matsubara. A new approach to quantum-statistical mechanics. *Prog. Theor. Phys.*, 14:351–378, 1955.

[60] H. A. Weldon. Simple rules for discontinuities in finite-temperature field theory. *Phys. Rev.*, D28:2007–2015, 1983.

[61] L. McLerran and T. Toimela. Photon and dilepton emission from the quark-gluon plasma: Some general considerations. *Phys. Rev.*, D31:545–563, 1985.

[62] C. Gale and J. I. Kapusta. Vector dominance model at finite temperature. *Nucl. Phys.*, B357:65–89, 1991.

[63] J. I. Kapusta, P. Lichard, and D. Seibert. *Phys. Rev.*, D44:2774, 1991.

[64] R. J. Fries, B. Muller, and D. K. Srivastava. *Phys. Rev. Lett.*, 90:132301, 2003.

[65] R. Baur et al. *Z. Phys.*, C71:571, 1996.

[66] M. M. Aggarwal et al. *Phys. Rev. Lett.*, 85:3595, 2000.

[67] J. H. Cobb et al. *Phys. Lett.*, 78B:519, 1978.

[68] C. Albajar et al. *Phys. Lett.*, B209:397, 1988.

[69] A. Adare et al. arXiv:0911.0244[nucl-ex].

[70] P. Lichard. *Phys. Rev.*, D51:6017, 1995.

[71] D. G. d'Enterria and D. Peressounko. *Eur. Phys. J. C*, 46:451, 2006.

[72] R. Chatterjee and D. K. Srivastava. *Phys. Rev. C*, 79:021901, 2009.

[73] Richard Petti. Measurement of low transverse momentum direct photons via external conversions. PHENIX Internal Analysis Note 943.

[74] Benjamin Bannier, Axel Drees, and Richard Petti. PHENIX Internal Analysis Note 1041, 2013.

[75] R.Chatterjee, E.S. Frodermann, U.W. Heinz, and D.K. Srivastava. *Phys. Rev. Lett*, 96:202302, 2006.

[76] H.Holopainen, S. Rasanen, and K.J. Eskola. *Phys. Rev. C*, 84:1104.5371, 2011.

[77] A. Adare et al. *Phys. Rev. Lett.*, 109:122302, 2012.

[78] C. Montag and T. Satogata. BNL-96440-2011-IR C-A/AP/435, 2011.

[79] K. Adcox et al. Phenix detector overview. *Nuclear Instruments and Methods in Physics Research Section A: Accelerators, Spectrometers, Detectors and Associated Equipment*, 499(2-3):469–479, March 2003.

[80] M. Allen et al. Phenix inner detectors. *Nuclear Instruments and Methods in Physics Research Section A: Accelerators, Spectrometers, Detectors and Associated Equipment*, 499(2-3):549–559, March 2003.

[81] S. S. Adler et al. Elliptic flow of identified hadrons in $au + au$ collisions at $\sqrt{s_{NN}} = 200\ GeV$. *Phys. Rev. Lett.*, 91(18):182301, Oct 2003.

[82] Mickey Chiu, Alexei Denisov, Edmundo Garcia, Judith Katzy, Andrei Makeev, Michael Murray, and Sebastian White. Measurement of mutual coulomb dissociation in $\sqrt{s_{NN}} = 130$ GeV Au+Au collisions. *Phys. Rev. Lett.*, 89(1):012302, Jun 2002.

[83] S. H. Aronson et al. *Nucl. Instrum. Meth.*, A499:499, 2003.

[84] A. Kozlov et al. *Nucl. Instrum. Meth.*, A523:345, 2004.

[85] Z. Fraenkel et al. *Nucl. Instrum. Meth.*, A546:466, 2005.

[86] K. Adcox et al. *Nucl. Instrum. Meth.*, A499:489, 2003.

[87] M. Aizawa et al. *Nucl. Instrum. Meth.*, A499:508, 2003.

[88] S. S. Adler et al. *Nucl. Instrum. Meth.*, A499:560, 2003.

[89] WA98 Collaboration. CERN Report No. SPSLC 91-17, 1991.

[90] T.C. Awes et al. arXiv:nucl-ex/0202009, 2002.

[91] *Geant: Simulation program for particle physics experiments. user guide and reference manual.*, 2013.

[92] J. T. Mitchell et al. *Nucl. Instr. Meth.*, A482:491–512, 2002.

[93] G.David, T. Sakaguchi, and R. Vertesi. Simulation verification in the emcal pbsc shower cahracteristics of hadrons. PHENIX Internal Analysis Note 330.

[94] S. Kelly, D. Morrison, and J. Nagle. PHENIX Internal Analysis Note 33, 2000.

[95] K. Adcox et al. Phenix central arm tracking detectors. *Nuclear Instruments and Methods in Physics Research Section A: Accelerators, Spectrometers, Detectors and Associated Equipment*, 499(2-3):489–507, March 2003.

[96] Gabor David. Study of emcal standalone particle identification in hijing events, 1997.

[97] Garbor David and Takao Sakaguchi. π^0 and photon analysis with stochastic cuts in 200GeV Au+Au collisions (run-2). PHENIX Internal Analysis Note 352.

[98] S. S. Adler et al. *Phys. Rev. C*, 69:034909, 2004.

[99] S. S. Adler et al. High transverse momentum η meson production in p+p, d+au and au+au collisions at $sqrtS_{NN} = 200GeV$. *Phys. Rev. C*, 75:024909, 2007.

[100] R. Albrecht et al. Production of η mesons in 200-a/GeV s+s and s+Au reactions. *Phys. Lett.*, B361:14–20, 1995.

[101] N. M. Kroll and W. Wada. *Phys. Rev.*, 98:1355, 1955.

[102] L. G. Landsberg. Electromagnetic decays of light mesons. *Phys. Rep.*, 128:301, 1985.

[103] J. C. Collins and D. E. Soper. *Phys. Rev.*, D17:2219, 1977.

[104] Benjamin Bannier, Axel Drees, and Richard Petti. PHENIX Internal Analysis Note 1139, 2013.

[105] A. Adare et al. *Phys. Rev.*, D109:072008, 2012.

[106] Y. Aoki, Z. Fodor, S. D. Katz, and K. K. Szabo. *Phys. Lett.*, B643:46, 2006.

[107] A. Bazavov et al. *Phys. Rev.*, D85:054503, 2012.

[108] M. Wilde et al. *Nucl. Phys.*, A904–905:573c, 2013.

[109] T. Hirano and K. Tsuda. *Phys. Rev.*, C66:054905, 2002.

[110] P. Huovinen. arXiv:nucl-ex/0305064, 2003.

[111] P. F. Kolb and U. W. Heinz. arXiv:nucl-ex/0305084, 2003.

[112] Benjamin Bannier, Axel Drees, and Richard Petti. PHENIX Internal Analysis Note 1138, 2013.

[113] G. Y. Qin, J. Ruppert, C. Gale, S. Jeon, and G. D. Moore. *Phys. Rev.*, C80:054909, 2009.

[114] S. Turbide, C. Gale, E. Frodermann, and U. Heinz. *Phys. Rev.*, C77:024909, 2008.

[115] R. Chatterjee, H. Holopainen, I. Helenius, T. Renk, and K. J. Eskola. arXiv:hep-ph/1305.6443, 2013.

[116] V. Konchakovski et al. *Phys. Rev.*, C85:044922, 2012.

[117] O. Linnyk et al. *Phys. Rev.*, C84:054917, 2011.

[118] V. Konchakovski et al. *Phys. Rev.*, C85:011902, 2012.

[119] E. Bratkovskaya et al. *Nucl. Phys.*, A856:162, 2011.

[120] J. Cleymans, V. Goloviznin, and K. Redlich. *Phys. Rev.*, D47:173, 1993.

[121] Jacopo Ghiglieri et al. arXiv:hep-ph/1302.5970, 2013.

[122] G. Basar, D.E. Kharzeev, and V. Skokov. *Phys. Rev. Lett.*, 109:202303, 2012.

[123] B. Müller, S.Y. Wu, and D.L. Yang. *arXiv:1308.6568*, 2013.

[124] V. V. Goloviznin et al. arXiv:hep-ph/1209.2380, 2013.

[125] Mickey Chiu et al. *Nucl. Phys.*, A900:16–37, 2013.

Appendix A

List of Analyzed Runs

108368	108768	108772	108778	108785	108908	108928	108943	109187	109189
109191	109192	109196	109197	109204	109214	109217	109220	109222	109238
109240	109242	109246	109252	109291	109293	109297	109355	109361	109363
109364	109366	109422	109424	109426	109470	109475	109477	109479	109482
109549	109550	109569	109573	109576	109587	109593	109654	109655	109656
109657	109659	109660	109664	109672	109673	109675	109677	109679	109684
109690	109691	109693	109699	109719	109762	109763	109764	109765	109767
109769	109820	109821	109822	111396	111402	111406	111413	111421	111423
111425	111436	111467	111468	111485	111494	111495	111497	111498	111500
111502	111528	111530	111531	111532	111538	111539	111544	111555	111556
111558	111559	111560	111583	111592	111593	111603	111604	111687	111688
111695	111697	111699	111701	111705	111711	111714	111716	111743	111824
111830	111831	111838	111893	111894	111895	111951	111953	111955	111957
111959	111964	111966	111982	111984	111985	112057	112059	112061	112064
112066	112071	112075	112122	112124	112128	112184	112186	112232	112233
112234	112283	112284	112286	112287	112288	112318	112320	112323	112403
112411	112475	112476	112477	112479	112480	112482	112483	112484	112492
112493	112504	112506	112507	112509	112511	112519	112526	112527	112657
112660	112661	112664	112666	113106	113107	113108	113194	113198	113201
113202	113204	113232	113284	113286	113288	113290	113464	113466	113468
113528	113529	113530	113559	113562	113564	113570	113573	113574	113575
113580	113688	113689	113690	113691	113695	113696	113703	113704	113706
113716	113838	113839	113840	113842	113851	113852	113854	113871	113873
113875	113877	113879	113880	113902	113904	113975	113979	113982	113983
113986	113999	114001	114003	114066	114069	114074	114075	114076	114086
114088	114089	114102	114143	114144	114145	114147	114271	114278	114280
114287	114295	114296	114329	114330	114332	114334	114399	114401	114405
114406	114414	114432	114467	114468	114471	114594	114602	114614	114616
114618	114621	114659	114660	114666	114681	114689	114802	114805	114808
114836	114837	114884	114887	114901	114927	114929	114936	114965	114967
114970	114971	114972	114993	114994	114997	115031	115050	115069	115070
115077	115087	115179	115180	115182	115185	115191	115205	115227	115237
115345	115347	115350	115358	115361	115366	115501	115502	115503	115778
115780	116061	116085	116087	116135	116136	116137	116138	116142	116146
116160	116161	116163	116167	116169	116178	116184	116186	116192	116228

Table A.1: List of runs used in the analysis of Au + Au data (part1).

116229	116236	116237	116313	116315	116317	116321	116338	116341	116353
116359	116419	116421	116423	116425	116427	116468	116472	116533	116534
116539	116544	116546	116547	116551	116566	116571	116572	116574	116609
116617	116620	116636	116637	116639	116642	116646	116657	116659	116660
116662	116690	116701	116702	116706	116707	116708	116742	116743	116746
116747	116749	116776	116777	116831	116833	116838	116842	116913	116917
116921	116927	116929	116933	117119	117120	117122	117128	117173	117223
117225	117226	117253	117255	117256	117258	117280	117290	117291	117295
117297	117303	117311	117327	117328	117427	117428	117429	117430	117431
117433	117435	117441	117443	117447	117455	117457	117543	117544	117546
117547	117574	117575	117576	117579	117581	117583	117586	117590	117592
117602	117604	117606	117607	117609	117613	117684	117685	117686	117694
117716	117725	117759	117760	117764	117766	117768	117770	117772	117776
117779	117781	117821	117823	117825	117826	117827	117847	117848	117849
117851	117852	117921	117922	117925	117927	118015	118019	118024	118028
118038	118042	118211	118252	118254	118301	118304	118308	118312	118314
118321	118435	118438	118440	118446	118457	118458	118462	118464	118468
118469	118674	118676	118751	118754	118764	118767	118770	118777	118779
118870	118901	118903	118911	118912	118923	118929	118932	118933	118934
119100	119106	119108	119125	119129	119133	119134	119138	119139	119140
119141	119143	119264	119267	119268	119269	119314	119326	119327	119329
119380	119381	119386	119387	119417	119420	119421	119428	119433	119440
119448	119451	119452	119549	119550	119618	119621	119684	119687	119688
119690	119691	119763	119768	119917	119919	119921	119925	119926	119928
119969	120039	120045	120047	120048	120057	120058	120059	120060	120061
120062	120063	120064	120078	120079	120081	120082	120194	120199	120200
120214	120219	120234	120237	120238	120240	120246	120261	120269	120274
120278	120279	120285	120286	120394	120396	120397	120402	120404	120405
120406	120407	120408	120410	120411	120416	120419	120420	120422	120426
120427	120428	120478	120479	120480	120483	120489	120491	120495	120496
120497	120498	120499	121220	121224	121233	121237	121266	121271	121275
121287	121288	121289	121291	121292	121293	121294	121295	121296	121343
121344	121347	121401	121404	121406	121408	121449	121458	121463	121465
121510	121511	121513	121523	121526	121531	121533	121534	121543	121544
121545	121548	121554	121807	121809	122041	122213	122214	122215	122220
122223									

Table A.2: List of runs used in the analysis of Au + Au data (part2).

Appendix B

Dead Areas in PbSc and PC3

B.1 List of Dead Towers in PbSc

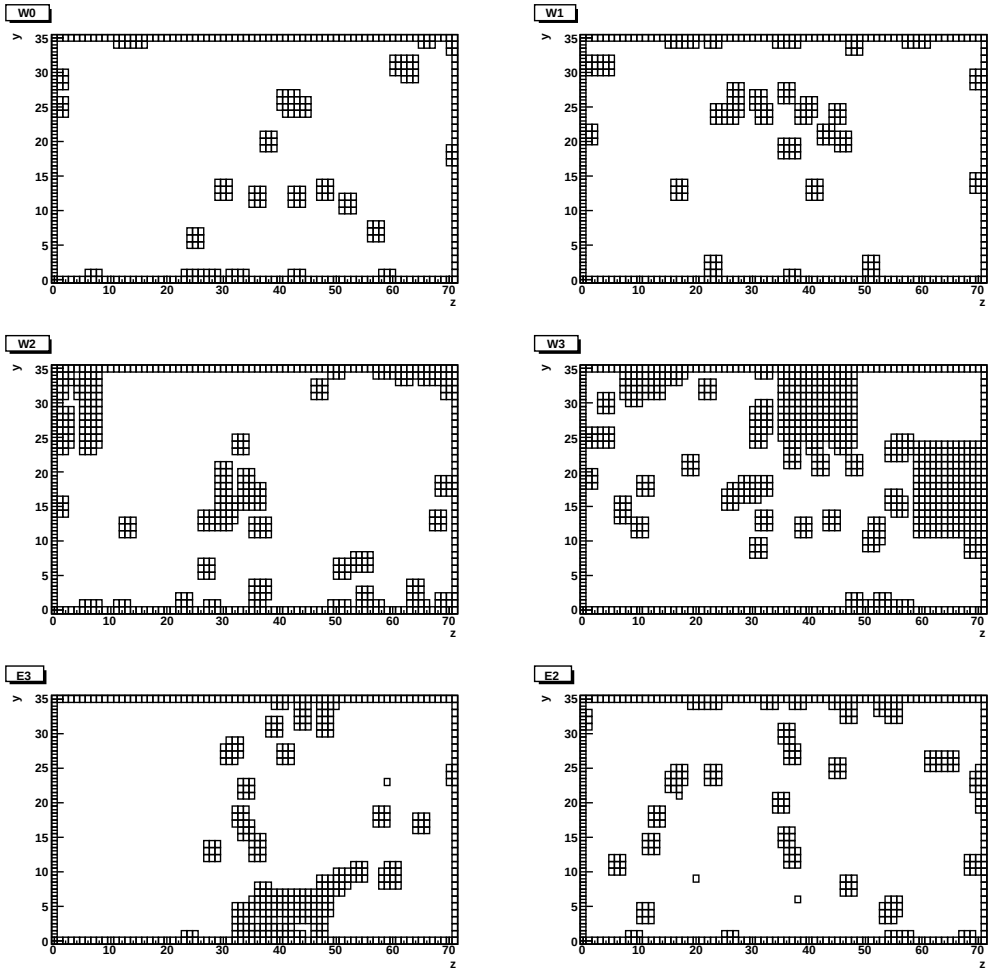

Figure B.1: Dead towers marked as boxes in the analysis for the Au+Au data. The edge towers of each sectors are also shown and excluded to reflect the fiducial cut in data analysis.

B.2 List of Dead Areas in PC3

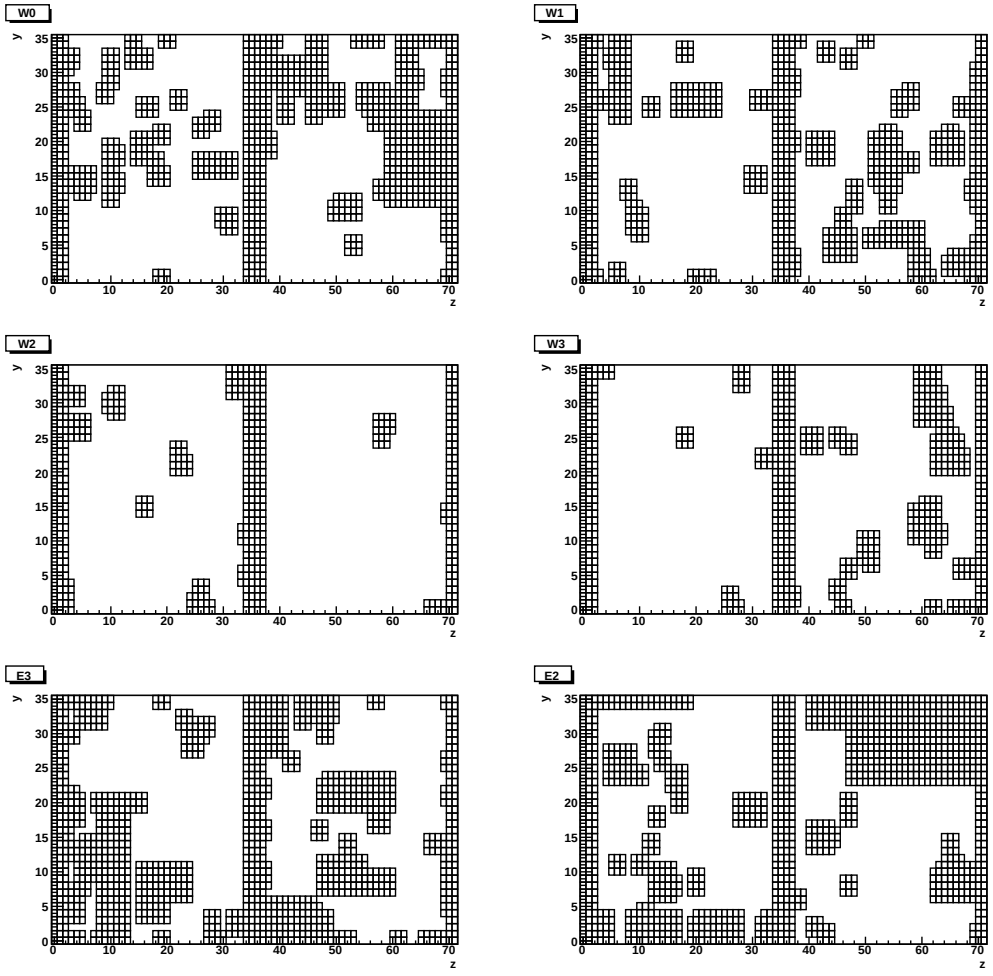

Figure B.2: PC3 dead areas projected into PbSc towers in the analysis for the Au+Au data.

Appendix C

Tagged γ^{π^0} Yield Extraction for Stochastic Cut2 Dataset

C.1 Yield Extraction for $0.0-0.5 GeV/c$ and $0.5-1.0 GeV/c$

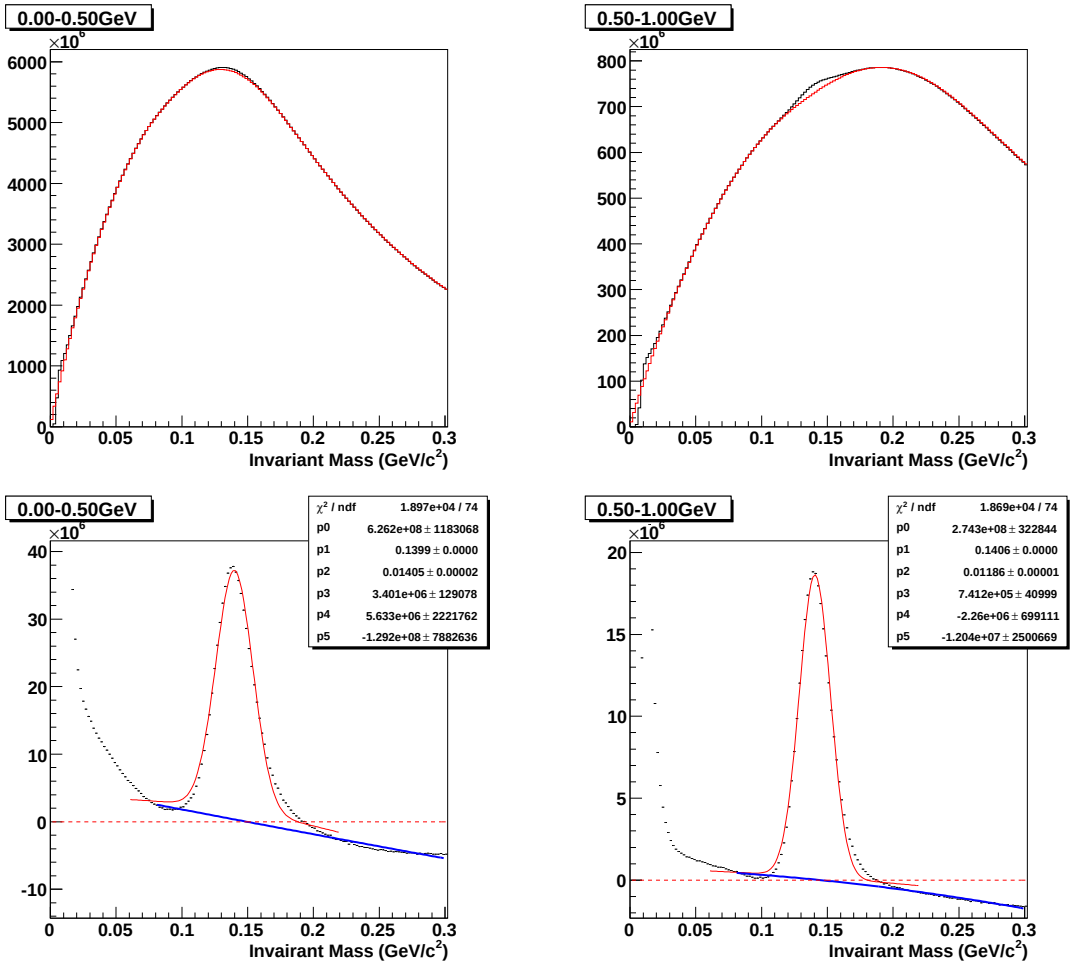

Figure C.1: Peak extraction for Stochastic Cut2 Dataset in $0.0 - 0.5 GeV/c$ and $0.5 - 1.0 GeV/c$ p_T bin

C.2 Yield Extraction for $1.0-1.5GeV/c$ and $1.5-2.0GeV/c$

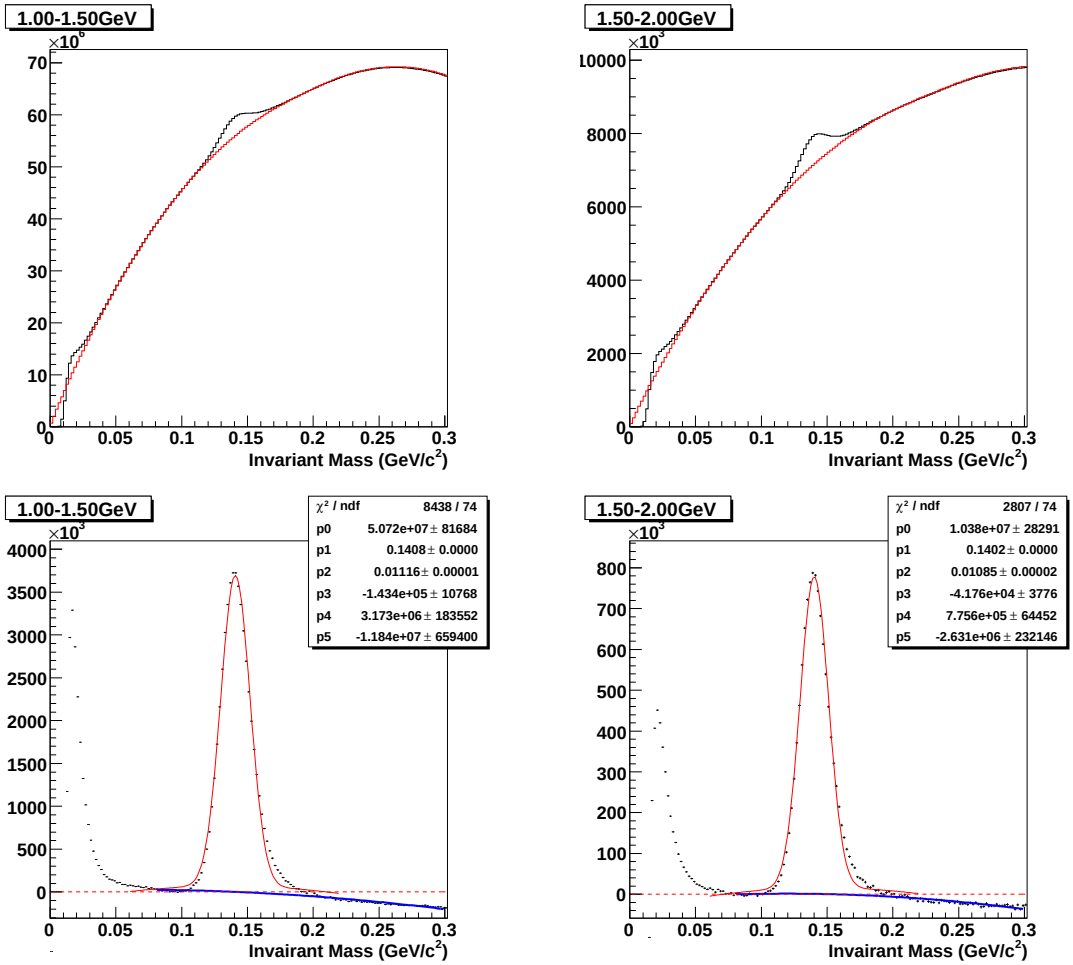

Figure C.2: Peak extraction for Stochastic Cut2 Dataset in $1.0-1.5GeV/c$ and $1.5-2.0GeV/c$ p_T bin

C.3 Yield Extraction for $2.0-2.5 GeV/c$ and $2.5-3.0 GeV/c$

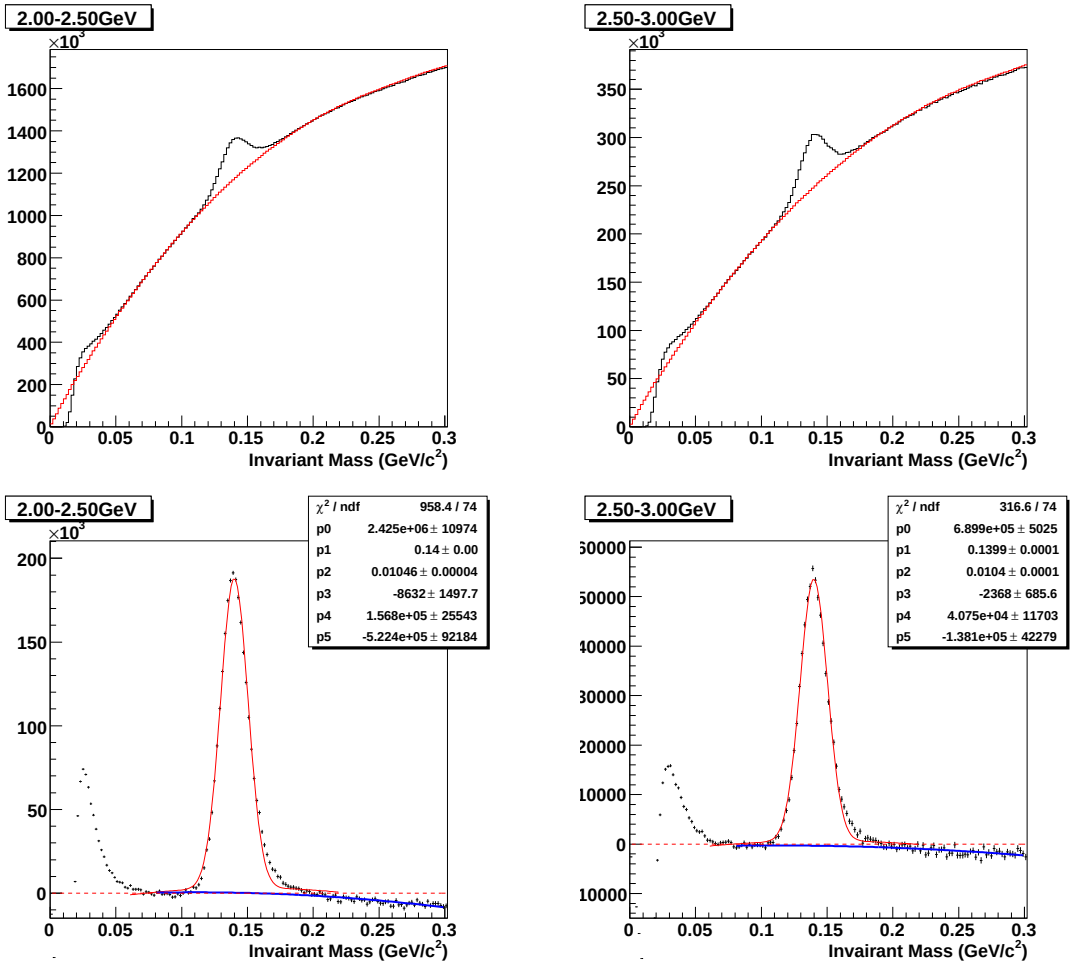

Figure C.3: Peak extraction for Stochastic Cut2 Dataset in $2.0-2.5 GeV/c$ and $2.5-3.0 GeV/c$ p_T bin

C.4 Yield Extraction for $3.0-3.5 GeV/c$ and $3.5-4.0 GeV/c$

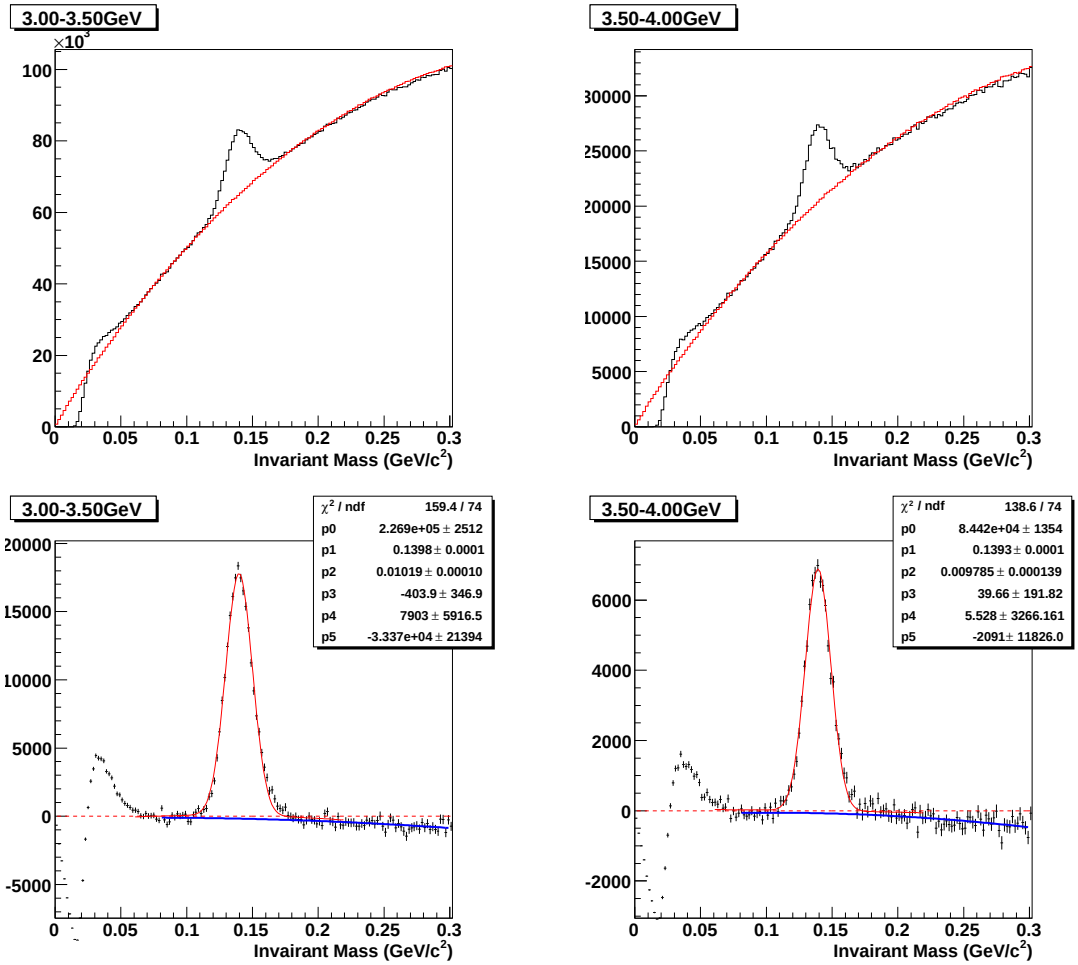

Figure C.4: Peak extraction for Stochastic Cut2 Dataset in $3.0-3.5 GeV/c$ and $3.5-4.0 GeV/c$ p_T bin

C.5 Yield Extraction for $4.0-4.5 GeV/c$ and $4.5-5.0 GeV/c$

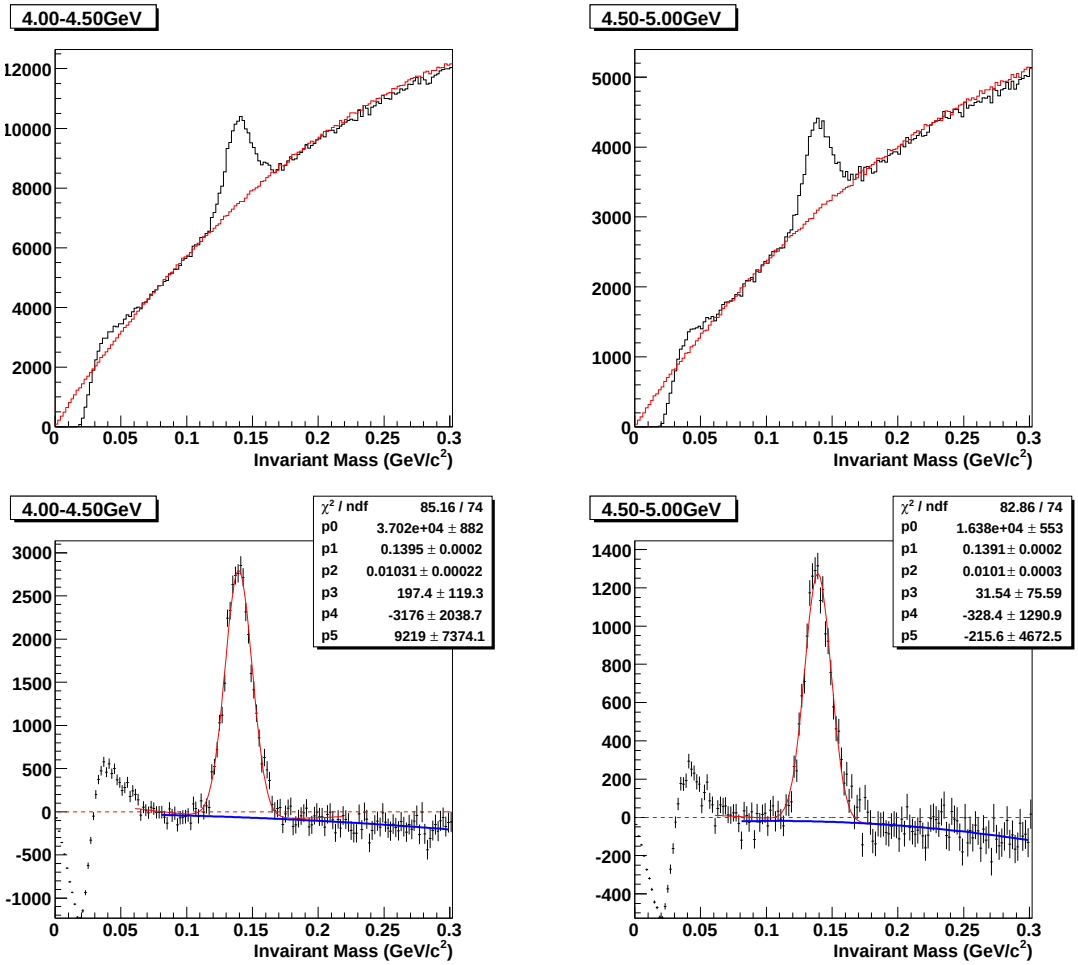

Figure C.5: Peak extraction for Stochastic Cut2 Dataset in $4.0-4.5 GeV/c$ and $4.5-5.0 GeV/c$ p_T bin

C.6 Yield Extraction for $5.0-5.5 GeV/c$ and $5.5-6.0 GeV/c$

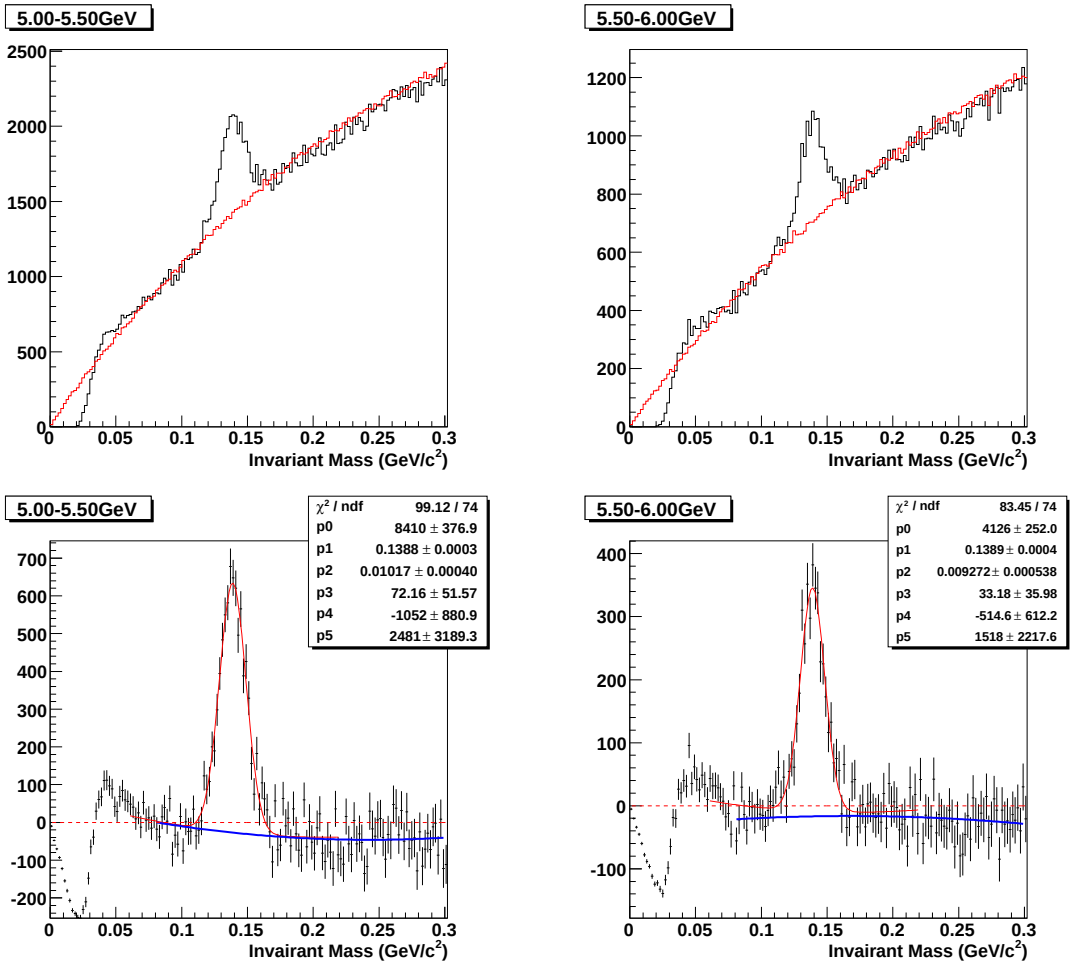

Figure C.6: Peak extraction for Stochastic Cut2 Dataset in $5.0 - 5.5 GeV/c$ and $5.5 - 6.0 GeV/c$ p_T bin

C.7 Yield Extraction for $6.0-6.5 GeV/c$ and $6.5-7.0 GeV/c$

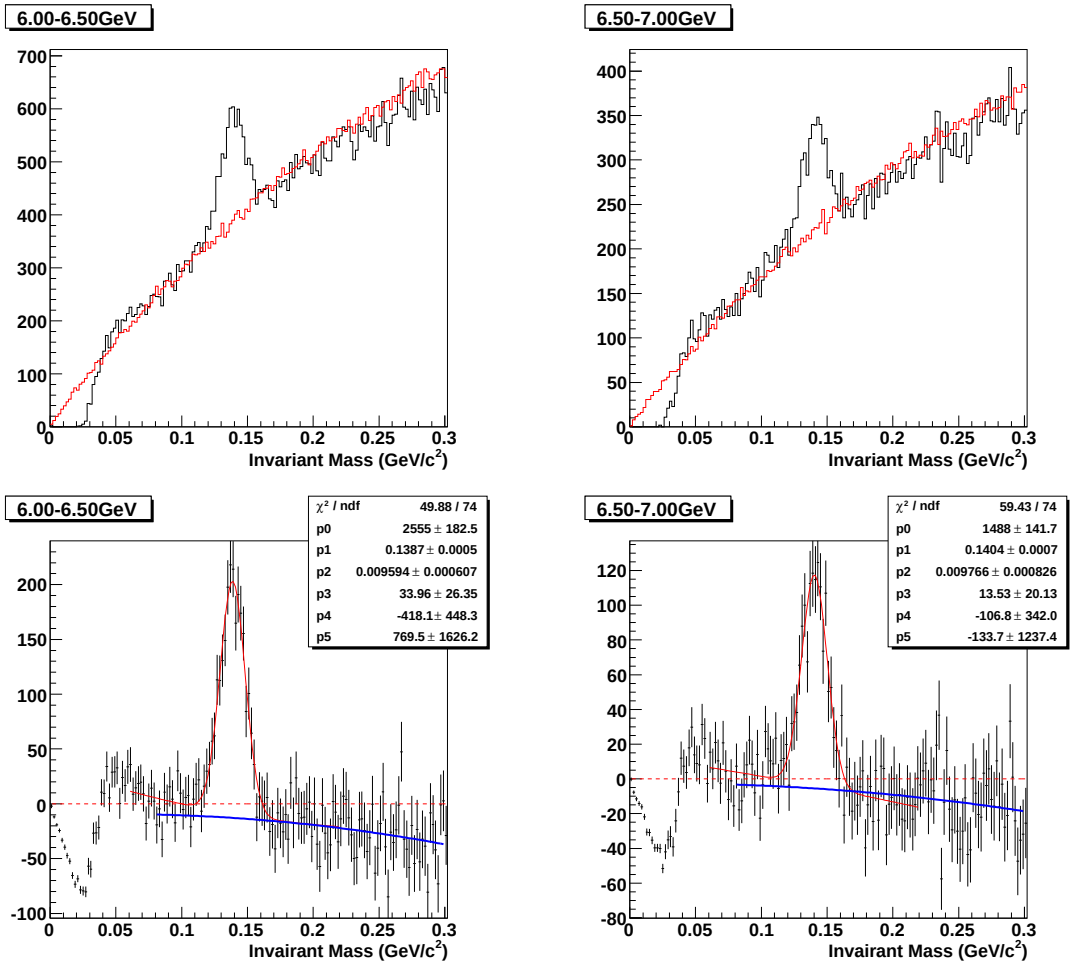

Figure C.7: Peak extraction for Stochastic Cut2 Dataset in $6.0-6.5 GeV/c$ and $6.5-7.0 GeV/c$ p_T bin

C.8 Yield Extraction for $7.0-7.5 GeV/c$ and $7.5-8.0 GeV/c$

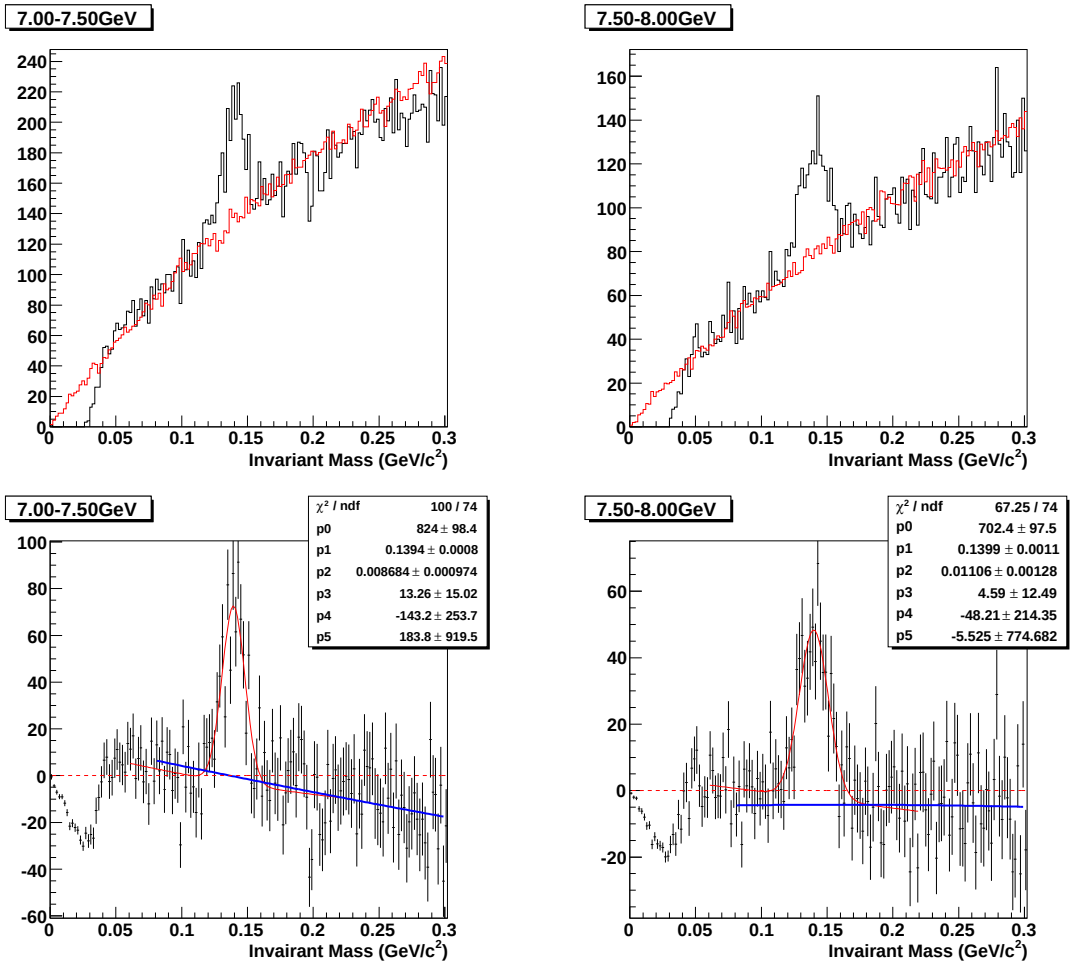

Figure C.8: Peak extraction for Stochastic Cut2 Dataset in $7.0 - 7.5 GeV/c$ and $7.5 - 8.0 GeV/c$ p_T bin

Appendix D

Tagged γ^{π^0} Yield Extraction for PC3Veto Cut Dataset

D.1 Yield Extraction for $0.0-0.5 GeV/c$ and $0.5-1.0 GeV/c$

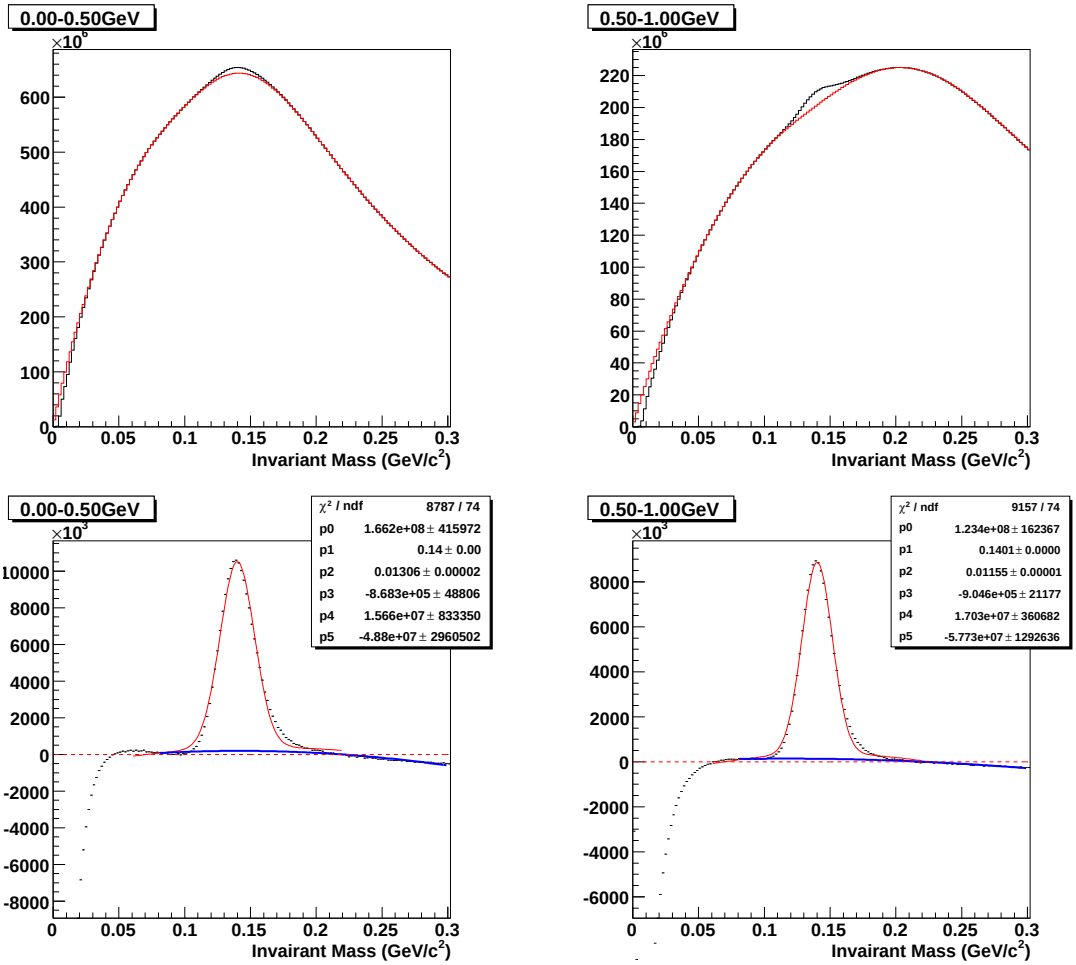

Figure D.1: Peak extraction for PC3Veto Cut Dataset in $0.0 - 0.5 GeV/c$ and $0.5 - 1.0 GeV/c$ p_T bin

D.2 Yield Extraction for $1.0-1.5 GeV/c$ and $1.5-2.0 GeV/c$

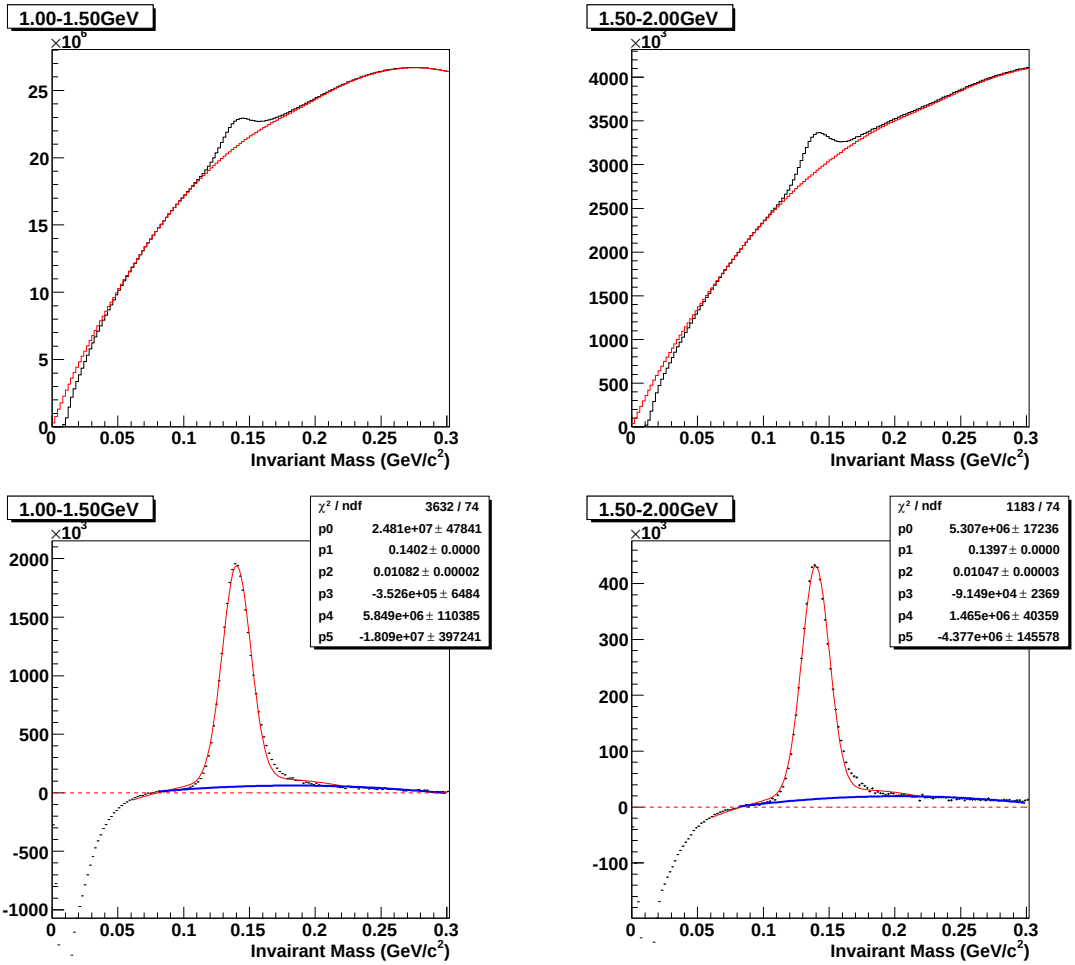

Figure D.2: Peak extraction for PC3Veto Cut Dataset in $1.0 - 1.5 GeV/c$ and $1.5 - 2.0 GeV/c$ p_T bin

D.3 Yield Extraction for $2.0-2.5 GeV/c$ and $2.5-3.0 GeV/c$

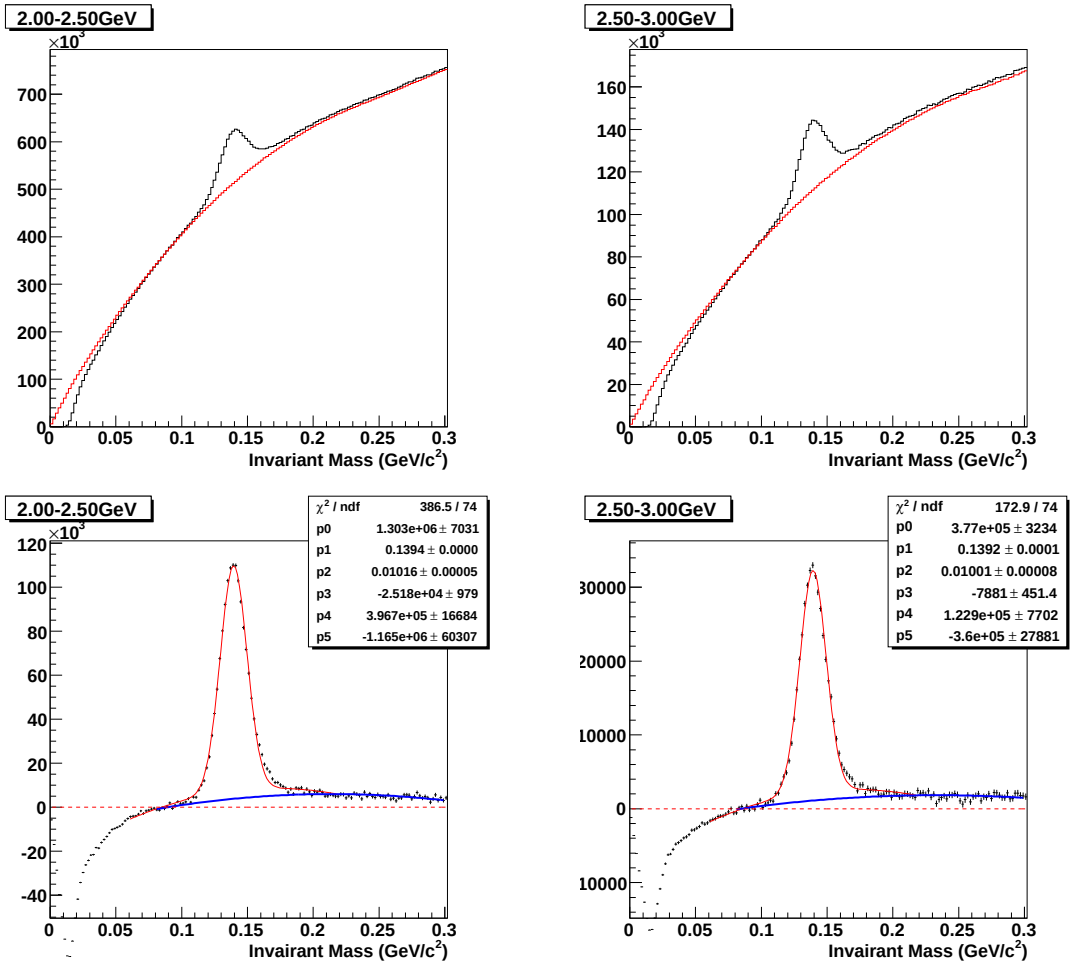

Figure D.3: Peak extraction for PC3Veto Cut Dataset in $2.0-2.5 GeV/c$ and $2.5-3.0 GeV/c$ p_T bin

D.4 Yield Extraction for $3.0-3.5 GeV/c$ and $3.5-4.0 GeV/c$

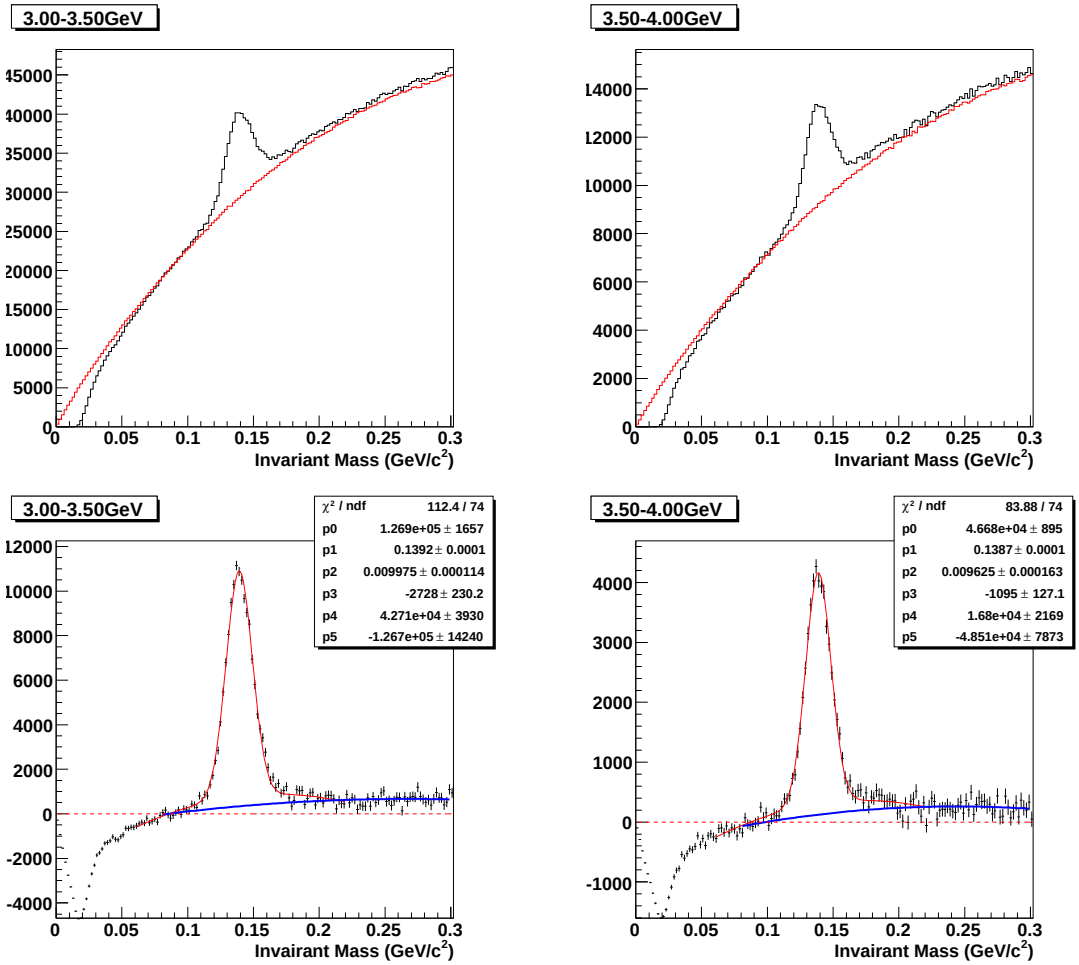

Figure D.4: Peak extraction for PC3Veto Cut Dataset in $3.0-3.5 GeV/c$ and $3.5-4.0 GeV/c$ p_T bin

D.5 Yield Extraction for $4.0-4.5 GeV/c$ and $4.5-5.0 GeV/c$

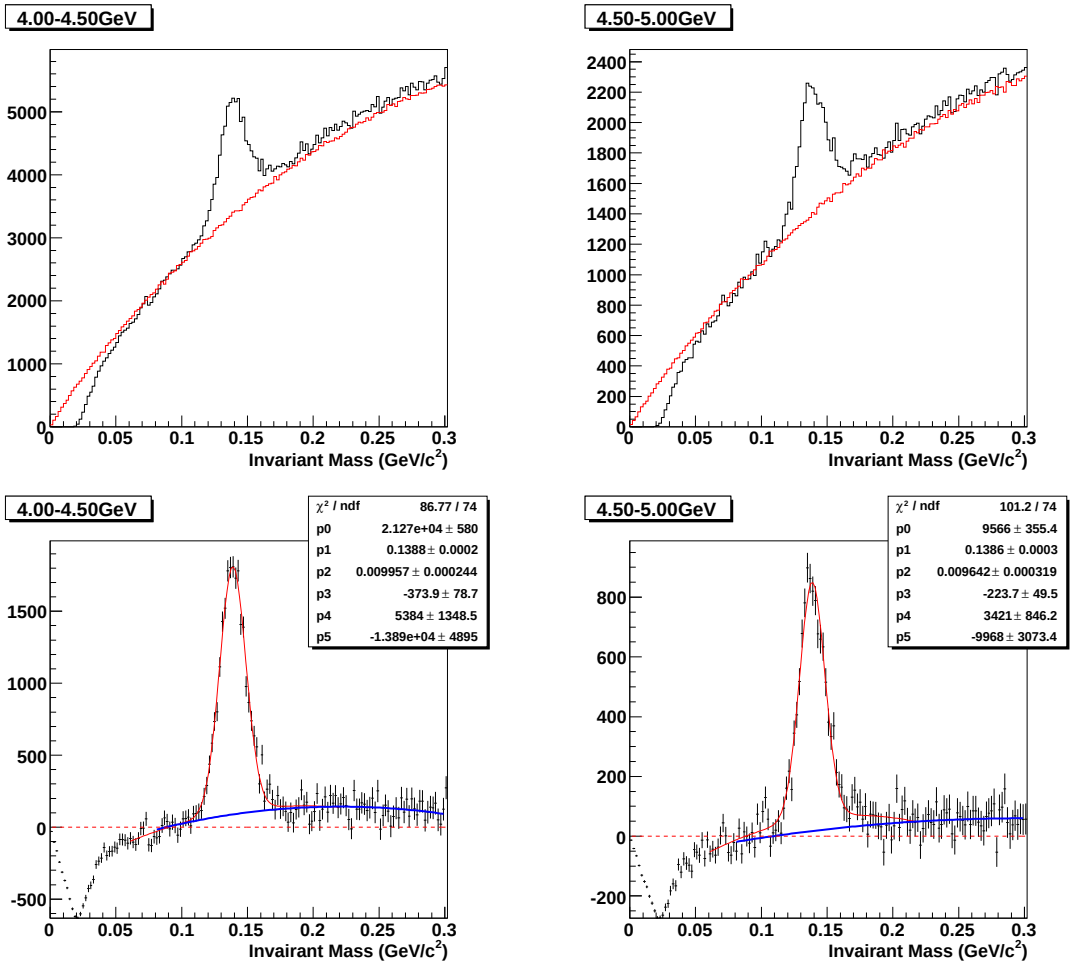

Figure D.5: Peak extraction for PC3Veto Cut Dataset in $4.0-4.5 GeV/c$ and $4.5-5.0 GeV/c$ p_T bin

D.6 Yield Extraction for $5.0-5.5 GeV/c$ and $5.5-6.0 GeV/c$

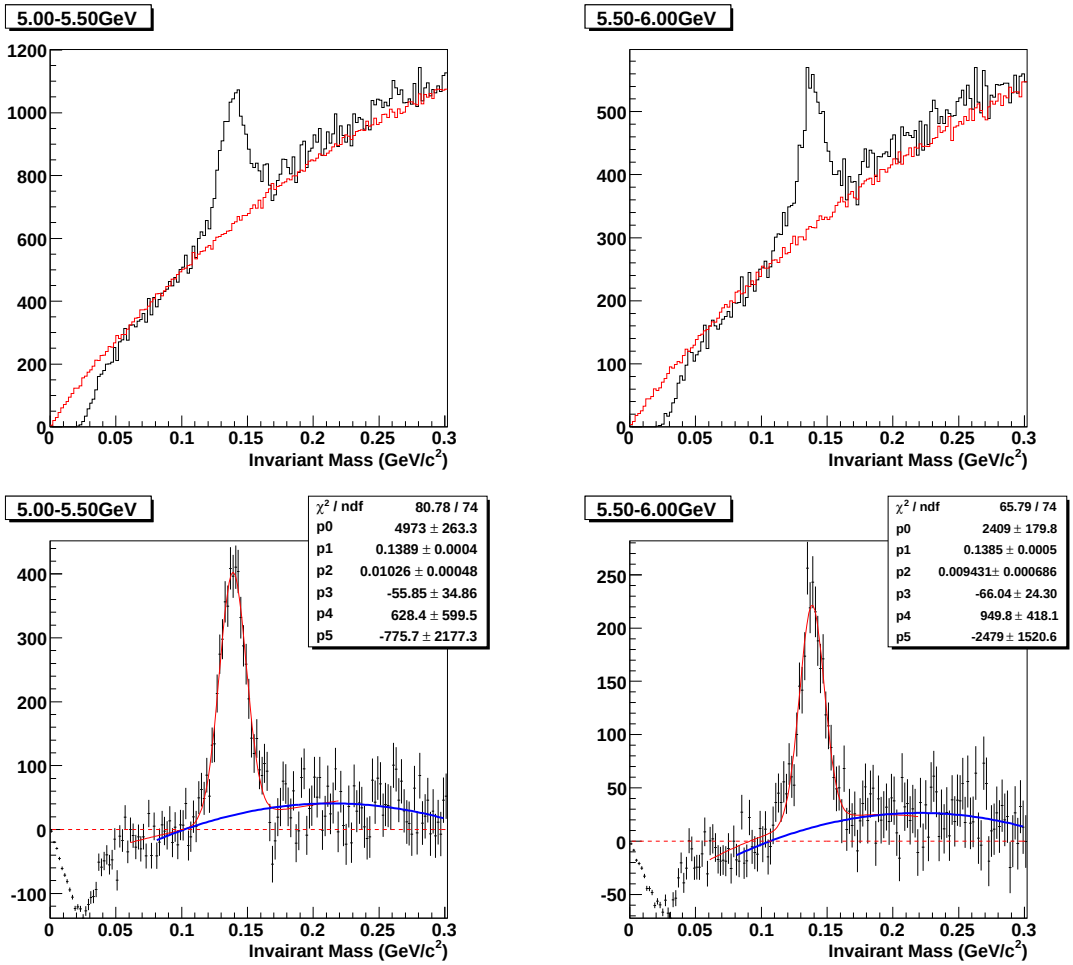

Figure D.6: Peak extraction for PC3Veto Cut Dataset in $5.0-5.5 GeV/c$ and $5.5-6.0 GeV/c$ p_T bin

D.7 Yield Extraction for $6.0-6.5 GeV/c$ and $6.5-7.0 GeV/c$

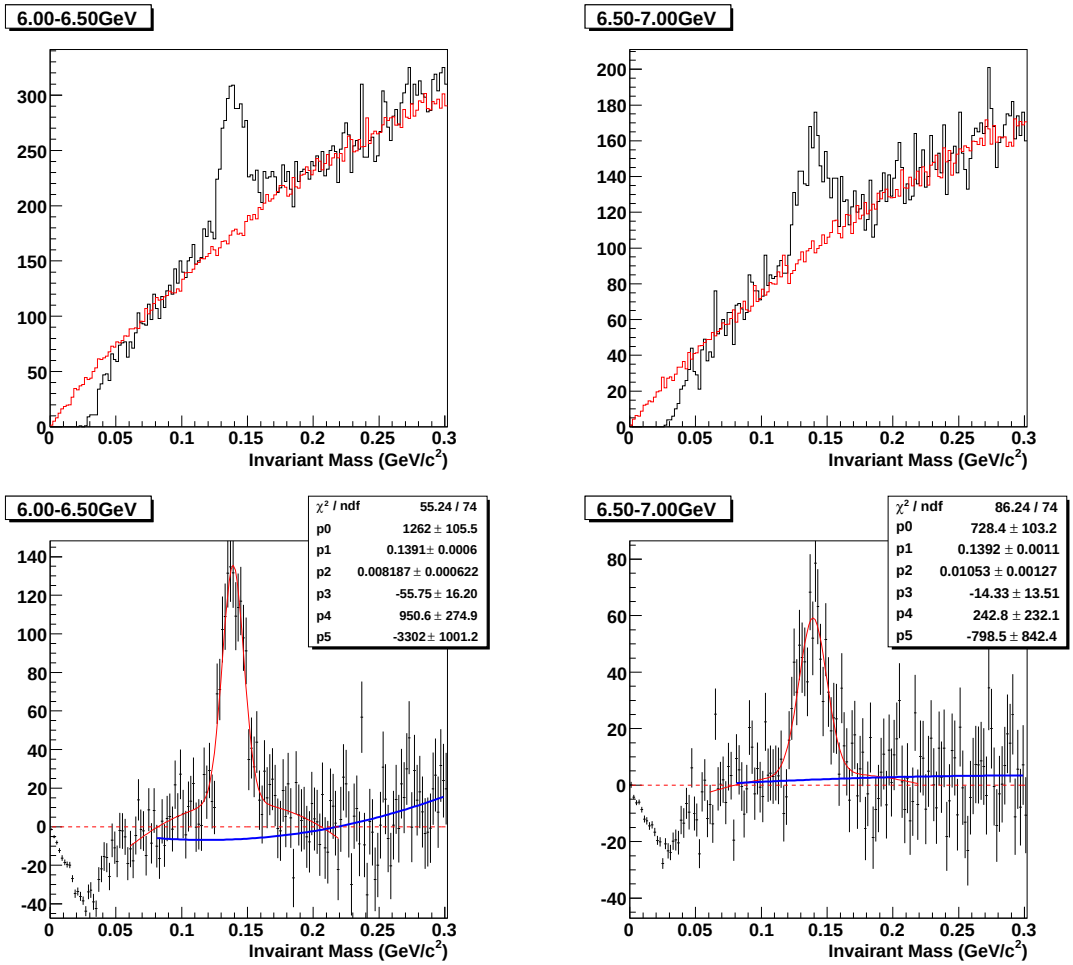

Figure D.7: Peak extraction for PC3Veto Cut Dataset in $6.0-6.5 GeV/c$ and $6.5-7.0 GeV/c$ p_T bin

D.8 Yield Extraction for $7.0-7.5 GeV/c$ and $7.5-8.0 GeV/c$

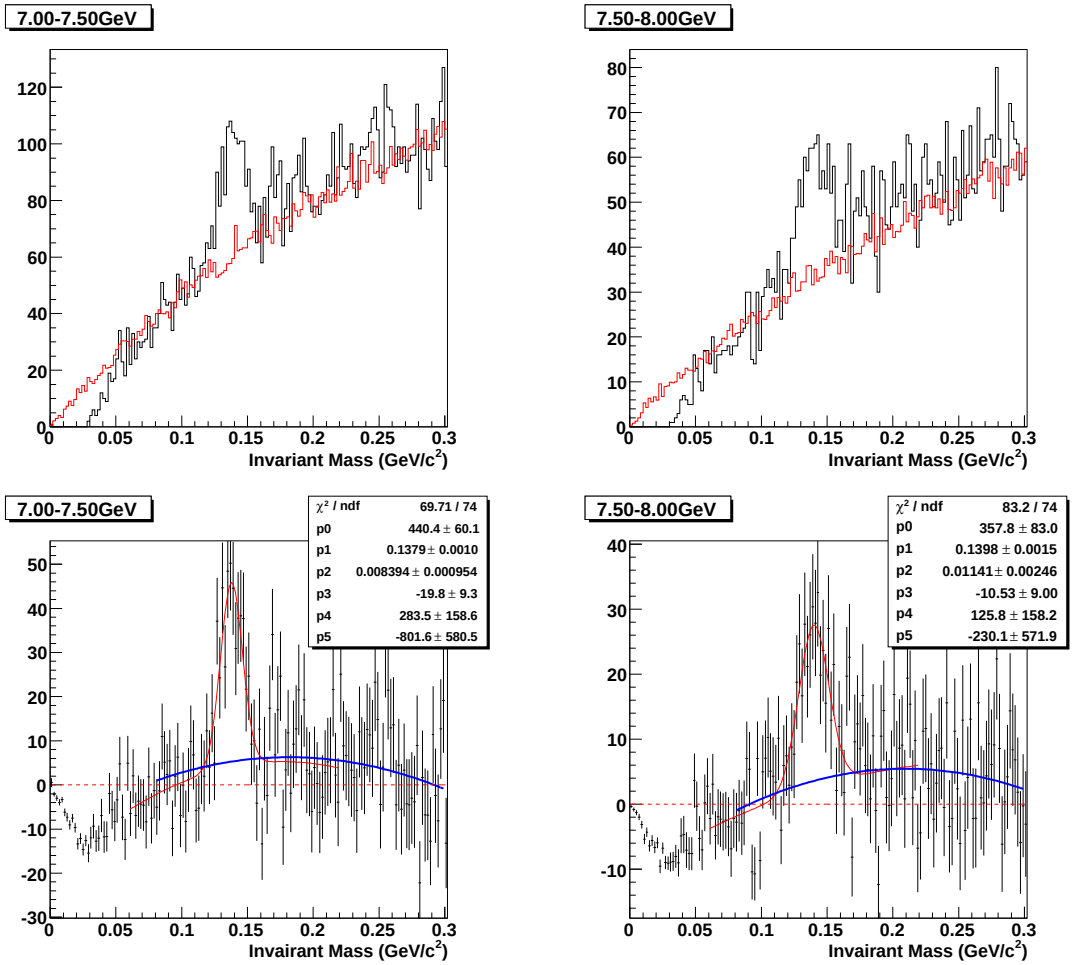

Figure D.8: Peak extraction for PC3Veto Cut Dataset in $7.0-7.5 GeV/c$ and $7.5-8.0 GeV/c$ p_T bin